# Indonesian Throughflow Heat Transport, and Spreading within the Eastern Tropical Indian Ocean

Laura Kristen Gruenburg

Submitted in partial fulfillment of the
requirements for the degree of
Doctor of Philosophy
under the Executive Committee
of the Graduate School of Arts and Sciences

COLUMBIA UNIVERSITY

2021

# Abstract

Indonesian Throughflow Heat Transport, and Spreading within the

Eastern Tropical Indian Ocean

Laura Kristen Gruenburg

The Indonesian Throughflow (ITF) is the only low latitude connector between the Pacific and Indian Oceans affecting upper ocean stratification and regional climate. Here we focus on the Indian Ocean side of this connection, first identifying changes within the primary throughflow pathway within the Indonesian Seas, then following the throughflow as it moves within the eastern tropical Indian Ocean.

Moored velocity measurements and an ENSO varying temperature profile developed from all available observations within the Makassar Strait are used to determine the southward heat flux anomaly (HFa) within this primary pathway of the ITF. Variability in the velocity profile is more important than that of the temperature profile for determining changes in the total heat flux with the former accounting for 72% of the variance in HFa and the latter 28%. As the upper layer (0-300 m) is the site of the largest volume transports and also the largest transport variability, upper layer HFa is far more dominant than the lower (320-740 m) in influencing the total depth integrated HFa. Upper ocean heat content anomaly (0-300 m; HCa) in the eastern tropical Indian Ocean calculated from gridded Argo datasets is well correlated with Makassar HFa at interannual timescales ($r = 0.8$). The lag between the two is 2.5 years, indicating that this is consistent with an advective signal.

From the Indo-Australian basin ITF waters flow either into the South Equatorial Current (SEC) to the west or the Leeuwin Current (LC) to the south. Gridded Argo data is used to track upper ocean heat content changes from the immediate outflow area into these two currents. The heat content anomaly timeseries in the region closest to the Indonesian Seas is well correlated with that at the easternmost section of the SEC with $r = 0.8$ at a 5 month lag. A notable exception occurs during 2011 when a positive heat content anomaly in the ITF outflow region is not later reflected in the SEC region, but rather expressed as an HCa increase the LC region. When compared to a previous HCa increase in the ITF outflow region during 2009, GODAS reanalysis shows that the velocity within the SEC was stronger eastward and the LC stronger southward during 2011. The Ningaloo Niño of 2011 was characterized by a low pressure anomaly off the west Australian Coast, which induced anomalous cyclonic circulation seen in NCEP/NCAR reanalysis winds at 1000 HPa. The positive zonal wind anomalies over the SEC and the reduction of southerly winds over the LC influenced these changes in current velocity. During the Ningaloo Niño of 2000 a similar pattern in atmospheric and oceanic circulation was identified. These results confirm the importance of the Ningaloo Niño in influencing the pathways of the ITF out of the Indo-Australian basin. Additionally, over the Argo time period, volume transport via the LC and SEC pathways appears anti-correlated, with increases in SEC outflow coupled with decreases in LC outflow.

As the SEC is the major pathway for the ITF within the Indian Ocean, we examine the propagation of these low salinity waters within the SEC thermocline. Using gridded Argo data, we examine the salinity along the $24\sigma$ surface as a proxy for ITF propagation, and the depth of the 20°C isotherm (d20) to determine how changes in the thermocline depth may affect the flow. The d20 was correlated with the salinity ($r=-0.5$) in the region of the Seychelles Chagos

Thermocline Ridge (SCTR), indicating that this region of upwelling, and the geostrophic currents that form around it, play a role in the westward propagation of the ITF. When examining the seasonal cycle, the effect of the SCTR is apparent as low salinity contours within the western portion of the basin show the furthest westward propagation during austral winter, when the SCTR is strong and most longitudinally expansive. On interannual timescales two years, 2010/11 and 2016/17, show anomalously high salinity in the SEC thermocline indicative of a reduction of ITF westward propagation. During late 2010 and 2016 anomalously strong upwelling regions are present at about 80°E and 10°S, out of the normal season for strong upwelling at this location. GODAS reanalysis velocity at 105 m shows cyclonic circulation developed around these upwelling centers, disrupting the normal zonal pathway of the SEC and reducing the amount of ITF able to propagate into the central Indian. As seen in the 34.8 salinity contour, both 2011 and 2017 show a reduction of 20 degrees of longitude of ITF westward propagation when compared to climatology. These upwelling regions were caused by both regional winds conducive to Ekman upwelling at that location, in addition to the absence of the annual westward propagating downwelling Rossby wave. This wave was absent during both late 2010 and 2016 due to positive zonal wind anomalies in the south east tropical Indian Ocean caused by a simultaneous occurrence of La Niña and a negative IOD.

# Table of Contents

# List of Figures

# Table of Acronyms

| | |
|---|---|
| **AMOC** | Atlantic Meridional Overturning Circulation |
| **AS** | Anderson and Stigebrandt (2005) |
| **CD** | Chagos Dome |
| **CTD** | Conductivity Temperature Depth |
| **ENSO** | El Niño Southern Oscillation |
| **ETIO** | Eastern Tropical Indian Ocean |
| **GODAS** | Global Ocean Data Assimilation System |
| **HCa** | Heat Content Anomaly |
| **HFa** | Heat Flux Anomaly |
| **ITF** | Indonesian Throughflow |
| **LC** | Leeuwin Current |
| **MBT** | Mechanical Bathythermograph |
| **MSLP** | Mean Sea Level Pressure |
| **NNI** | Ningaloo Nino Index |
| **OHC** | Ocean Heat Content |
| **SCTR** | Seychelles Chagos Thermocline Ridge |
| **SD** | Seychelles Dome |
| **SEC** | South Equatorial Current |
| **SSHg** | Sea Surface Height anomaly from geoid |
| **SST** | Sea Surface Temperature |
| **XBT** | Expendable Bathythermograph |

# Acknowledgments

I would like to thank my advisor Arnold L. Gordon for his support, patience, and guidance over the last five years. I would also like to thank the other members of my committee Andreas Thurnherr and Ryan Abernathey for their thoughtful suggestions and advice.

I would like to thank my mentors within OCP: Claudia Giulivi and Bruce Huber, as well as OCP admin Jean Economos.

NASA and GSAS-Columbia University provided the funding necessary to continue this research.

My fellow graduate students and friends deserve a special thank you: Jean Guo, Genevieve Coffey, Alexandra Boghosian, Rachel Marzen, Hun Baek, Carly Peltier, Julius Busecke, Una Miller, Shanice Bailey, Suki Wong, Lauren Moseley, Maggie Lee, Joann Lee, Kerome Bramwell, Elizabeth Bachman, Lianna Futterman, and Asmi Napitu who also mentored me during my first trip in the field.

Thanks to Mingting Li and Sujata Murty for their insights and collaboration.

Finally, I would like to thank my family for their encouragement and support: my parents Barbara and Dana, my brother Evan, my husband David, all the Gruenburgs, the Dragotta-Pilutkiewicz-Espada family, the Flores family, the Avolios, and my Sherman Street family.

dedicated to Barbara, Dana, Evan, and David

# Chapter 1: Introduction

## 1.1 Global Ocean Circulation and Interbasin Exchange

Although separated by continents into large basins, the global ocean is a web of interconnected pathways. Surface currents combine with intermediate and deeper flows to create a global conveyor belt circulating water in zonal, meridional, and depth space throughout the oceans (Figure 1.1). This global circulation of water has many important functions for Earth's climate, such as carrying equatorial heat poleward, redistributing freshwater, and sequestering carbon at depth (e.g. Ganachaud and Wunsch, 2000; Ganachaud and Wunsch, 2003; Stammer et al., 2003; DeVries et al. 2014). At the surface the Atlantic, Pacific, and Indian Ocean basins are characterized by wind driven subtropical gyres. These regional gyres are connected by overturning circulation which transports heat and freshwater across the equator and between ocean basins. This surface circulation is connected to abyssal flows in the North Atlantic and Southern Oceans, where changes in buoyancy by heat and freshwater exchange cause waters to become dense and sink forming North Atlantic Deep Water and Antarctic Bottom Water.

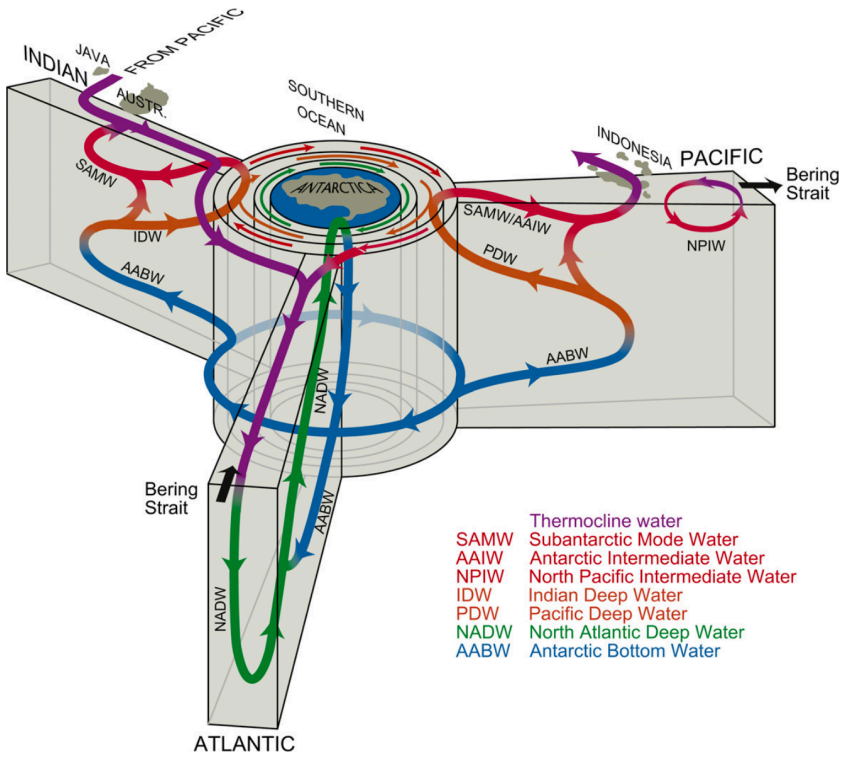


**Figure 1.1** Schematic of global ocean circulation showing the Southern Ocean at the center and clockwise from top left the Indian, Pacific and Atlantic Oceans. Arrows indicate movement of water masses within and between ocean basins. The interbasin exchange of the ITF is shown by the purple arrow leaving the Pacific and entering the Indian Ocean. (Figure from Talley et al., 2011).

In addition to the multilayered flows within each ocean basin, another particularly interesting aspect of this global circulation is the regions of connection between basins. Indian Ocean waters make their way into the Atlantic via eddies shed from the Agulhas Current (Gordon et al. 1985). These rings bring relatively warm, salty Indian Ocean water around the southern coast of Africa into the south Atlantic feeding the Atlantic Meridional Overturning Circulation (AMOC; e.g. Gordon et al., 1992; de Ruijter et al., 1999). The Pacific is linked to

the Arctic by the Bering Strait. Although the total volume transport through this channel is small, it is an important source of freshwater to the Arctic and plays a role in sea ice formation (e.g. Aagaard and Carmack, 1989). Within the Antarctic Circumpolar Current of the Southern Ocean deep waters from the Atlantic, Pacific, and Indian Oceans mix to form Circumpolar Deep Water. Because of the continental topography, all of the oceanic interbasin pathways are located at relatively high latitudes except for one, the Indonesian Throughflow (ITF).

The ITF is unique in its low latitude position, transporting relatively fresh tropical Pacific waters into the Indian via the many straits of the Maritime Continent, the southeast Asian region of island nations between Australia to the south and east Asia to the north, and playing an important role in this global circulation (Gordon, 1986). The ITF is driven by the pressure gradient between the tropical Pacific and Indian Oceans (Wyrtki, 1987). These waters are primarily routed through the Makassar Strait, where the majority of the thermocline transport, and about 80% of the total transport, occurs (Gordon et al., 2010). Deeper waters of about 2.5 Sv pass through the Lifamatola passage to the east (van Aken, 2009). There is some flow via the Karimata Strait, about 1.6 Sv on average (He et al., 2015), although it is minimal due to its shallow depth (~40 m) and seasonal reversal in flow direction. About 15 Sv of ITF exits the Indonesian Seas via the Lombok, Ombai, and Timor Straits and continues into the Indian Ocean (Sprintall et al., 2009).

### 1.2 Indonesian Throughflow in a Regional Context

The Indonesian Throughflow is variable on intraseasonal to decadal timescales and is affected by dynamics of both the Pacific and Indian Ocean basins. The dominant feature over the Maritime Continent is the southeast Asian Monsoon inducing northwesterly winds during the boreal winter months and southeasterly winds during the summer. This affects flow through the

Makassar Strait, as winds push fresher Java Sea water into the southern Makassar Strait during winter, altering the north-south pressure gradient and restricting surface flow (Gordon et al., 2003). Interannual variability in the East Asian Monsoon may also play a role in ITF changes on longer timescales (Murty et al., 2017). At interannual timescales the ITF is affected by ENSO forcing; La Niña conditions tend to cause an increase in ITF transport and El Niño a decrease (e.g. Meyers, 1996; England and Huang, 2005; van Sebille et al., 2014). Additionally, the Indian Ocean Dipole can also affect the ITF by altering the Pacific-Indian pressure gradient (Pujiana et al. 2019).

### 1.3 Indonesian Throughflow in the Indian Ocean

The focus of this work is on the ITF spreading in the eastern tropical Indian Ocean – which pathways it takes and how they change in time. ITF waters are often identified in the Indian Ocean by their characteristic low salinity (Figure 1.2). Waters of up to 60% ITF source are found within the thermocline of the western Indian Ocean (Gordon et al., 1997) indicating transport within the South Equatorial Current (SEC). Modeling studies have shown that ITF is a major contributor to the Agulhas Leakage (Durgadoo et al., 2017), which feeds AMOC. A direct connection between changes in the ITF and Agulhas Leakage is difficult to identify in observations, as the ITF may take a decade for these waters to completely traverse the Indian Basin (Song et al., 2004), but Le Bars et al. (2013) show using ocean models that the presence of the ITF acts to increase the Agulhas Leakage.

Recent studies have shown that increases in the ITF can cause heating in the upper water column in the Indian Ocean (Nieves et al., 2015; Lee et al., 2015; Zhang et. Al., 2018). This can affect air sea-interaction and in turn, the development of the Asian monsoon. Vidya et al. (2020) showed this during the 1998-2016 ‘global warming hiatus’ as an increase in ITF advection

caused increases in upper ocean heat and SST in the southern Indian Ocean, which weakened the cross equatorial atmospheric pressure gradient and cross-equatorial winds associated with the monsoon (Vidya et al., 2020),

We aim to build on studies like these, by looking more in detail at the pathways of the ITF from the Makassar Strait to the Indo-Australian basin to the central Indian Ocean. As we track the ITF using anomalous upper ocean heat and characteristic thermocline salinity, we aim to understand both how variability at one point on this path can affect the next, and how regional forcing can alter these pathways.

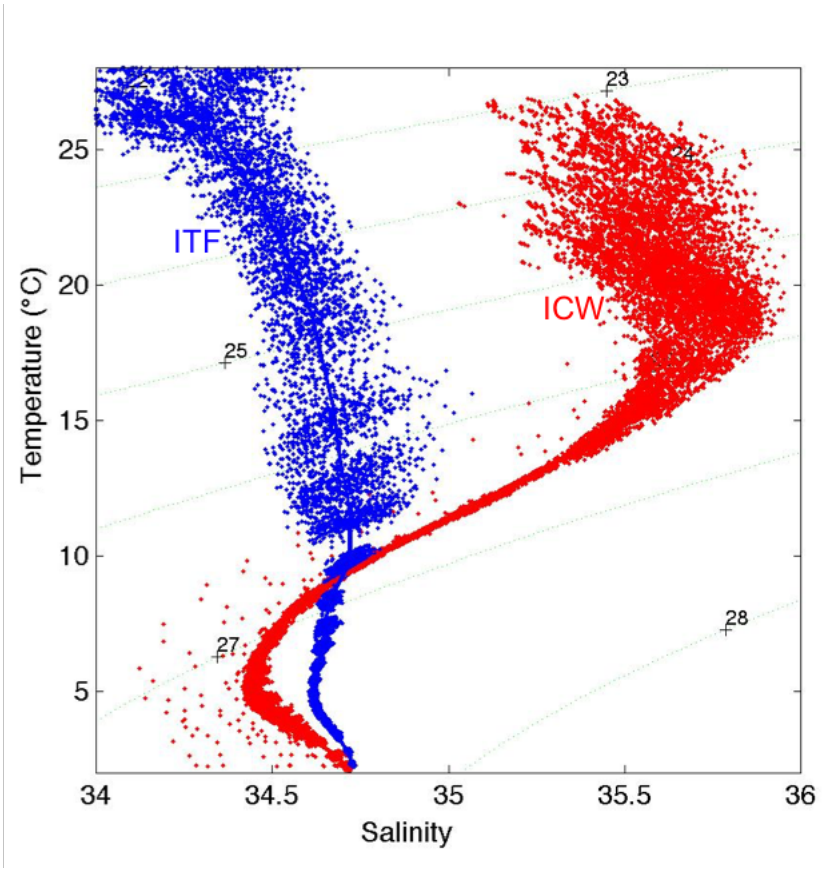


**Figure 1.2** Temperature and salinity diagram showing Indonesian Throughflow waters in blue and Indian Central Water in red. Indian Central Water is shown here as Argo T/S profiles across

25.5°S at 61.5°SE, 70.5°E, 79.5°E, and 88.5°E. ITF water is plotted as Argo T/S profiles at 112.5°E and 10.5°S , 11.5°S, 12.5°S, and 13.5°S. The characteristic low salinity of the ITF is seen here in the near linear nature of the plot in salinity space, with points scattered around 34.6.

Chapter 2 examines the heat flux through the Makassar Strait, the primary pathway of the ITF, during two observation campaigns spanning 2004-2011, and 2013-2017 and identifies its connection to the upper ocean heat content (OHC) in the eastern tropical Indian Ocean[1]. Composite La Niña, El Niño, and neutral temperature profiles are constructed using all available CTDs within the strait as well as MBT, XBT, and profiling float measurements, while mooring observations provide velocity with depth. Upper ocean heat content in the Indian Ocean ITF outflow region is determined using gridded Argo profiles. During La Niña (El Niño) the thermocline deepens (shallows) and the velocity maximum shoals (deepens), increasing (decreasing) the flow of warm upper ocean waters through the Makassar Strait. Variability in the heat flux is primarily influenced by changes in velocity while changes in the temperature stratification play a lesser role. The heat flux in the upper layer (0-300 m) is the dominant factor in the total depth integrated (0-720 m) heat flux. Upper ocean (0-300 m) heat content in the eastern tropical Indian ocean is well correlated with the Makassar heat flux at interannual time scales and indicates that changes within this important ITF passage can impact the eastern Indian.

[1] Gruenburg, L.K., and A.L. Gordon. 2018. Variability in Makassar Strait heat flux and its effect on the eastern tropical Indian Ocean. *Oceanography* 31:80-87.

Chapter 3 investigates the ITF outflow into the Indian Ocean from the Indo-Australian basin via the Leeuwin Current (LC) or South Equatorial Current. Using Argo gridded data, upper ocean heat content is tracked from the immediate ITF outflow area to the source regions of the SEC and LC. GODAS reanalysis is used to examine current velocities in these two regions. NCEP/NCAR reanalysis provide mean sea level pressure (MSLP) and near surface winds for the surrounding region. Heat content changes in the immediate ITF outflow region are reflected five months later in the SEC region, except during 2011. During this time a positive heat content anomaly is deflected from the SEC region and enhances OHC in the LC region. MSLP reveals an anomalous low pressure center off the west Australian Coast and resulting weakened southerly winds over the Leeuwin region and positive zonal wind anomalies over the SEC. These findings are consistent with the Ningaloo Niño of 2011. The strengthened LC during this time is in agreement with past studies of the marine heatwave in this region. The SEC also shows velocity changes, with a weakening of westward flow resulting in a reduction of heat propagation into the central Indian. To compare with 2011, we examine the same parameters during the Ningaloo Niño event in 2000. Although this 2000 event was somewhat weaker, we find similar anomalous atmospheric and oceanic circulation. These results show how the Ningaloo Niño plays an important role in the partitioning of the ITF between the SEC and LC pathways.

Chapter 4 explores the westward propagation of the ITF within the thermocline of the South Equatorial Current on seasonal and interannual time scales. The depth of the 20°C isotherm is used to investigate the role of the Seychelles Chagos Thermocline Ridge (SCTR) . Examination of the seasonal cycle reveals the importance of the SCTR development on westward ITF propagation, especially during austral winter months. Two time periods of

unusually salty water area discovered during 2010/11 and 2016/17 indicating reduced westward ITF transport within the SEC. Both of these years show anomalous upwelling centers in the middle of the Indian Ocean basin during austral summer, out of season for the normal SCTR strengthening during austral winter. Subsurface velocity from GODAS shows that these upwelling centers induced cyclonic circulation that disrupted the normal zonal path of the SEC. These two time periods were marked by an absence of the annual westward propagating downwelling Rossby wave in late 2010 and 2016. This was due to the presence of positive zonal wind anomalies in the south east tropical Indian Ocean linked to simultaneous La Niña and negative IOD conditions. The result for ITF propagation was a plume nearly 20 degrees of longitude further to the east than climatology for both 2010/11 and 2016/17 as determined by the 34.8 salinity contour.

Chapter 5 will provide conclusions and a discussion of future work regarding the ITF propagation within the Indian Ocean further from the outflow region.

# Chapter 2: Variability in Makassar Strait Heat Flux and its Effect on the Eastern Tropical Indian Ocean

*Published as L. Gruenburg and A.L. Gordon. 2018. Variability in Makassar Strait Heat Flux and its Effect on the Eastern Tropical Indian Ocean. Oceanography, 31, 80-87.*

**Note:** The text below is a slight modification of Gruenburg and Gordon (2018) by adding Figures 2.5, 2.6 and associated text.

**Abstract**

Heat flux anomaly (HFa) within the Makassar Strait is investigated using observed velocity time series and ENSO scaled temperature profiles. Direct measurements of velocity from 40 to 740 m were recorded 2004-2011, and 2013-2017 during the INSTANT and MITF NOAA-OCO programs. The velocity profile is thermocline intensified with V-max near 100 m. In situ temperature measurements during 2004-2006 and ship based CTD profiles during these two monitoring campaigns were combined with all available World Ocean Database CTD, OSD, MBT, and XBT data within Makassar Strait since 1950 to create representative temperature profiles for positive, negative, and neutral phases of ENSO. The Makassar velocity profile displays a stronger (weaker), shallower (deeper) V-max, and a deeper (shallower) thermocline during La Niña (El Niño). Southward Makassar HFa increases rapidly from 2006 to 2008 with a peak of 0.13 PW in 2008 and 2009. Afterwards, Makassar HFa slowly decreases to a minimum of -0.25 PW (less southward) during 2015, after which southward heat flux beings to climb again. Variability in depth integrated volume transport, surface to 740 m, explains 57% of HFa variance. However, the total volume transport does not reflect the relative contributions of the warm upper and cool lower layers. Changes in the depth dependent velocity profile explain 72%

of HFa variance whereas temperature profile variability explains 28%. The impact of Makassar HFa variability on the Indian Ocean is assessed through comparison with the heat content anomaly (HCa) in an Eastern Tropical Indian Ocean box (ETIO; 101.5°E-105.5°E, and 9.5°S-15.5°S) using gridded Argo data. The ETIO HCa follows a similar pattern (R=0.83) when lagged 30 months behind the Makassar HFa. Although well correlated a notable discrepancy between the two time series is present in the ETIO in 2012/13, possibly owing to a shift of ITF from the dominant SEC pathway to a southward Leeuwin track.

## 2.1 Introduction

The ocean heat content is markedly increasing as anthropogenic induced warming of the atmosphere is transferred by air-sea interaction into the water column. The ocean holds 93% of the anthropogenic heating from 1955 to 2010 (Levitus et al., 2012). Ocean uptake of heat depends on the difference between air and sea surface temperatures, as well as the wind speed, both of which vary spatially and temporally in response to the many climate oscillations spanning a broad range of time scales. A key part of the ocean heat uptake occurs in the tropical Pacific Ocean, which varies in response to the El Niño Southern Oscillation (ENSO; England et al., 2014) and longer period oscillations, such as Pacific Decadal Oscillation (PDO; von Känel et al., 2017). During La Niña the sea surface temperature (SST) in the central and eastern tropical Pacific Ocean are colder than during El Niño conditions. In addition, the trade winds are stronger during La Niña (England et al., 2014). These factors result in the Pacific tropical expanse being more effective at absorbing atmospheric heat, which attenuates atmospheric warming during La Niña conditions (Kosaka and Xie, 2013). The oceanic heat spreads both poleward and zonally into the Indian Ocean by the Indonesian Throughflow (ITF; Lee et al., 2015). Here we use

observations to investigate the interocean heat flux fluctuations accomplished by the ITF during the period 2004-2017 and the impact on the heat inventory in the eastern tropical Indian Ocean.

The Indonesian throughflow (ITF) advects ~15 Sv (Sv = $10^6$ $m^3$/sec) of tropical Pacific water into the eastern tropical Indian Ocean (ETIO; Gordon et al., 2010), spreading as a distinct low salinity plume across the Indian Ocean within 10-15°S (Gordon et al. 1997). The ITF plays an important role in the ocean-climate system (e.g. Schneider & Barnett, 1997; Sprintall et al., 2014) and has been shown to affect the Indian Ocean stratification (eg. Song and Gordon, 2004; Liu et al., 2015; Feng et al., 2015).

Approximately 77% of ITF waters flow through Makassar Strait (Makassar throughflow of 11.6 Sv versus 15 Sv during the INSTANT program 2004-2006 Gordon et al., 2010). Makassar Strait transport, which has been monitored with some gaps in time from 1996-2017, displays seasonal and interannual fluctuations. The Makassar velocity profile displays a marked velocity maximum (V-max) within the upper thermocline. During the summer months (southeast monsoon) there is an increase in maximum velocity while a decrease is present during the beginning of the northwest monsoon (Gordon et al., 2008; Susanto et al., 2012; Gordon et al., 2012). The velocity profile in Makassar Strait also changes with ENSO phase, with increased velocity within the warm upper thermocline during La Niña and reduced velocities during El Niño (Gordon et al., 2008; Gordon et al., 2012). In addition to this shifting velocity profile, temperature within Makassar Strait also varies with ENSO. Ffield et al. (2000) compared XBT based Makassar temperature at 100 m to Niño3 and Niño4 indices finding correlations of -0.80, and -0.82 respectively (negative correlations indicating cooler temperatures, shallower thermocline, during positive ENSO phase). Susanto et al. (2012) found a correlation between Makassar average temperature 120-420 m and Niño3.4 of -0.78.

This ENSO dependence is linked to the movement of the North Equatorial Current (NEC) bifurcation, which shifts between 10°N and 15°N (Qiu and Chen, 2010). During El Niño the NEC bifurcation shifts northward, increasing leakage from the Pacific through the Luzon Strait into the South China Sea (SCS) which drives relatively fresh buoyant SCS waters through the Sulu Sea and into the Sulawesi Sea where they form a 'freshwater plug' inhibiting Makassar throughflow in the upper ~70 m (Qiu and Chen, 2010; Gordon et al., 2012; Gordon et al., 2014). The reverse conditions are present during La Niña. Recent studies have also shown the importance of salinity in driving the ITF. Hu and Sprintall (2016) separated the effects of salinity on ITF transport and found a contribution to total variability of about 36%. Rainfall variability over the Maritime Continent may contribute significantly to these salinity changes, as Hu and Sprintall (2017) suggest that increased rainfall in this region leads to elevated ITF transport.

After passing through the Makassar Strait, ITF waters exiting the Indonesian Seas are injected into the ETIO through three primary pathways: Lombok Strait, Ombai Strait, and Timor Passage. These three portals also exhibit strong seasonal and interannual variability (Sprintall et al., 2009). Using a numerical model Song and Gordon (2004) show decreased SST in the ETIO when the Makassar ITF transport profile is altered within its observed range. Another model study by Lee et al. (2015) suggests that ITF effects may not be limited to the eastern Indian region. They show that increases in Makassar heat flux during the warming hiatus are reflected in increasing heat content in the upper (>700 m) of the Indian Ocean. Furthermore, a variable ITF has the potential to affect Atlantic Meridional Overturning Circulation (AMOC). In two more model simulations Durgadoo et al. (2017) propose that 45% of Agulhas Leakage waters

originate from the ITF, and Le Bars et al. (2013) conclude that the Agulhas Leakage is increased by 3 Sv when the ITF is present compared to a closed Indonesian Seas scenario.

Longer time series of Makassar throughflow data 2004-2011, 2013-2107 from the International Nusantara Stratification and Transport (INSTANT), and the Monitoring Indonesian Throughflow National Oceanographic and Atmospheric Association Ocean Climate Observation (MITF NOAA-OCO) programs now allow for more detailed investigation of the ITF which can help to validate these model simulations and provide an observation based foundation for further study of how ITF variability can affect the Indian Ocean and climate.

In this study we consider the heat flux anomaly (HFa) within the Makassar Strait calculated using observed time varying velocity and temperature profiles. We compare the Makassar HFa time series to the heat content anomaly (HCa) within the ETIO observed by Argo floats.

## 2.2 Makassar Data

### 2.2.1 Velocity

Velocity measurements were recorded by moored ADCPs deployed within the 45 km wide Labani Channel located at 2.86°S, 118.62°E. in Makassar Strait during 1996-1998, 2004-2011 and 2013-2017 as part of the Arlindo, and INSTANT and MITF NOAA-OCO programs respectively (Figure 2.1; Gordon et al. 2008, Gordon et al. 2012). For this study data from 2004 onward are considered, as earlier measurements only capture velocities above 400 m and we seek to investigate heat flux above the sill depth (values to 740 m are used to encompass the sill depth of 680 m) in the southern Makassar Strait. For the 2004-2017 time period velocity measurements

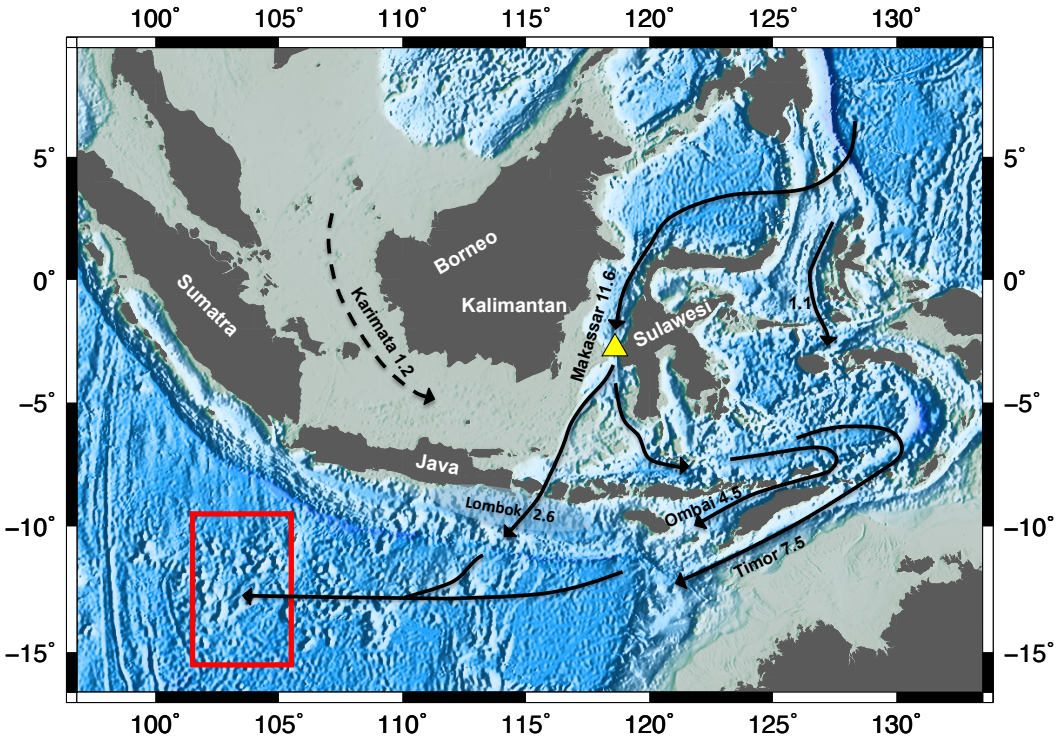


**Figure 2.1** The Makassar Strait and ETIO outflow region. The mooring location within the Labani Channel is indicated by the yellow triangle. The ETIO box bounded by 101.5°E through 105.5°E and 9.5°S through 15.5°S is shown by the red rectangle. Arrows indicate the pathway of ITF waters, starting at the Pacific inflow and finishing in the ETIO box. Volume transports in Sv ($10^6$ $m^3s^{-1}$) from the INSTANT program 2004-2006 (Gordon et al. 2010) are indicated at each passage, with Karimata transport in dashed line (Fang et al. 2009).

were interpolated to hourly intervals at 20 m depth levels from 40 to 740 m. Velocities were only available below 40 m. For the surface layer the velocity measurement at 40 m was applied. This is one of 4 methods for extending velocity measurements from the topmost measurement to the surface described in Vranes et al. (2002). The method used here is less likely to

systematically over or underestimate surface layer velocities than linear extrapolations to the surface described in the other 3 methods. The Labani channel axis is aligned at a slight angle, ~170°, of due south. The along axis velocity, marking the Makassar Strait throughflow, was determined from the geographic zonal and meridional speed rotated counterclockwise by 10° (as in Gordon et al., 2008; Susanto et al., 2012; Figure 2.2). In order to remove tidal fluctuations and reflect the same temporal resolution as Argo data used in the ETIO region, the final along channel velocities were averaged monthly.

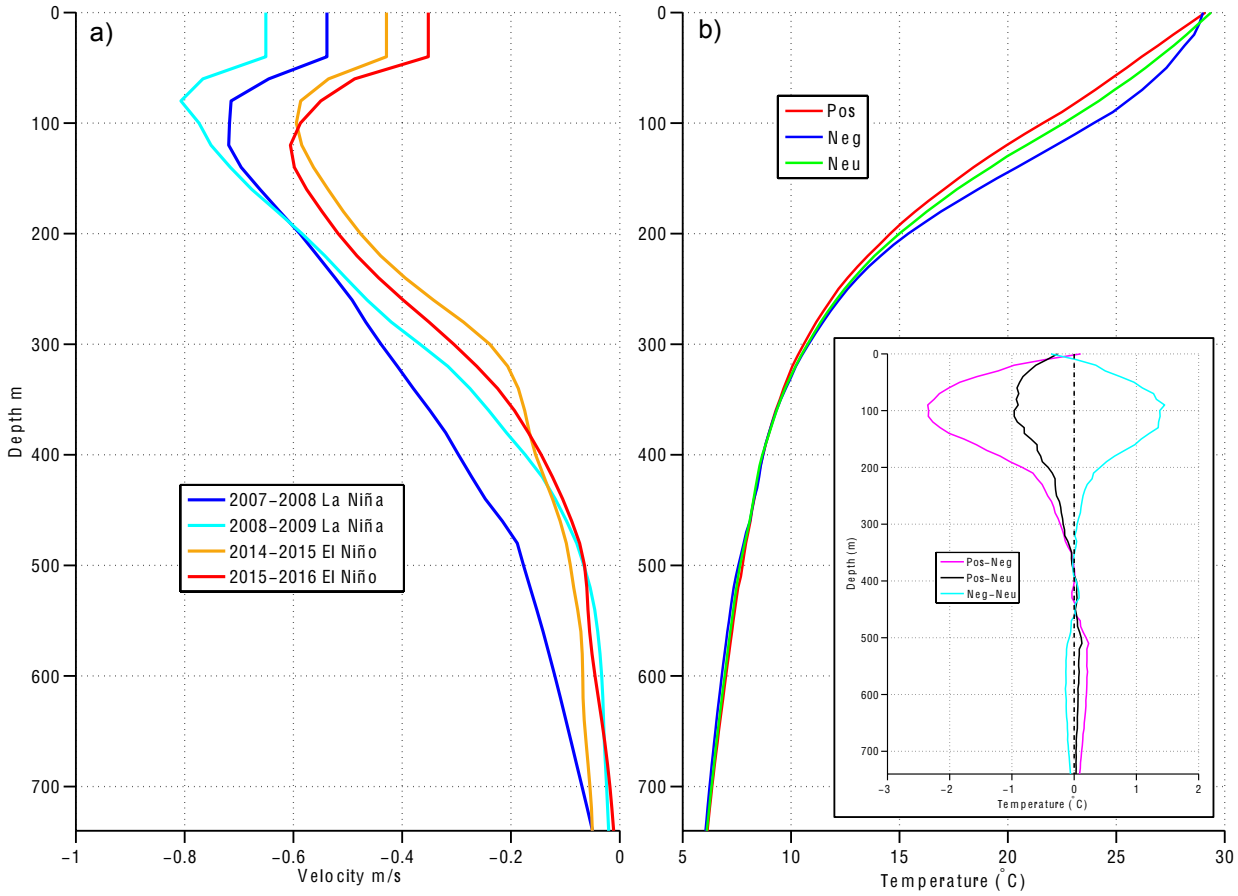


**Figure 2.2** Makassar velocity and temperature profiles. a) Averaged Makassar velocity profiles July-June for 4 years, two representing La Niña years (dark blue 2007-2008, light blue 2008-2009), and two representing El Niño years (orange 2014-2015, red 2015-2016) Negative velocity indicates southward flow. During La Niña (El Niño) years the velocity maximum is larger

(smaller) and it occurs at shallower (deeper) depth. b) Makassar temperature profile composites for El Niño (red), La Niña (blue), and neutral (green). Deepening of the thermocline approximately 10-350 m is present during La Niña with the opposite during El Niño 0-380 m. b) inset Positive ENSO phase temperature profile minus negative profile (purple), positive minus neutral (black), and negative minus neutral (blue). The largest temperature differences are in the surface and thermocline with negative (La Niña) temperatures 2.4 °C warmer than positive (El Niño) temperatures at 90 m.

### 2.2.2 Temperature

To ensure that full variability in Makassar heat flux anomaly is captured, the variable temperature profile, in addition to the velocity profile must be addressed. A deeper thermocline during La Niña will strengthen the established pattern of shallower, faster velocities (increased heat flux), with opposite conditions during El Niño. Estimates of Indonesian throughflow heat flux made with the benefit of continuous in-situ temperature data are only possible during 2004-2006. Using a climatology temperature profile for the remaining velocity time series 2006-2011, 2013-2017 could underestimate (overestimate) heat flux during La Niña (El Niño) thus decreasing heat flux variability. This study uses in-situ temperature data combined with the Niño3.4 climate index to approximate a variable temperature profile to capture the increased variability in Makassar heat flux.

To investigate the changes in the temperature profile in Makassar Strait during different ENSO stages CTD data from 7 Makassar Strait cruises spanning 1993-2017 totaling 50 profiles were used in combination with continuous temperature profiles measured from 2004 through 2006 as part of the INSTANT program. Additional temperature data including 9 CTDs, 26

profiles from ocean stations, 89 profiles from profiling floats, 37 MBTs and 358 XBTs from the World Ocean Database (Boyer et al., 2013) were also used. The ENSO phases were determined by the Niño3.4 climate index (National Oceanic and Atmospheric Administration, 2017).

Following the ENSO phase temperature profiles were coded as negative (La Niña), neutral, or positive (El Niño), depending on the date the measurement was taken. Negative was defined as Niño3.4 less than -0.5, neutral as between -0.5 and 0.5 inclusive, and positive as greater than 0.5. During 2004-2006 continuous temperature profiles were recorded, though due to mooring movement many values in the surface layer could not be used. This data was collected every 6 minutes and was averaged into daily intervals. In order to determine shallow temperatures, sea surface temperature (SST) from the NOAA Optimally Interpolated SST (OISST) dataset (Banzon et al., 2016) was used for the same time period. This daily data is at 0.25° resolution and the grid box that encompassed the mooring site was used for all further calculations. At each time step in the 2004-2006 Makassar temperature time series an associated SST was appended to the top of the profile. A piece-wise cubic interpolation was used to interpolate between the surface and the uppermost measurement. The 3 ENSO phase temperature profiles were created using a bootstrap approach. For each of the three profiles a temperature profile was chosen at random from all available temperatures (266 for negative, 374 for positive, and 952 for neutral), recorded, and then placed back into the pool of available temperatures. This process was repeated 10,000 times for each ENSO phase. The resulting mean profiles are shown in Figure 2.2. A temperature time series 2004-2017 was created be applying each representative profile to the ENSO phase recorded in the Niño 3.4 index. Although this method seeks to improve heat flux calculations made using a climatology temperature profile it is limited by a lack of continuous temperature data over many ENSO cycles. Because of this we are

unable to determine how developing and decaying phases of ENSO may affect the Makassar temperature profile differently.

## 2.3 Results and Discussion

### 2.3.1 ENSO based Temperature reconstruction

Representative profiles for each of the ENSO states are shown in Figure 2.2. Significant differences are evident, especially within the thermocline. The expected pattern is present with a shallower thermocline during El Niño and a deeper one during La Niña. Positive ENSO events are linked with cooler temperatures (compared with neutral conditions) from 0 to 380 m with a maximum cooling of 1.0 °C at 110 m depth. Negative ENSO events are associated with warmer temperatures (compared with neutral) from 10 to 350 m with a maximum warming of 1.5 °C at 90 m depth. La Niña conditions reflect warmer temperatures than El Niño conditions from 10 to 370 m. The largest temperature difference between profiles occurs within the thermocline at 90 m depth where the positive profile is 2.4 °C cooler than the negative profile.

### 2.3.2 Heat Flux/Heat Content

Heat flux was calculated in the Makassar Strait using velocity profiles from section 2.2.1 above combined with the ENSO based temperature time series from section 2.2.2 above. Heat flux was calculated as follows

$$Heat\ Flux = \int_{740}^{0} \rho v A C_p\,(\theta - \theta_{ref})\,dz \qquad [1]$$

Where ρ is a mean density profile, v is the along channel velocity profile, A is the cross sectional area of the depth bin at the mooring location determined from a combination of observed bathymetry recorded during the Labani Channel mooring rotation of 2009 and Smith and Sandwell topography (Smith & Sandwell, 1997) (http://topex.ucsd.edu/marine_topo/), $C_p$ is the specific heat of seawater, estimated here as 4000 J/kgC, $\theta$ is time varying temperature profile

determined in section IIb, and $\theta_{ref}$ is a reference temperature, 0 °C was used.

Vranes et al. (2002) provides mean Makassar heat flux estimates using 5 different reference temperatures with results ranging 0.18 PW. Understanding the difficulty in choosing an appropriate closure point for our system, we use a reference temperature of 0 °C and only consider heat flux anomalies to alleviate inconsistencies in reference temperature choice. These values are multiplied together and integrated over the 0-740 m layer at each one-month time step. The mean heat flux was subtracted from each data point in the time series to create a heat flux anomaly time series. A 13-month running mean was applied to remove the seasonal cycle and identify interannual variability and long-term trends.

The heat content was calculated for a region of the ETIO, a box bounded by 101.5°E to 105.5°E and 9.5°S to 15.5°S inclusive. The ETIO box represents the furthest west portion of the ITF outflow area identified by Andersson and Stigebrandt (2005) termed the 'downstream buoyant plume'. As we investigate the effects of the ITF on the Indian Ocean, we choose to examine this box as it is already known to contain ITF water (Gordon et al., 1997) and provides the most direct connection back to the Makassar Strait. The most westward portion of this box was chosen as a way to avoid shorter term variability that may arise from Makassar water exiting through the 3 main export passages at various times and rates (Sprintall et al. 2009 discusses these exit passages in detail), and to avoid regions of coastal upwelling. Ideally an investigation of heat content along the entire path Makassar water travels through the Indonesian Seas and into the ETIO would be performed, but we are limited by the lack of continuous observations. The Argo profiler dataset used here does not resolve the Indonesian Seas. The ETIO box we have chosen balances proximity to the ITF outflow area with sufficient data coverage. Heat content

was calculated using a gridded 1° by 1° monthly Argo dataset (2005-2017) from the Asia Pacific Data Research Center (2017). The following equation was used to determine heat content

$$Q = \int_{740}^{mld} \rho C_p \theta \, dz \qquad [2]$$

Where ρ is a mean density profile, $C_p$ is the specific heat of seawater, estimated here as 4000 J/kgC, and $\theta$ is temperature. In order to focus on subsurface variability, heat content within the mixed layer was not included in the total heat content. Argo based mixed layer depths (mld) were provided by the Asia Pacific Data Research Center (2017). These values were multiplied together and integrated over the bottom-of-mixed-layer through 740 m layer at each one-month time step. The mean was subtracted from the resulting dataset to examine only anomalies and a 13-month running mean was applied to the time series.

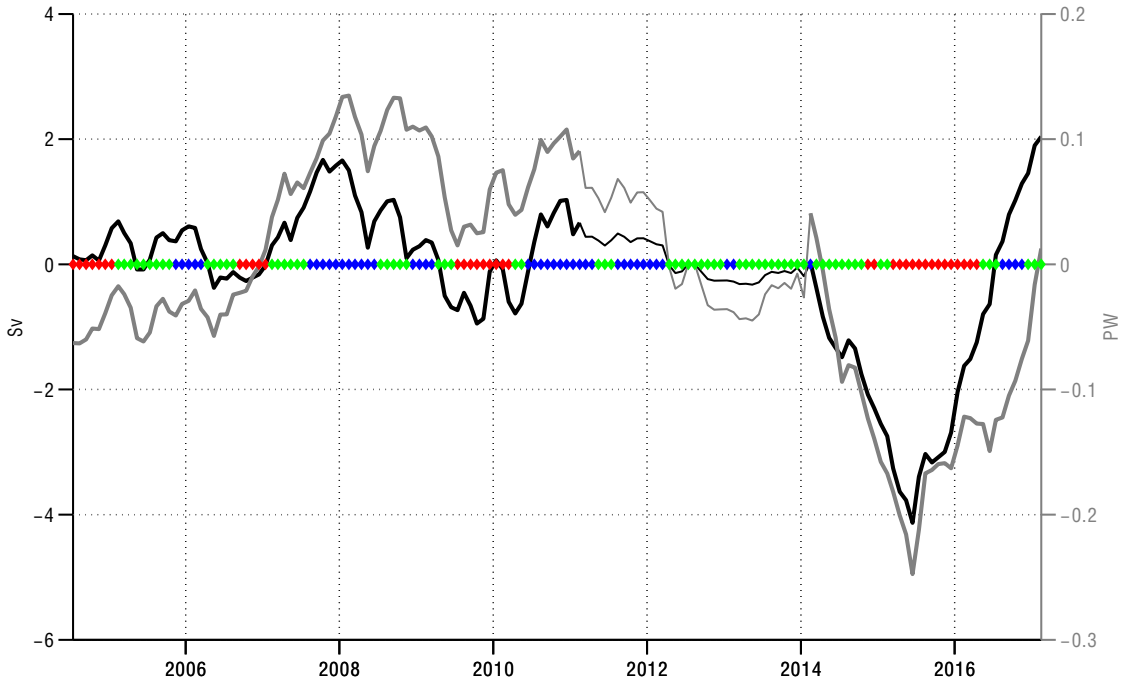


**Figure 2.3** Makassar Strait transport anomaly (thick black line, Sv = $10^6$ $m^3s^{-1}$) and heat flux anomaly (thick grey line) from observations. Transport and heat flux estimations determined

using Li et al. (2018) are in the thin black line and thin grey line respectively. Time series are shown with a 13-month running mean. Positive values indicate increasing transport or heat flux to the south. The correlation coefficient between these two time series is 0.76. Although the volume transport is important in driving heat flux anomaly, it is not the sole factor determining HFa variability. ENSO phase from Niño 3.4 (National Oceanic and Atmospheric Administration, 2017) used to construct temperature profile is shown in red (positive), green (neutral), and blue (negative) markings along the zero anomaly line.

The heat content anomaly in the ETIO box is a continuous monthly dataset from 2005-2017. The Makassar heat flux anomaly time series is continuous from 2004-2011 and 2013-2017 with missing data for much of 2011 and 2013, and all of 2012. Before comparing these two datasets we sought to patch this gap. The heat flux anomaly in Makassar Strait is well correlated with the volume transport anomaly 0-740 m with an R-value of 0.76 (Figure 2.3). Li et al. (2018) produces a reconstructed 0-300 m Makassar transport from 1948-2016 using Pacific zonal wind speed square anomalies in a neural network framework. When the same 13-month running mean is applied to the 0-300 m Makassar transport anomaly from Li et al. (2018) it is well correlated (R=0.82) with the 0-740 m transport anomaly observations during their over-lapping time period (2004-2011, 2013-2016). Similarly, this reconstruction is well correlated with the observed heat flux anomaly during the over-lapping time period (R=0.72). As the Li et al. (2018) 0-300 m transport represents the observed transport variability quite well, and both the observed and reconstructed transports track the heat flux anomaly, we use the Li et al. (2018) 0-300 m reconstruction to fill in the 2011-2013 heat flux anomaly gap. The mean ratio of observed heat flux anomaly to reconstructed 0-300 m Makassar transport anomaly from 2004-2011 and

2013-2016 was calculated (0.18 PW/Sv). For each missing month of data from 2011-2013 the reconstructed 0-300 m Makassar transport anomaly was multiplied by the ratio to create a heat flux anomaly estimate which was used to fill in the gap (see green line in Figure 2.4).

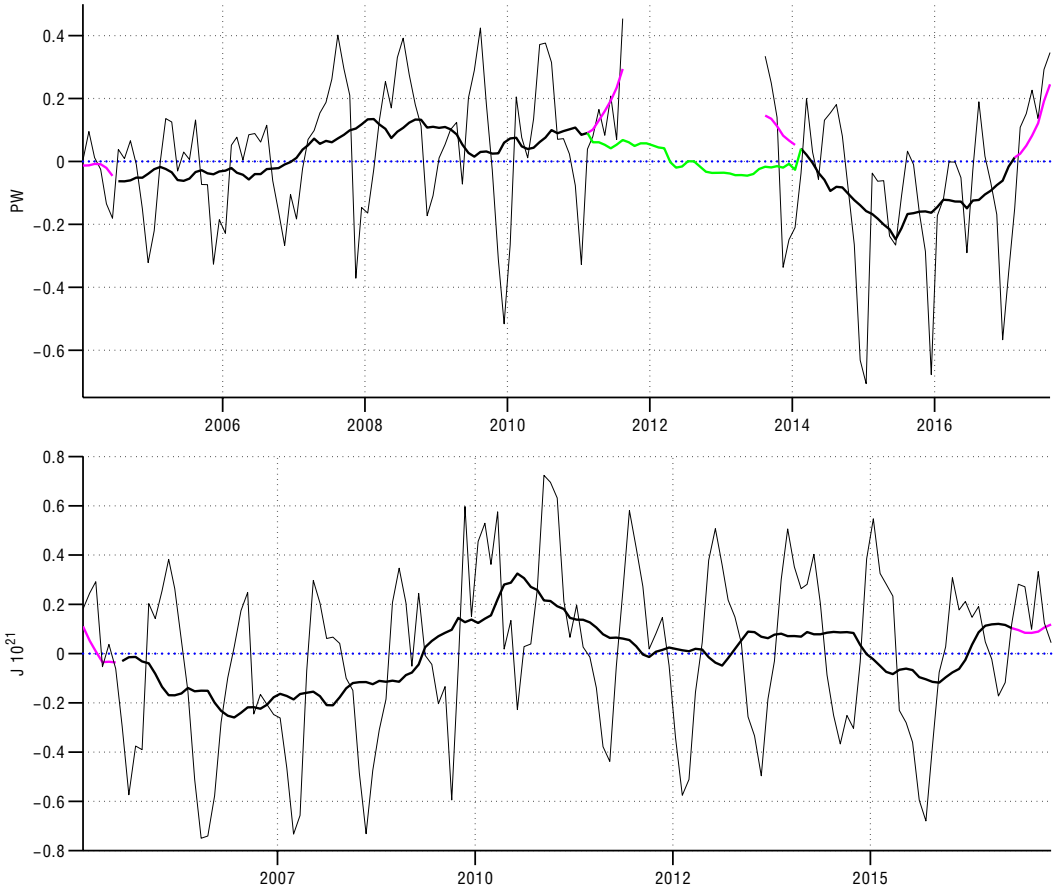


**Figure 2.4** *Top* Heat flux anomaly in Makassar Strait 2004-2017. Monthly means (grey), 13-month running mean (black), portion removed before correlation (purple), gap filled using heat flux anomaly to volume transport anomaly ratio and Li et al. (2018) 0-300 m transport (green). Positive values indicate increasing heat flux anomaly south. Large seasonal cycle is clearly visible in monthly means. Maximum heat flux anomaly south of 0.13 PW during February of 2008 and minimum of -0.25 PW during June 2015. *Bottom* Heat content anomaly in the ETIO box during the Argo era 2005-2017. Monthly means (grey), 13-month running mean (black),

portion removed before correlation (purple). Maximum heat content anomaly of $0.33^{21}$ J occurs in July 2010 and minimum of $-0.26^{21}$J happens in December 2006.

### 2.3.3 Makassar to ETIO Comparison

As the Makassar Strait contains about 77% of the total ITF (Gordon et al. 2010) and no continuous long-term measurements of major exit passages exist, it is appropriate to consider how the outflow region in the ETIO would be affected by changes in the Makassar Strait.

A time varying cross correlation is applied to the Makassar heat flux anomaly time series and the ETIO box HCa. At a time step of zero the ETIO box time series begins in January 2005 and the Makassar time series in January 2005, The ETIO box time series is shifted back at one-month intervals and an associated correlation is calculated, for example the second correlation would be calculated with the ETIO box time series beginning in January 2005 and the Makassar in December 2004. In this manner the time lag between Makassar heat flux anomaly events and potentially connected ETIO HCa changes is lengthened with every consecutive correlation calculation. Significance of the correlations was determined using the bootstrap approach described by Martinson (2018). Due to the application of the 13-month running mean, the first and last six months of data from each time series were removed before performing the correlations.

### 2.3.4 Makassar Heat Flux and ETIO Heat Content

Makassar heat flux anomaly time series is shown in Figure 2.4. The time series shows large seasonal variability with the average difference between minimum boreal winter heat flux south and maximum summer heat flux south of 0.65 PW. This is a result of the seasonal nature of the Makassar volume transport, which is characteristically greatest during summer months and

weakest during winter (Susanto et al. 2012). Following the application of the 13-month running mean to remove the seasonal cycle, the maximum heat flux anomaly south is 0.13 PW during February of 2008 and minimum is -0.25 PW during June 2015 (positive values indicating increasing heat flux southward). Heat flux anomaly is very highly correlated with volume transport anomaly (R=0.76; Figure 2.3). This volume transport explains approximately 57% of the variance in heat flux anomaly, indicating that the variability in the temperature and velocity profiles also significantly effects heat flux anomaly. When the upper and lower layer volume transports are plotted with the HFa (figure 2.5) the importance of the 0-300 m layer becomes apparent. In figure 2.5 a clear trend in HFa is apparent, with larger positive (increasing HFa to the south) values when upper layer transport is high and larger negative (decreasing HFa to the south) when this transport is low. The upper layer transport is correlated with the total depth integrated HFa with r = 0.94 (figure 2.6). This confirms the importance of the upper layer, with its larger mean transport and larger variability in both velocity and temperature, on heat transport through the Makassar Strait.

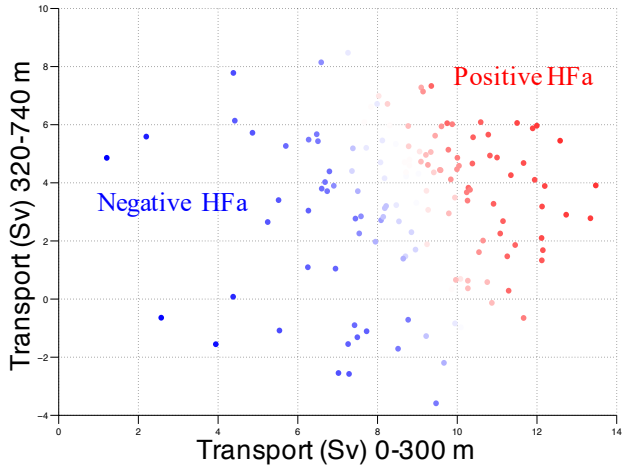


**Figure 2.5** Makassar Strait volume transport, positive values indicate increasing transport to the south, in the upper (0-300 m) layer on the x-axis and lower (320-740 m) layer on the y-axis.

Color indicates total (0-740m) HFa with warm colors indicating positive (increasing heat flux to the south) HFa and cool colors negative HFa (decreasing heat flux to the south). Positive HFa is associated with increasing upper layer transport and negative HFa with decreasing upper layer transport. Changes in lower layer transport are not associated with trends in HFa.

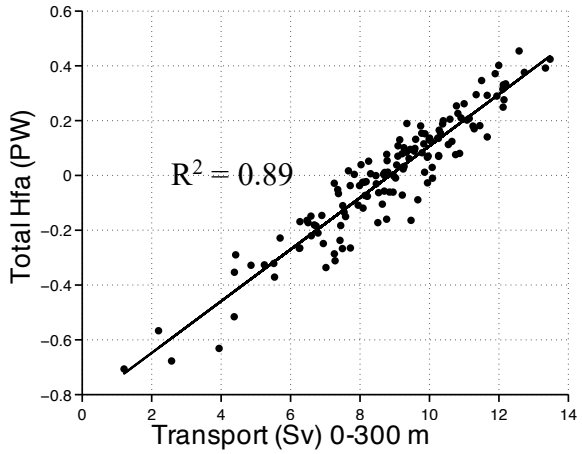


**Figure 2.6** Upper layer (0-300 m) Makassar Strait volume transport on the x-axis and total (0-740 m) HFa on the y-axis. The two are well correlated with $r^2$=0.89. Total HFa primarily depends on variability in the upper layer volume transport.

To determine the impact of the velocity and temperature profiles, heat flux was calculated twice more, once using a mean velocity profile and variable temperature profile, and once using mean temperature and variable velocity profiles. These new heat flux estimates indicate that changes in the velocity profile account for 72% of the variance in total heat flux, whereas the temperature profile changes only account for 28%. During La Niña the velocity maximum shallows, the maximum speed increases, and the isotherms deepen, increasing both the amount of water flowing through the channel and the temperature of that water. The opposite happens in El Niño.

Figure 2.4 displays ETIO box heat content anomaly. Similar to Makassar heat flux, ETIO box heat content anomaly also presents a seasonal cycle. This seasonal cycle shows larger values during (austral) summer and smaller values during late winter. The average difference between summer and winter heat content is $0.97^{21}$ J. After the 13-month running mean is applied, heat content anomaly within this box reaches its maximum of $0.33^{21}$ J during July 2010 and the minimum of $-0.26^{21}$ J during December 2006.

The best correlation between the Makassar HFa and ETIO box HCa is R=0.83 with a p-value of $10^{-4}$ at a lag of 30 months (Figures 2.7,2.8). This is consistent with signal composed of advection and eddy transport, with Makassar waters winding their way through the Indonesian Seas and exiting into the ETIO around 2.5 years later.

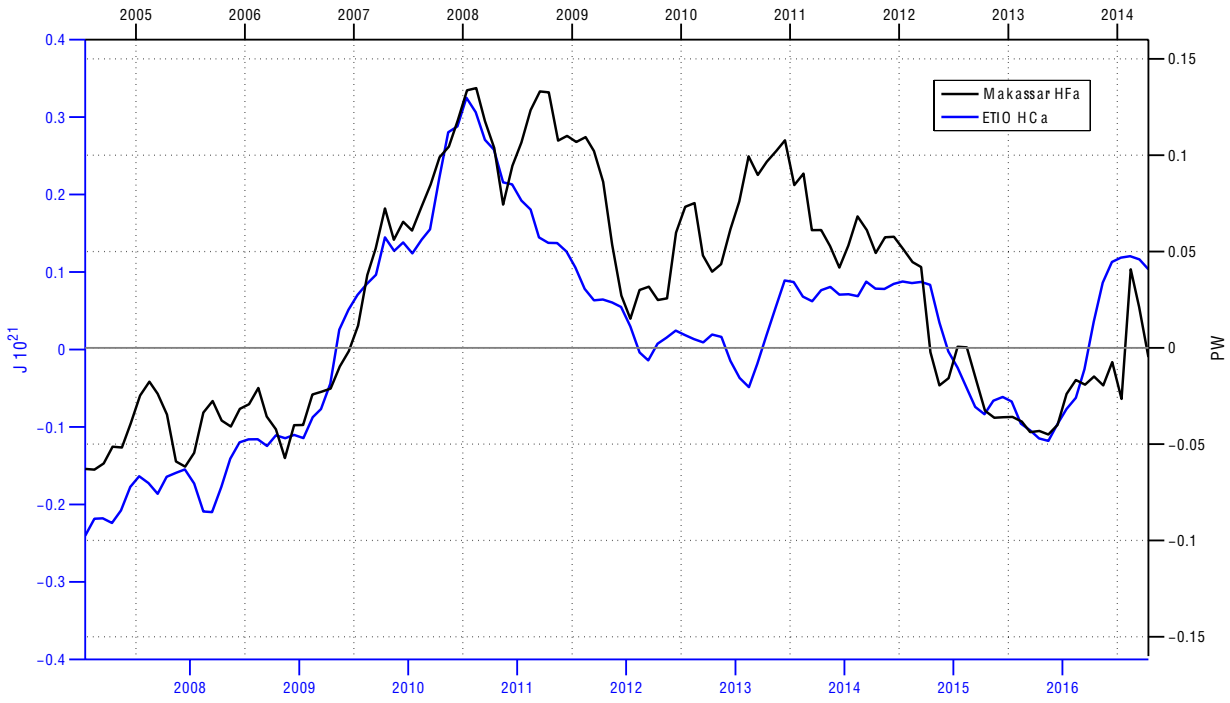


**Figure 2.7** Heat flux anomaly in Makassar Strait (black) and heat content anomaly in ETIO box (blue) are shown with ETIO box time series lagged 30 months behind the Makassar time series. Values indicating increased Makassar HFa to the south are positive. The correlation coefficient

is 0.83. Both datasets show increases between 2006 and 2008 (using black axes) followed by a negative trend continuing through 2013.

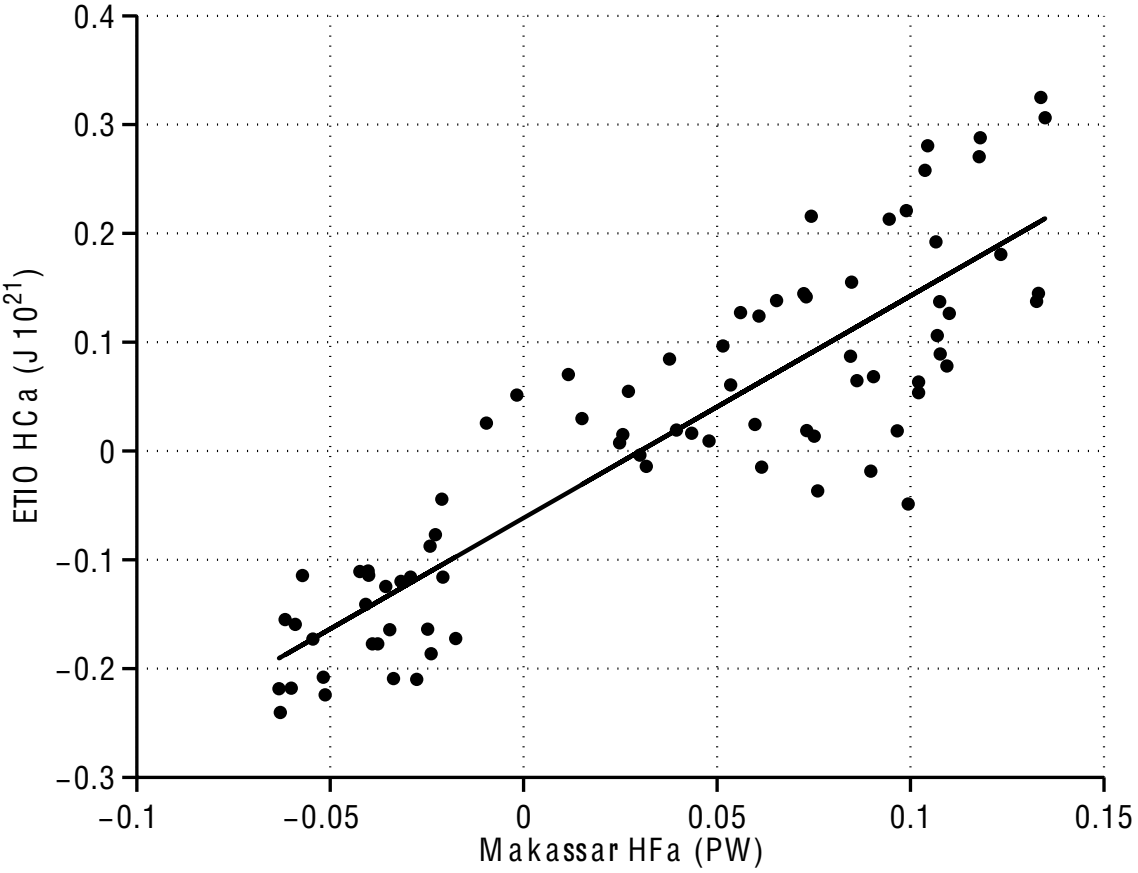


**Figure 2.8** Heat flux anomaly in Makassar Strait plotted against 30 month lagged heat content anomaly in the ETIO box. The $R^2$ value is 0.69. Positive Makassar HFa values indicate increasing Makassar HFa southward.

Although this lag may be somewhat variable due to recirculation by eddies and uncertain residence time in the Banda Sea, it is notable that the 30 month lag is consistent with a model based study by Song et al. (2004), which suggests less than four years for Makassar waters to reach the outflow region, which includes the ETIO box. This indicates the importance of

Makassar Strait throughflow in defining the water mass characteristics of ITF outflow waters. Although not all entry and exit passages of the ITF are consistently actively monitored, ITF effects on the Indian Ocean can still be identified using Makassar Strait data. The Makassar Strait contains about 77% of total ITF waters (Gordon et al. 2010). Both model (van Sebille et al., 2014) and observation based (Ffield and Gordon, 1992; Ilahude and Gordon, 1996) studies show the majority of water traveling through Makassar Strait is of North Pacific origin. van Sebille et al. (2014) shows that the majority of water traveling through the exit passages of Lombok, Timor, and Ombai are derived from the Makassar Strait, and that ITF waters crossing 110° E retain a distinct core of North Pacific water between 15 °C and 25 °C. Although there is mixing of South and North Pacific waters within the Indonesian Seas, the South Pacific contribution is smaller (Ffield and Gordon, 1992) and more concentrated in the lower water column (Huatala et al., 1996; Ilahude and Gordon, 1996).

When ETIO box HCa is compared with the Indian Ocean Dipole (IOD) Mode Index there is a significant correlation of -0.37 (higher HCa during a negative IOD) indicating that the IOD explains about 14% of ETIO HCa variance. Although the IOD may influence the inter-ocean pressure gradient that drives the ITF (Yuan et al. 2011), its importance to interannual trends in ETIO HCa is minimal when compared to the advective signal from Makassar Strait.

A large discrepancy between the Makassar HFa and ETIO HCa occurs during 2011 through 2013 (Figure 2.7, blue axes). This could have many causes including changes in residence time of water within the Banda Sea and alternate trajectories for ITF waters in the ETIO. Chapter 3, which follows, suggests the latter, with the potential for a southern pathway for ITF waters within the ETIO. It is expected that further from this immediate outflow region the advective signal may not be as well defined. But results from Lee et al. (2015) in which a

model showed increasing heat flux through Makassar Strait followed by increased heat content (0-700 m) in the Indian Ocean provide reason to believe that Makassar heat flux variability may significantly affect Indian Ocean heat content at greater spatial scales, especially when longer term (multi-year) trends are considered. Sen Gupta et al. (2016) shows a multi-model mean of 3.4 Sv reduction in ITF transport under the RCP8.5 climate change scenario. This could lead to a reduction of heat flux through the Makassar Strait, a reduction of heat content in the ETIO and, if persistent over multiple years, a reduction of upper water column heat content in the Indian Ocean.

## 2.4 Summary

Heat flux anomaly in the Makassar Strait was determined using velocity profiles from direct observations 2004-2011, 2013-2017 and an estimated variable temperature profile based on observed temperature during positive, negative, and neutral ENSO phases. The 2011-2013 gap was filled by calculating a ratio of heat flux anomaly to volume transport anomaly and applying this to the reconstructed 0-300 m Makassar transport anomaly from Li et al. (2018). Variability in the Makassar Strait heat flux is linked to changes in the velocity and temperature profiles as well as the vertically integrated volume transport within the Labani Channel. ETIO box heat content anomaly was determined using Argo gridded datasets from 2005-2017. Both time series display seasonal and interannual variability. After smoothing with a 13-month running mean they correlate well (R=0.83) with rapid increases in Makassar heat flux anomaly 2006-2008 and a slow decrease 2009-2015 manifest 30 months later in ETIO box heat content anomaly. This indicates that variability within the Makassar Strait plays an important role in determining the heat content in the ETIO with potential for that influence to spread across the

Indian Ocean, perhaps reaching into the Agulhas leakage region south of Africa, as suggested in model runs (Durgadoo et al., 2017).

## 2.5 Acknowledgements

The authors would like to acknowledge the thoughtful advice of three anonymous reviewers. The Makassar MITF time series is supported by award number UCAR Z15-17551 from the NOAA Division of Climate Observations, US Department of Commerce. The statements, findings, conclusions, and recommendations are those of the authors and do not necessarily reflect the views of NOAA or the Department of Commerce. This work was supported by NASA Headquarters under the NASA Earth and Space Science Fellowship Program, grant 80NSSC17K0438 Response of the Indian Ocean to Indonesian Throughflow Variability. Lamont-Doherty Earth Observatory contribution number 8249.

# Chapter 3: Indonesian Throughflow Partitioning Between Leeuwin and South Equatorial Currents

**Abstract**

The Indonesian throughflow (ITF) injects Pacific Ocean waters into the Indian Ocean. Here we examine the partitioning of ITF waters between its two pathways within the eastern Indian Ocean. The main ITF pathway is within the thermocline of the South Equatorial Current (SEC) forming a plume of low salinity ITF water spreading westward across the Indian Ocean near 11°S. ITF waters are also injected into the southward flowing Leeuwin Current (LC) along the western coast of Australia. We use gridded Argo data (2005-2018) as well as GODAS reanalysis (1980-2019) to investigate the variability in the partitioning between the SEC and the LC pathways. Argo derived heat content anomaly (HCa) is examined within three boxes in the eastern Indian Ocean, one immediately adjacent to the ITF outflow passages from the Indonesian Seas (ITF box), one in the far eastern branch of the SEC (SEC box), and the third in the LC (LC box). Although interannual HCa variability in the SEC and ITF boxes is well correlated, a large increase in HCa within the ITF box does not appear in the SEC box in 2011, but is evident in the LC box. The 2011 change in the SEC/LC partitioning is further investigated using GODAS reanalysis data by examining the strength of the SEC and LC during a 2009 HCa increase within the ITF box, and the subsequent increase in 2011. During 2009 a strong SEC and weakened LC spread the increased ITF HCa into the central Indian; whereas a weak SEC and strengthened LC during 2011 transmit the HCa signal to the south, along the western coast of Australia. Near surface winds and mean sea level pressure from NCEP/NCAR reanalysis reveal that Ningaloo Niño atmospheric conditions led to the shift in circulation during 2011. Comparison to a weaker Ningaloo Niño in 2000 reveals a similar circulation pattern. LC and SEC exports show a high

negative correlation at interannual timescales, indicating that a reduction of outflow from one pathway is partially compensated by an increase from the other.

## 3.1 Introduction

The Indonesian Throughflow (ITF) is a significant conduit for the transfer of Pacific Ocean water into the Indian Ocean, impacting the distribution of ocean heat within these two basins. The 'global warming hiatus' of the 2000s was in part caused by a redistribution of heat from the tropical Pacific to the upper water column within the Indian Ocean (Nieves et al. 2015). Lee et al. (2015) showed that excess heat uptake by the Pacific was transferred via increased ITF to the Indian Ocean, creating a subsequent upper ocean heat content increase. Zhang et al. (2018) likewise concludes that increasing advection from the ITF is the greatest contributor to an increase in upper ocean heat content in the southern Indian Ocean during the last two decades. This increased advection of heat has had an effect on the Mascarene High region, weakening the atmospheric meridional pressure gradient over the Indian Ocean basin and influencing cross-equatorial winds (Vidya et al., 2020). Makassar Strait, which represents about 80% of the total ITF (Gordon et al., 2010), displays heat flux variability which is reflected in heat content variability in the eastern tropical Indian Ocean (Gruenburg & Gordon, 2018).

While it is clear that the ITF plays an important role in inter-basin heat exchange between the Indian and Pacific, the specific pathways of ITF spreading in the Indian Ocean can provide insight to where within the Indian the ITF water is distributed, with implications for local air-sea interaction and regional ecosystems. There are two identified avenues for the ITF to take, the South Equatorial Current (SEC) to the west between 10°S and 15°S, and the Leeuwin Current (LC) flowing southward along the western coast of Australia (Figure 3.1).

The westward flowing SEC stretches from the Indo-Australian Basin to the eastern African margin (Wyrtki, 1961; Schott and McCreary, 2001), carrying ITF waters to the western part of the basin where the SEC splits and either joins the Agulhas via the Mozambique or East Madagascar Currents or flows to the north via the East African Coastal Current (Song et al, 2004). The SEC is driven by regional wind patterns and is also influenced by the ITF (Godfrey and Golding, 1981). To the south, the relatively shallow (<200m) LC is driven by the pressure gradient created by higher sea level off northwestern Australia, a result of the ITF (e.g. Thompson, 1984; Godfrey & Ridgway, 1985). The LC is strongest during austral winter when the prevailing northward winds weaken (e.g. Smith et al. 1991). Gordon et al. (1997) shows the importance of the SEC pathway, identifying waters of up to 60% ITF origin transported by the SEC into the western Indian Ocean. Durgadoo et al. (2017) shows that 6.1 Sv of Agulhas Leakage has an ITF source, connected to the western Indian primarily via the SEC. van Sebille et al. (2014) uses a model with Lagrangian particles to show that most of the ITF enters the SEC, though there is a smaller core of these particles that are injected into the LC. Although these studies have shown that the ITF does flow through both the SEC and the LC, variability between these two routes is still poorly understood.

Understanding how the ITF partitions between these two pathways is important for determining how and where the heat and freshwater from the Pacific spreads across the Indian Ocean. As discussed above, increased westward SEC propagation, or westward propagation of eddies and Rossby waves from the Leeuwin region, can bring ITF waters into the southern Indian Ocean affecting upper ocean heat content and cross-equatorial monsoonal winds. Increases in the SEC pathway can potentially impact the Agulhas Current and Leakage, although these effects would likely be seen at least a decade later. It is also possible that ITF waters in the

Leeuwin only remain in the Indian Ocean briefly before making their way back toward the Pacific within the South Australia Current. This study uses Argo observations from 2005-2018 to track changes in upper ocean heat content, and GODAS reanalysis data to examine current velocity within the SEC and LC outflows of ITF water, with the aim of understanding the temporal ratio changes between the two pathways.

### 3.2 Methods and Objectives

Depth integrated heat content of the water column was calculated in each of three boxes (Figure 3.1) within the eastern tropical Indian Ocean (ETIO). The three boxes are the ITF box (10.5°S to 15.5°S and 115.5°E to 120.5°E), the SEC box (10.5°S to 15.5°S and 100.5°E to 105.5°E) and the LC box (21.5°S to 28.5°S and 110.5°E to 115.5°E). The SEC and ITF boxes are located within the ITF low salinity buoyant plume designated by Anderson and Stigebrandt (2005) (AS box; 10°S to15°S at 100°E to 120°E). The ITF box is positioned at the far eastern end of the AS box and encompasses the waters leaving the Indonesian Seas through the Timor and Ombai Passages, together making up roughly 80% of the total outflow (based on INSTANT program values; Gordon et al. 2010). The SEC box is in the far western portion of the AS box and encompasses the ITF outflow that will enter the Indian Ocean within the South Equatorial Current. The half degree offset between the AS box bounds and those of the SEC and ITF boxes relate to the 1°x1° spatial resolution of the gridded Argo dataset which provides variables on the half degree. The LC box falls south of the AS box along the west Australian coast.

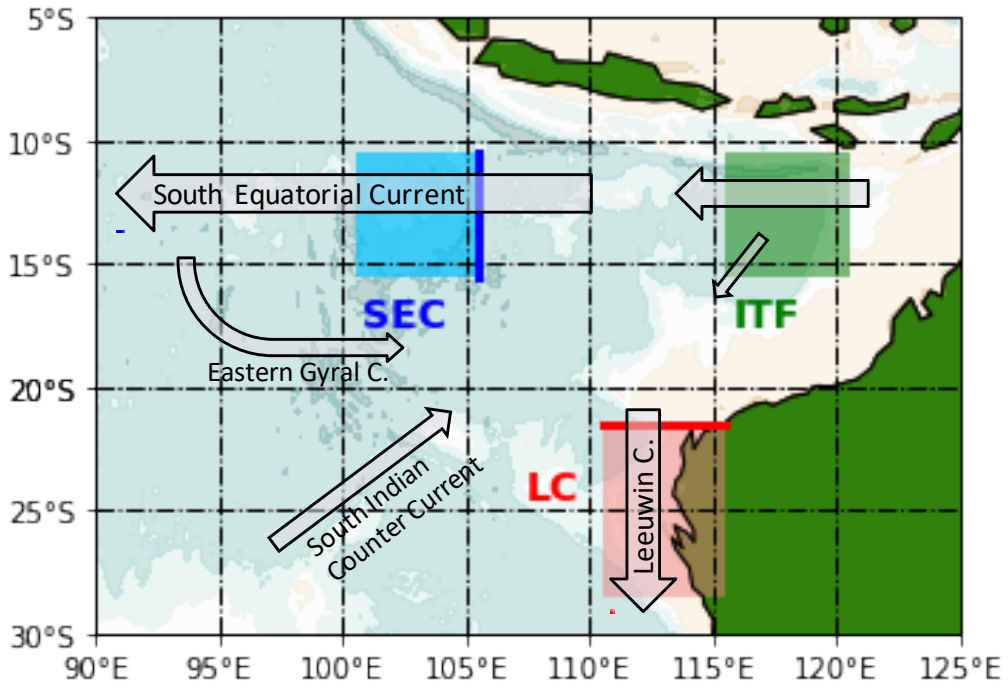


**Figure 3.1** The Indonesian throughflow outflow area within the eastern tropical Indian Ocean. Currents are shown in black arrows. The 3 boxes where upper ocean heat content were calculated are the ITF (green), SEC (blue), and LC (red). Velocity associated with the South Equatorial Current, and the Leeuwin Current were examined across the thick blue and red lines respectively.

The upper ocean heat content (HC; above 25.5σ) in each box was calculated using the following equation:

$$Q_{25.5\sigma} = \int_{25.5\sigma}^{surf} \theta \rho c_p dz \qquad [1]$$

The parameters $\theta$ and $\rho$ were acquired from gridded Argo datasets (retrieved from http://apdrc.soest.hawaii.edu/projects/argo/.). The Argo datasets were at 1°x1° degree spatial resolution with monthly temporal resolution from 2005 through 2018. HC was calculated above an isopycnal instead of a fixed depth to account for changes in heat content induced by

thermocline heaving. We compare heat content anomaly calculated above a fixed depth of 300m to that above 25.5σ in Figure 3.2. Although the magnitude of the HCa is different is either case primarily due to difference in volume, the heat content variability is quite similar in both cases across all 3 boxes. We use HCa above the 25.5σ surface in all further analysis.

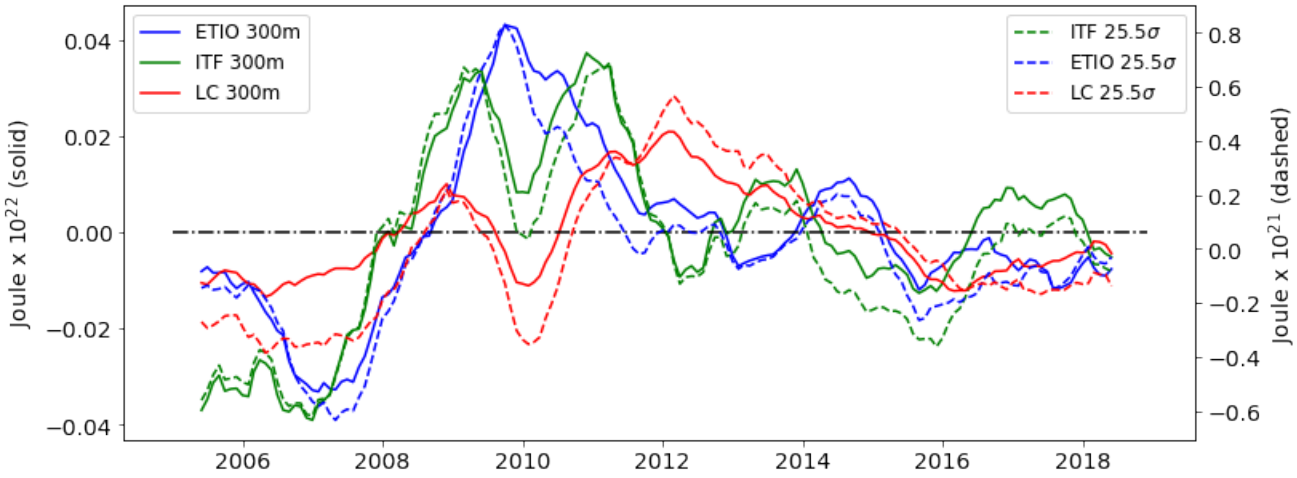


**Figure 3.2** Heat content anomaly above 300m within the ETIO (blue), ITF (green) and LC (red) boxes is shown in solid lines. Dashed lines show heat content anomaly above 25.5σ.

As the ITF tends to spread within the Indian Ocean thermocline (Gordon 1986; Gordon et al, 1997) we chose to investigate HCa above the 25.5σ surface as it is within the climatological mid-thermocline, near 200m, for all three boxes (Figure 3.3). For each grid point within the three boxes at monthly time steps, the potential temperature ($\theta$) and potential density ($\sigma$) variables were linearly interpolated from standard depths (fine resolution close to the surface with increased spacing at depth) to 10 m intervals from the surface to the 25.5σ surface. Heat content per $m^2$ was then calculated using equation [1] with $c_p$ =4000 $Jkg^{-1}K^{-1}$. HC values for each grid

point within the box were then summed. Heat content per $m^2$ is used instead of total heat content over the area of the box due to the different sizes of the boxes. As a result of shallow topography not all grid points within the Leeuwin and ITF boxes contained data. To verify that Argo floats were present in the boxes the number of profiles per year was calculated and is plotted in Figure 3.4. Heat content anomaly (HCa) was calculated by removing the time averaged HC values at each grid point from each monthly time step. A12-month running mean was applied to all time series to smooth out the seasonal cycle.

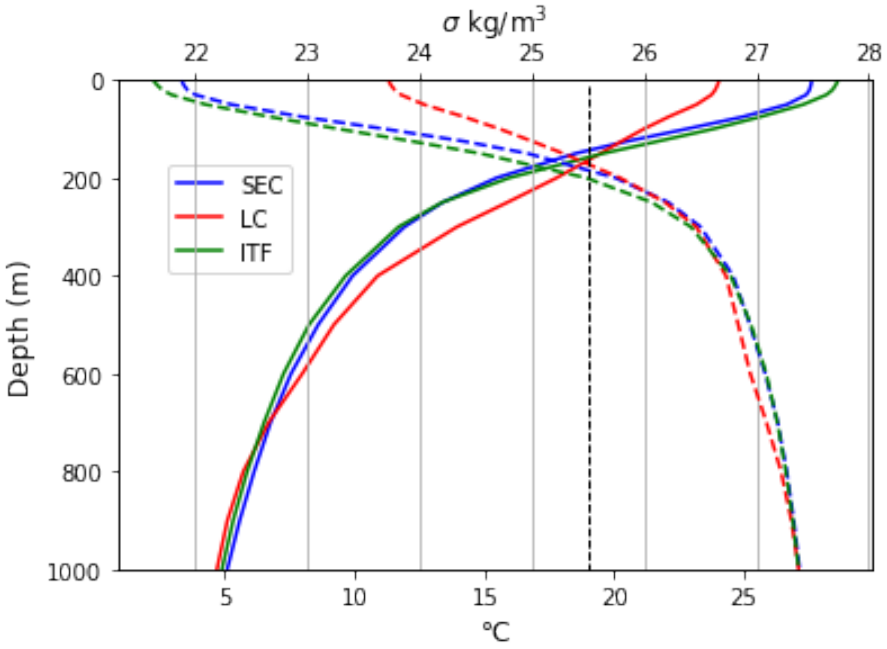


**Figure 3.3** Mean temperature (bottom x-axis, solid lines) and density (top x-axis, dashed lines) for the ITF (green), SEC (blue) and LC (red) boxes.

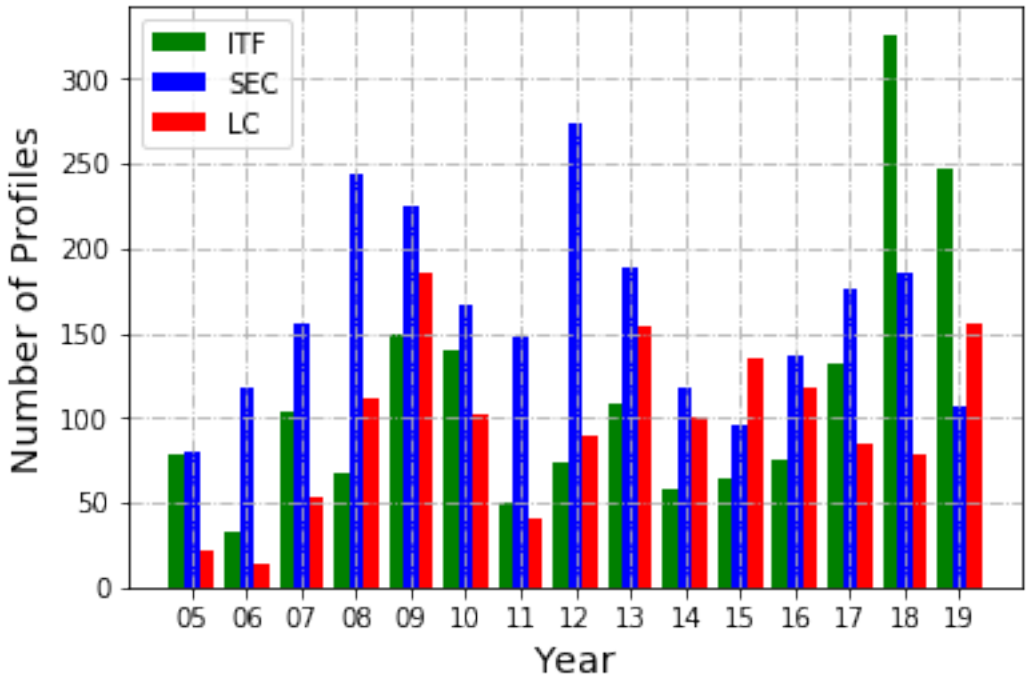


**Figure 3.4** The number of Argo profiles within each box by year. ITF box shown in green, SEC in blue, and LC in red.

The HCa within the ITF box is compared with those in the other two boxes. First the 12-month running mean of the SEC box heat content anomaly is cross-correlated at monthly lags (one month time step for 2 years) with the ITF box. Correlations were considered significant with p values less than 0.05.

Next we examined the changes in the zonal velocity (SEC) and meridional velocity (LC) within the upper water column. The SEC section (blue line in Figure 3.1) is the most westward boundary of the box (105°E from 15°S to 10°S). The Leeuwin section (red line in Figure 3.1) cuts across the top of the LC box, at 21°S from 110°E to 115°E . The southward velocities across the LC section and westward velocities across the SEC section were investigated using meridional and zonal velocities 0 – 400 m from GODAS reanalysis (Behringer & Xue, 2004). GODAS is a gridded global dataset at a spatial resolution of 1/3° latitude by 1° longitude of

monthly mean variables. U and v components of current velocity were retrieved at 28 depth levels (5, 15, 25, 35, 45, 55, 65, 75, 85, 95, 105, 115, 125, 135, 145, 155, 165, 175, 185, 195, 205, 215, 225, 238, 262, 303, 366, and 459 meters) from 1980 through 2019. GODAS data was retrieved from https://www.esrl.noaa.gov/psd/data/gridded/data.godas.html. When examining the anomaly, we subtracted the climatological monthly mean values. These climatological values were created by averaging only over 2005 through 2018 to be consistent with the Argo data.

Next we aimed to quantify the transport out of the Indo-Australian basin by the SEC and LC pathways. Volume transport across the SEC section (blue line in Figure 3.1) was calculated at the eastern boundary of SEC box (100°E from 15°S to 10°S). Transport across the Leeuwin (LC) section cuts across the top boundary of the LC box (21.5°S from 110°E to 115°E) the Leeuwin heat content box. The southward transport along the LC section and westward transport across the SEC section were investigated using meridional and zonal velocities from 25.5σ to the surface using the GODAS reanalysis described above. A 12-month running mean was applied to all resulting time series to smooth out the seasonal cycle.

To further understand the relationship between the two outflow pathways, a time varying cross correlation between the two was preformed, both of monthly means and of the 12-month running mean time series. To investigate which external forces played a role in transport variability the two time series were compared to NINO3.4, DMI, u, and v components of near surface wind speed, and sea surface height anomaly. The NINO3.4 and DMI time series were retrieved from https://www.cpc.ncep.noaa.gov/data/indices/ and https://www.esrl.noaa.gov/psd/gcos_wgsp/Timeseries/DMI/ respectively. NCAR/NCEP Reanalysis 1 (Kalnay et al., 1996) u and v component of wind speed at 1000 hPa wind speeds

were retrieved from https://www.esrl.noaa.gov/psd/data/gridded/data.ncep.reanalysis.pressure.html. This dataset provided wind speed at 2.5° x 2.5° spatial resolution monthly from January 1949 through December 2018. To be consistent with the ARGO data, only wind speeds from 2005 onward were used. Sea surface height anomaly from the geoid (SSH) was included in the GODAS reanalysis dataset. The SEC and LC transport time series were compared to the winds in a box bounded by 50°S to 22.5°N and 50°E to 150°E, encompassing the majority of the Indian Ocean and a portion of the Pacific Ocean containing the west Pacific warm pool. At each grid point within this domain the 12-month running mean u, and v wind speeds were cross correlated with the SEC and LC 12-month running mean at monthly lags for 2 years. The same procedure was performed using SSHg within the box bounded by 41.17°S to 1.17°S and 40.5°E to 129.5°E encompassing the southern Indian Ocean.

## 3.3 Results

### 3.3.1 Heat Content

Timeseries of heat content anomaly per square meter (HCa) is plotted in Figures 3.5a-c. The mean HCa in the ITF box is $8.1 \times 10^{11} \pm 2.4 \times 10^{10}$ J/m$^2$, $8.6 \times 10^{11} \pm 2.0 \times 10^{10}$ J/m$^2$ in the SEC box, and $5.1 \times 10^{11} \pm 1.2 \times 10^{10}$ J/m$^2$ in the LC box. A strong seasonal cycle is present in both the SEC and LC boxes. The SEC experiences maximum HCa/m$^2$ in September/October and minimum HCa/m$^2$ in March/April. Maximum HCa/m$^2$ in the LC box occurs in April/May/June with a minimum in September/October/November. The SEC box is well correlated with the ITF box ($r=0.81$) when the SEC box lags the ITF box by 5 months. The first positive HCa peak in the ITF time series during 2009 is present 5 months later in the SEC box, however the second ITF HCa peak in 2011 does not appear in the SEC box, but appears in the LC box (Figure 3.5d-h).

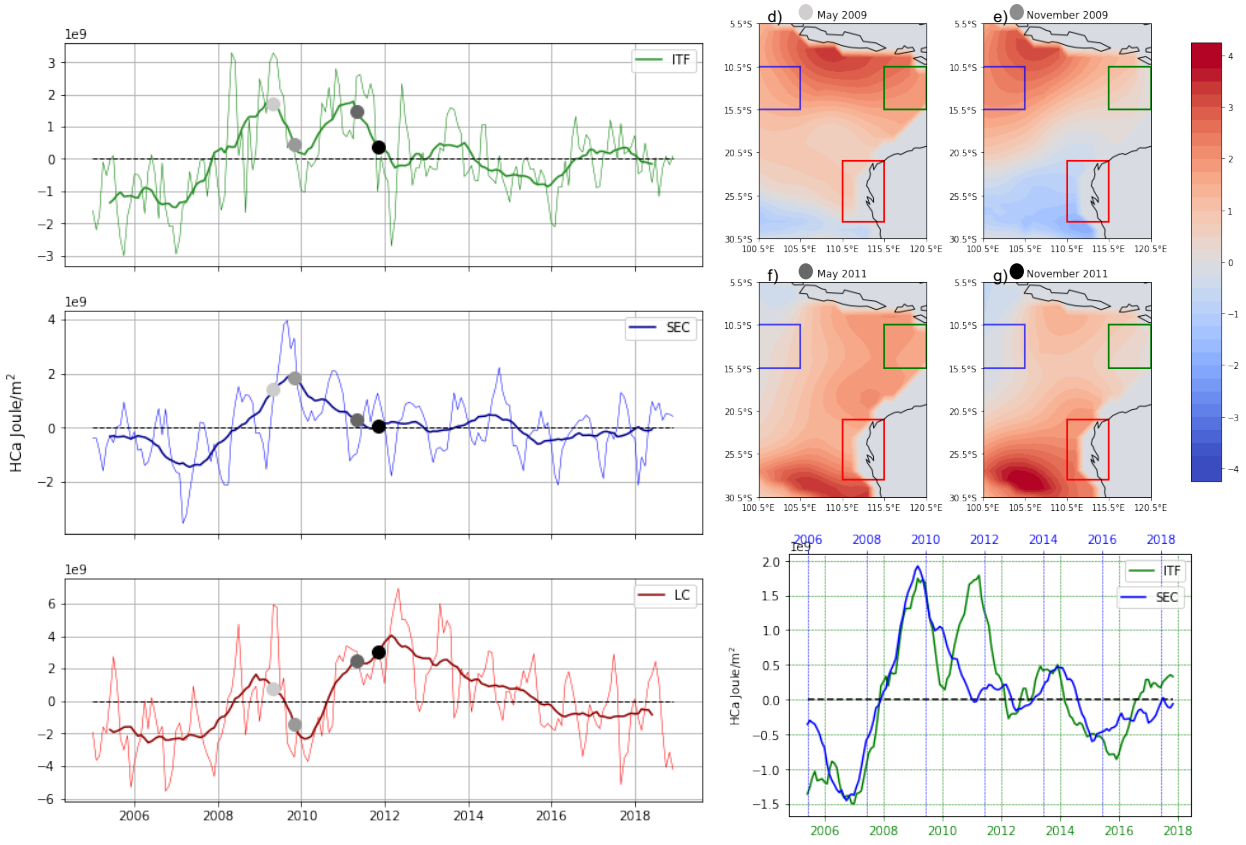


**Figure 3.5** ***Left*** Heat content anomaly per $m^2$ above the 25.5σ surface in each of the 3 boxes. a) ITF box thin line showing monthly means and thick line with a 12-month running mean. b) and c) as in a) for the SEC and LC boxes respectively. Grey circles correspond to contour plots d) through g). ***Top Right*** d) through g) show heat content anomaly per $m^2$ above the 25.5σ surface at each 1º x 1º gridpoint in the Argo dataset. Heat content anomaly time series at each gridpoint are smoothed with a 12-month running mean. Warm colors indicate positive heat content anomaly and cool colors indicate negative heat content anomaly. d) and e) show May and November of 2009. A positive heat content anomaly is seen propagating from the ITF box westward toward the SEC box. f) and g) show May and November 2011. During this time period heat content anomaly is advected southward from the ITF box into the LC region. ***Bottom Right*** Heat content anomaly per $m^2$ above the 25.5σ surface in ITF (green) and SEC

(blue) boxes plotted with a 12-month running mean. The SEC box (top blue x-axis) is shown lagged 5-months behind the ITF box (lower green x-axis). At this lag the two are well correlated with r=0.8. The second large positive HCa in the ITF box during 2010—2011 is not reflected later in the SEC box.

### 3.3.2 Velocity Across Sections

We next examine the velocity in the SEC and LC sections (Figure 3.1) during 2009 (first peak in ITF HCa) and 2011 (second peak). During early 2009 there was an increase in westward velocity in the SEC predominately in the upper 200 m during January, February, March (JFM) with maximum anomalies around 5 cm/s within the surface layer (Figure 3.6). Conversely, during 2011 we see a strong negative anomaly, with an anomalous eastward flow with maximum values of -3.5 cm/s, within the upper 200 m of the SEC during JFM. In the LC region 2009 is marked by slightly weaker southward flow in the upper water column than climatological values (Figure 3.7). During 2011 an increase in southward flow is present.

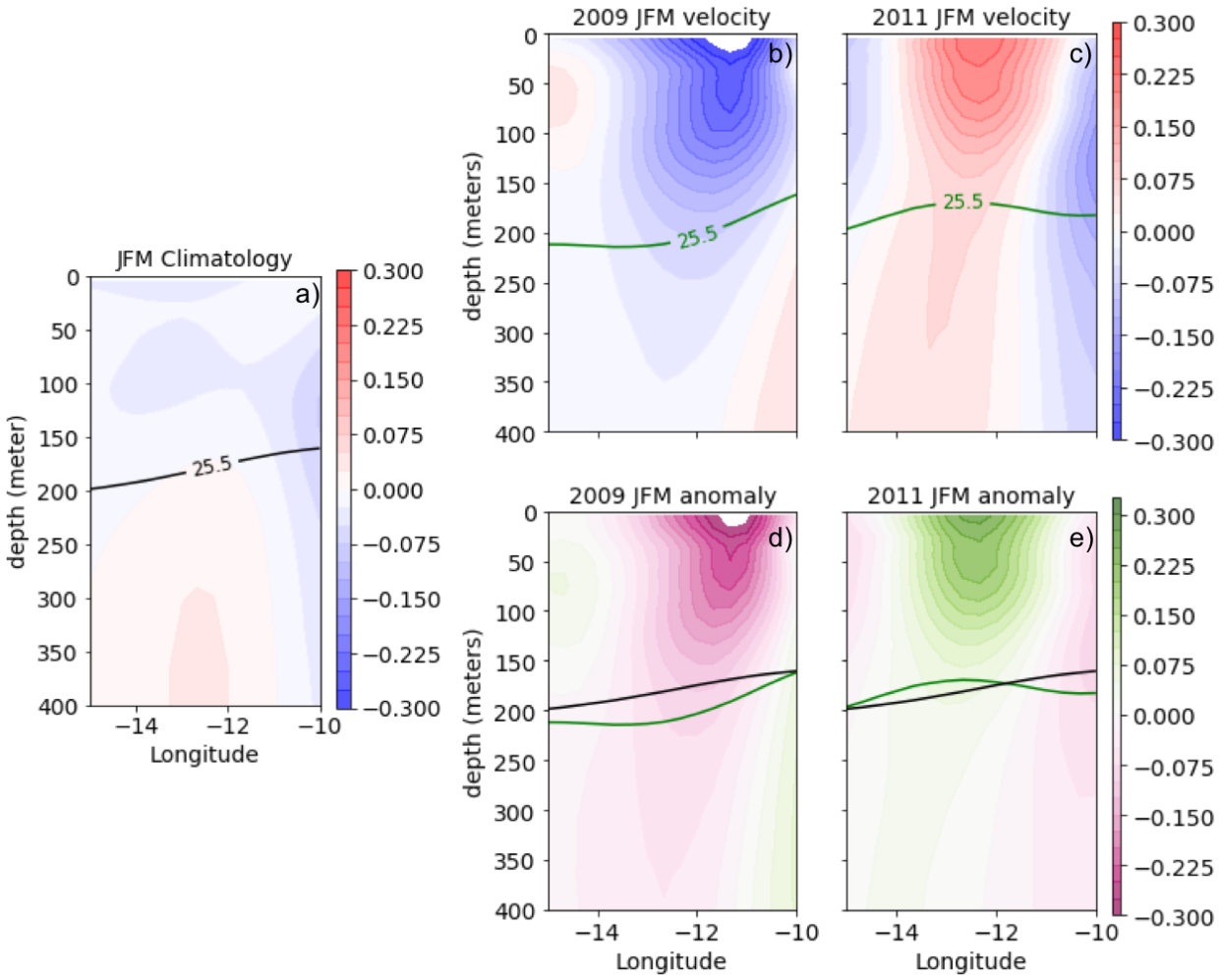


**Figure 3.6** Zonal velocity is shown across 105ºE, the easternmost boundary of the SEC box. a) Climatological velocity for averaged January, February, March (JFM) with blue as westward and red as eastward velocities. The 25.5**σ** isopycnal is shown as a black line. b) and c) show JFM averaged velocity for 2009 and 2011 respectively with red and blue shading as in a). The 25.5**σ** isopycnal is shown in green. d) and e) show JFM anomaly from the climatology for 2009 and 2011 respectively. Purples indicate anomalous westward velocity and greens anomalous eastward velocity. Climatological and JFM averaged 25.5**σ** isopycnals are shown in black and green respectively. A strong westward flow is present in 2009, whereas 2011 shows an eastward flow.

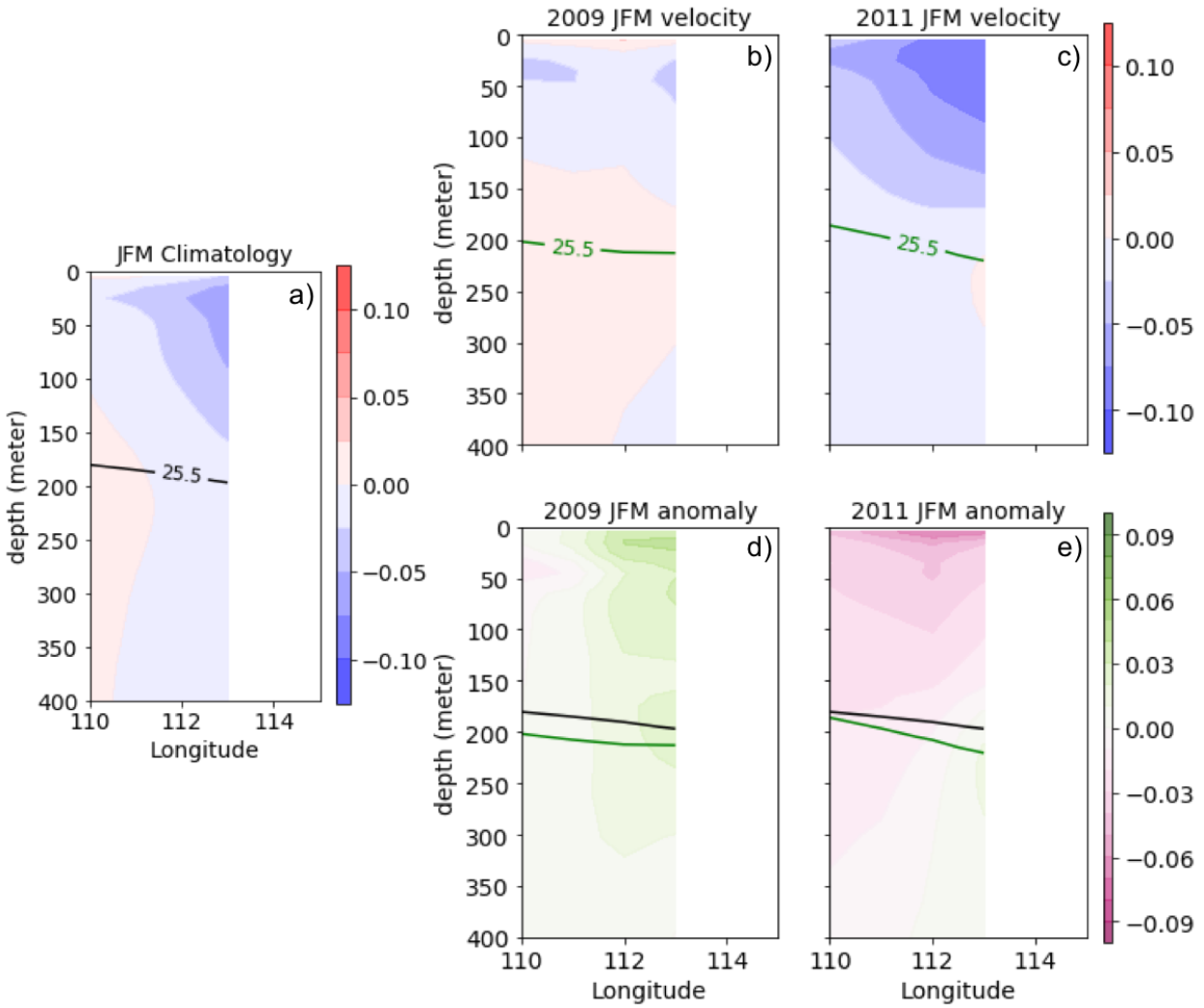


**Figure 3.7** Meridional velocity across 21.5ºS, the top of the LC box. a) Climatological velocity for averaged January, February, March (JFM) with blue southward and red as northward velocities. The 25.5**σ** isopycnal is shown as a black line. b) and c) show JFM averaged velocity for 2009 and 2011 respectively with red and blue shading as in a). The 25.5**σ** isopycnal is shown in green. d) and e) show JFM anomaly from the climatology for 2009 and 2011 respectively. Purples indicate a strengthened southward velocity and greens weakened southward velocity. Climatological and JFM averaged 25.5**σ** isopycnals are shown in black and green respectively. A weakening of southward flow is seen in 2009, whereas 2011 shows a strong increase in southward flow.

### 3.3.3 Near Surface Winds and Mean Sea Level Pressure

The u and v components of wind and the mean sea level pressure reveal strong anomalies in 2011 (Figures 3.8 and 3.9). In JFM of that year there were strong positive (eastward) zonal wind anomalies along 10°S from 80°E to 110°E. Meridional winds show negative anomalies (weaker northward) over the western coast of Australia as well as in the Indo-Australian Basin during JFM. Mean sea level pressure (MSLP) reveals a region of low pressure located in northwest Australia, and MSLP anomaly further indicates that anomalously low MSLP was present off the west Australian Coast. These pressure anomalies are consistent with the cyclonic circulation that produced the zonal and meridional wind anomalies seen in 2011. When 2009 is examined we see no consistent and well defined positive or negative anomalies in zonal winds. There is a small positive meridional wind (more northward) anomaly over our LC box for the first three months of 2009. MSLP reveals only a small positive pressure anomaly along the west Australian Coast.

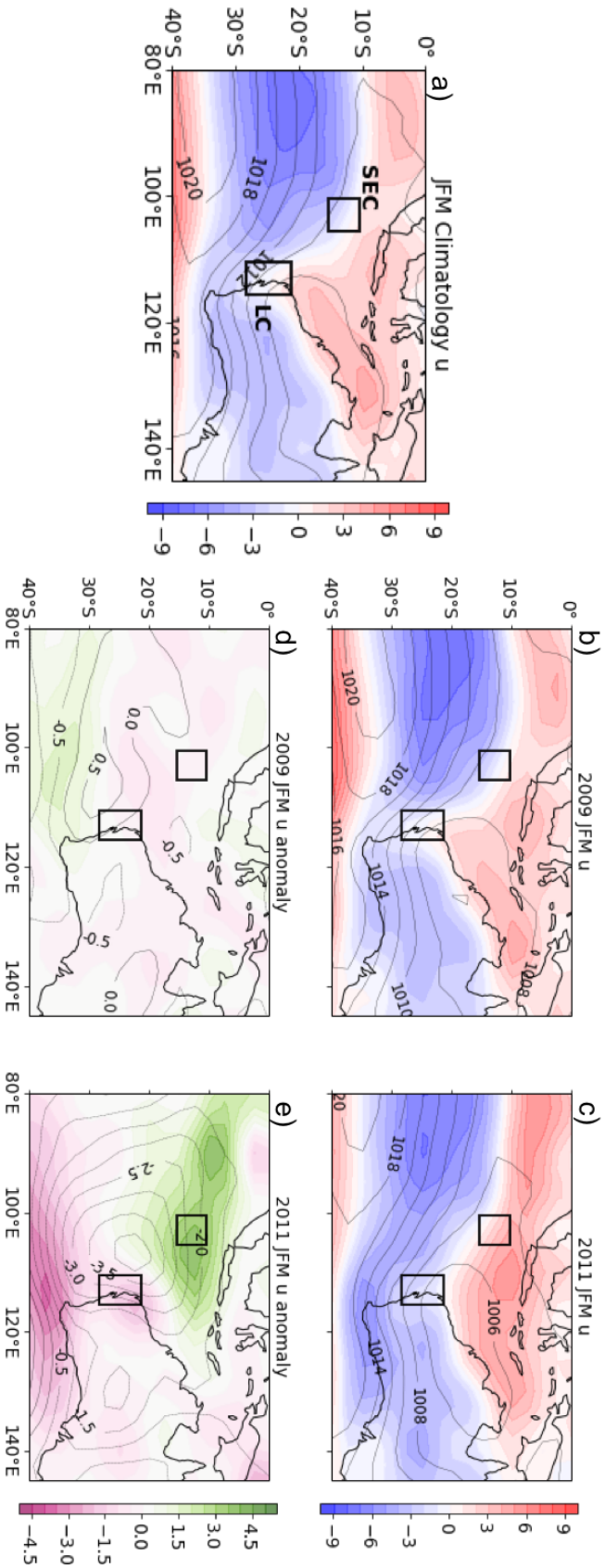
a)
JFM Climatology u
SEC
LC
b)
2009 JFM u
c)
2011 JFM u
d)
2009 JFM u anomaly
e)
2011 JFM u anomaly

**Figure 3.8** Zonal wind speed at 1000HPa is shown by colored shading and MSLP as black contour lines. a) Climatological average of JFM with reds indicating westerly winds and blues easterly winds. b) and c) show zonal winds and MSLP during JFM of 2009 and 2011 respectively with colored shading as in a). d) and e) show JFM zonal wind anomaly from the climatology in colored shading with greens as positive anomalies (stronger eastward/weaker westward) and purples as negative anomalies (stronger westward/weaker eastward). MSLP anomalies are shown as black contours. During 2011 an anomalous low pressure center is present off the west Australian coast, with positive zonal wind anomalies present along its northern flank at around along 10ºS.

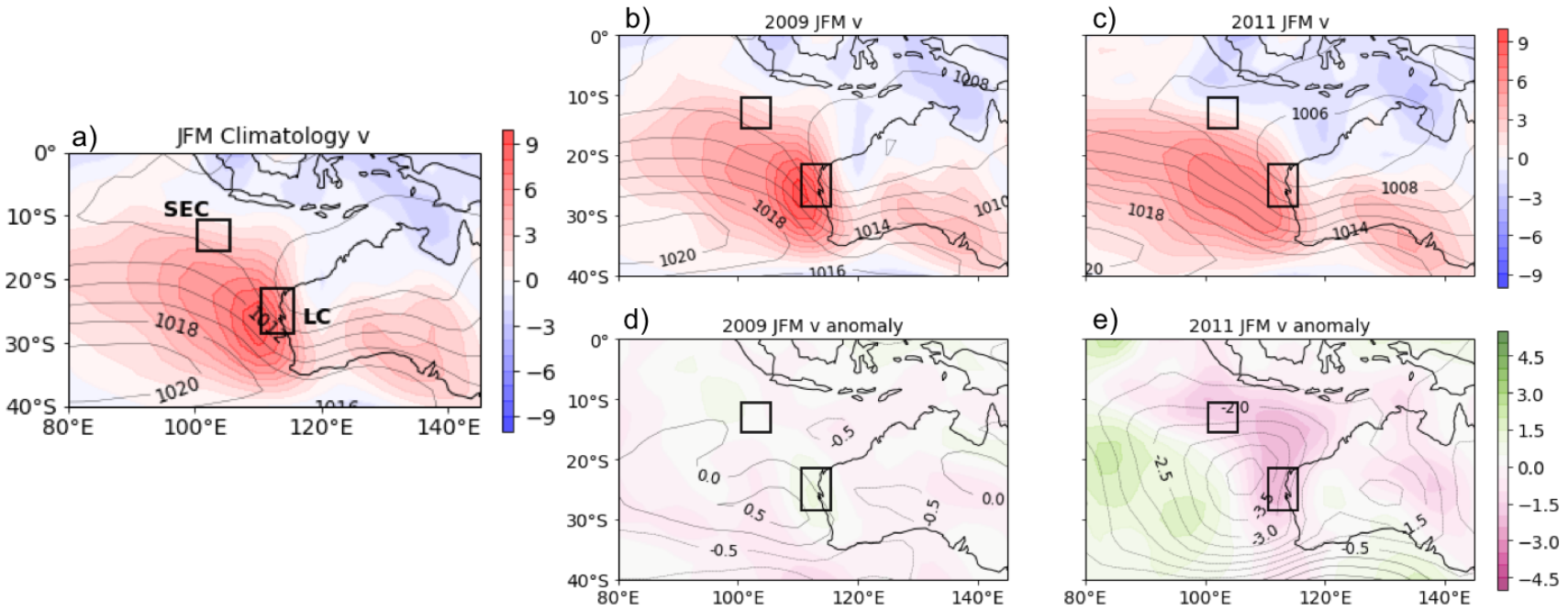
a)
JFM Climatology v
SEC
LC
b)
2009 JFM v
c)
2011 JFM v
d)
2009 JFM v anomaly
e)
2011 JFM v anomaly
0°
10°S
20°S
30°S
40°S
80°E
100°E
120°E
140°E

**Figure 3.9** Meridional wind speed at 1000HPa is shown by colored shading and MSLP as black contour lines. a) Climatological average of JFM with reds indicating southerly winds and blues northerly winds. b) and c) show meridional winds and MSLP during JFM of 2009 and 2011 respectively with colored shading as in a). d) and e) show JFM meridional wind anomaly from the climatology in colored shading with greens as positive anomalies (stronger northward/weaker southward) and purples as negative anomalies (stronger southward/weaker northward). MSLP anomalies are shown as black contours. The low pressure center off the west Australian coast during 2011 is associated with anomalous cyclonic atmospheric circulation and a weakening of southerly winds in the Leeuwin Current region. Conversely, during 2009 MSLP anomalies are weakly positive to the west of Australia and meridional wind anomalies are weakly positive over the Leeuwin Current region.

### 3.3.4 Transport Across Sections

The mean transport across the SEC section was -7.0±5.5Sv (negative transport indicates westward flow, *out* of ETIO region), and across the LC section was -1.7±1.7Sv, the error reflects one standard deviation. The large standard deviation is indicative of a robust seasonal cycle (thin lines Figure 3.10). When we compare the LC and SEC time series, we see that the monthly means are well correlated (r=-0.63). When the seasonal cycle is removed using a 12-month running mean the two time series are poorly correlated (r = -0.25; Figure 3.11). It is noted that Figure 3.11 shows three distinct clusters in time of transport data. We examine these three groups individually (A: 2006-2011, B: 2012-2016, and C: 2017-2019) and see that LC and SEC are very well correlated with r=-0.9 in each case. Although when broken into smaller groups there are fewer data points on which to perform the correlation and thus the confidence in the

relationship between the two time series is not as strong. LC is well correlated (r = 0.62) with the Niño3.4 index whereas the SEC is not well correlated with Niño3.4. The SEC is correlated with DMI (r = 0.47) when SEC lags DMI 11months; the LC is correlated with DMI (r = -0.46) when LC lags DMI 21 months.

When compared with u and v components of wind speed the SEC shows highest correlation ($|r| > 0.5$, Figure 3.12) with zonal winds over the maritime continent and with meridional winds off the western coasts of Sumatra and Java (Figure 3.12). LC shows the highest negative correlation ($r < -0.5$) with zonal winds over the south central Indian and highest positive correlation ($r > 0.5$) with zonal winds off the northwest coast of Australia and the southwest coast of Sumatra. The highest correlation between LC and meridional winds occurs off the north west coast of Australia ($r > 0.5$) and to the south of Java ($r < -0.5$).

The SEC shows a high correlation ($r < -0.7$) with SSH in the region immediately to the west of the section. The LC shows the highest correlation ($r < -0.7$) along the west and north Australian coasts (Figure 3.13).

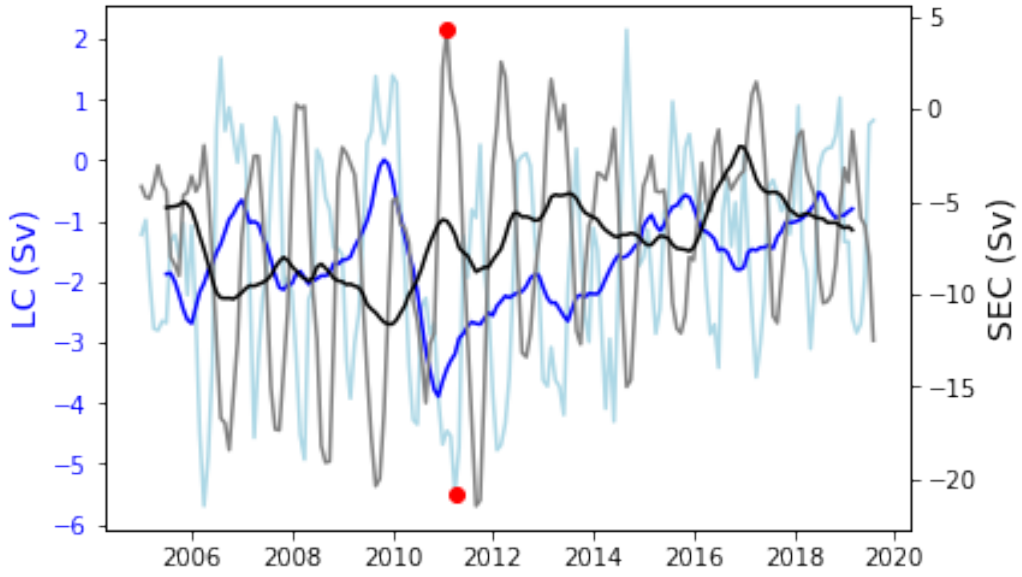


**Figure 3.10** Leeuwin Current and South Equatorial Current transports above 25.5σ surface during the ARGO observational time period. LC is show in light blue (monthly mean) and dark blue (12-month running mean) lines. SEC is shown in grey (monthly mean) and black (12-month running mean) lines. Red dots indicate the early 2011 minimum/reversal in SEC transport and maximum in LC transport.

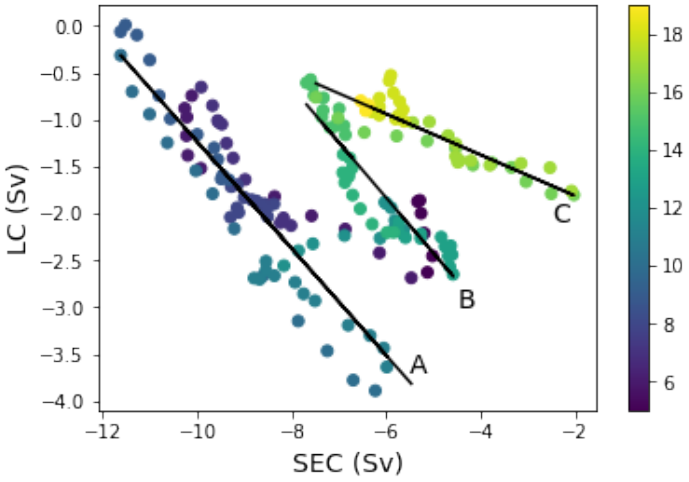


**Figure 3.11** Scatter plot depicting 12-month running mean of SEC transport on the x-axis and 12-month running mean of LC transport on the y-axis. Colors indicate the year with 2005 in

blue and 2019 in yellow. When grouped in time they are well correlated with A: 2006-2011, r=-0.9, B: 2012-2016, r=-0.9, and C: 2017-2019, r=-0.9.

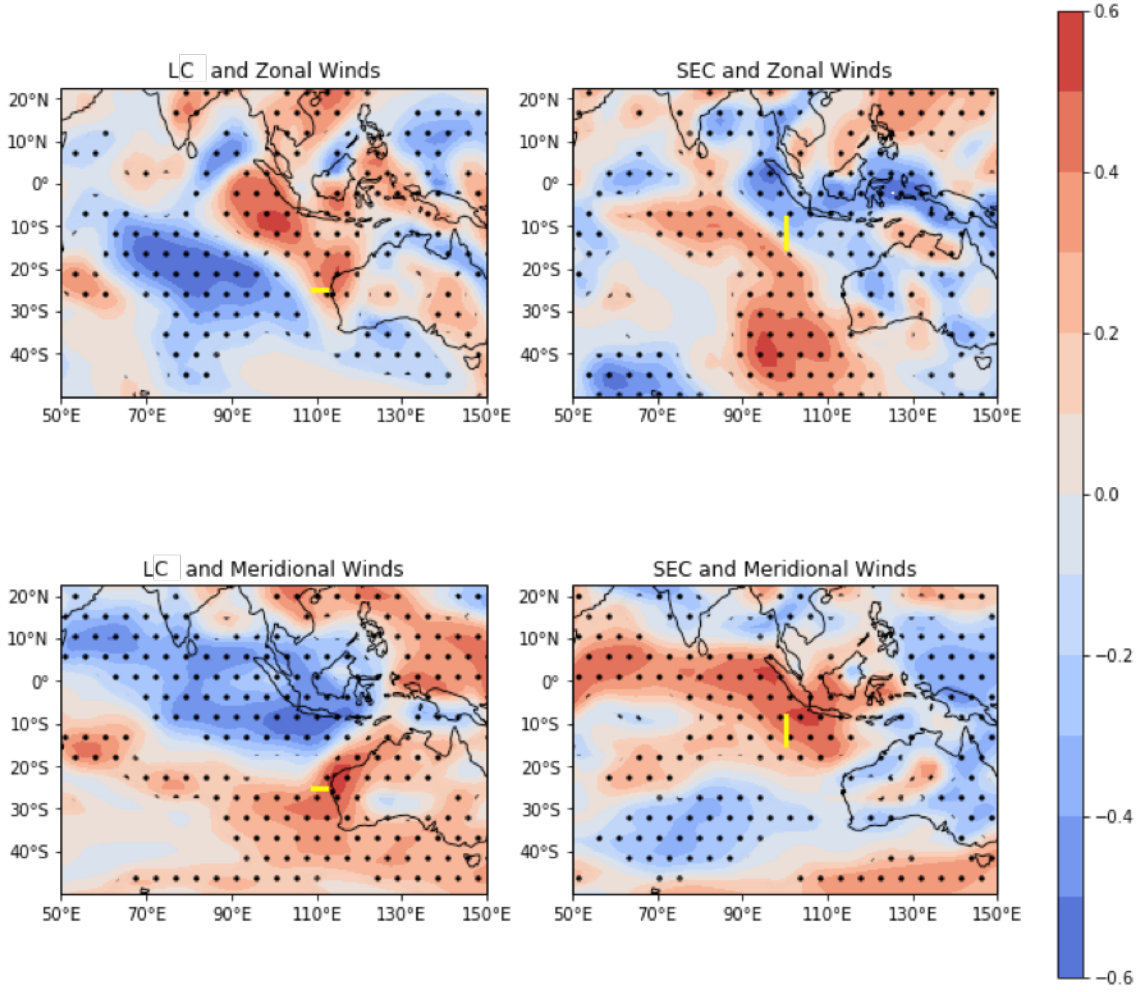


**Figure 3.12** LC section and SEC section correlation with meridional and zonal wind speed. Red colors indicate positive correlation (more positive wind speed linked with reduced transport across sections) and blue colors show negative correlation (more positive wind speed linked to increased transport across section). Stippling indicates correlation is significant with $p < 0.05$. SEC and LC sections are shown in thick yellow lines.

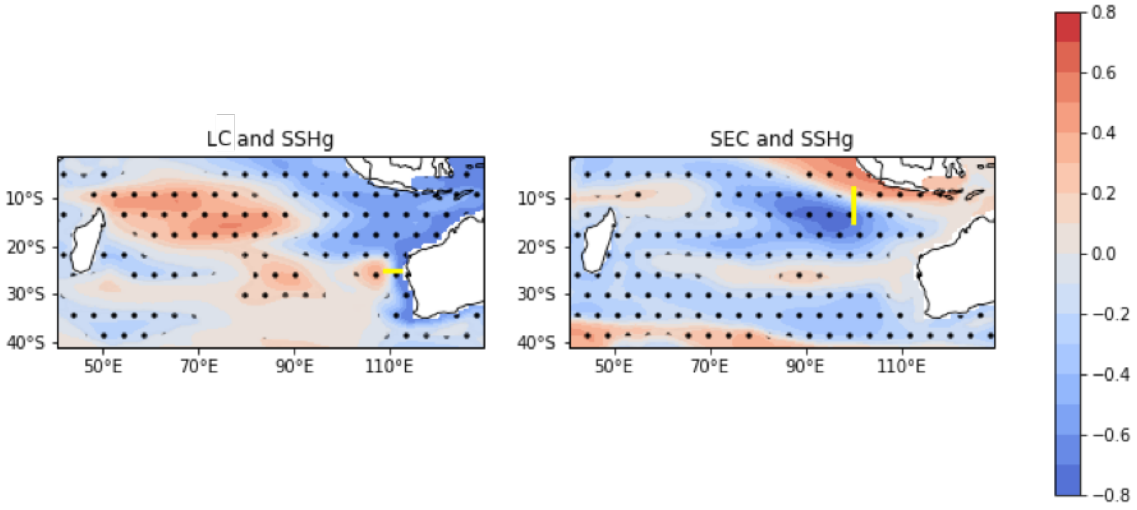


**Figure 3.13** Correlation between LC (left) and SEC (right) section transport and SSHg. Warm colors indicate positive correlation (higher sea surface height connected with reduced transport) and cool colors indicate negative correlation (higher sea surface height associated with increase in transport). Stippling for significant correlations. LC and SEC sections are shown in bold yellow line.

## 3.4 Discussion

Our results clearly indicate a change in circulation during 2011 within the eastern tropical Indian Ocean when compared with 2009. This year is of particular importance in the region as it was a very strong Ningaloo Niño. A Ningaloo Niño is defined by anomalously high SST within the region of 32°S-26°S, 112°E-115°E (Ningaloo Niño Index (NNI), Marshal et al. 2015), and during 2011 this region experienced 3°C of surface warming (Feng, et. Al., 2013). Our analysis of wind speed and MSLP is consistent with that of Feng et al. (2013) who examined this event in detail and concluded that the weakened southerly winds off the west Australian Coast had a large impact on the increasing LC flow. We find that in addition to the anomalous behavior of the LC, this time period is also characterized by the reversal of flow across the SEC section (Figure 3.6).

Our results indicate that this reversal of the SEC during 2011 was also an important factor in the warming within the LC region, and further discussion of SEC variability will follow in Chapter 4. In addition to the strengthening of the LC which would carry ITF waters to the south there was a simultaneous reduction in westward SEC transport and heat exiting the Indonesian Seas was not efficiently exported from the Indo-Australian basin to the west. Benthuysen et al. (2014) agrees with this conclusion, and finds that 2/3 of the anomalous warming in the LC region during this time period was due to advection as opposed to changes in air-sea interaction. Our results from 2009 indicate an opposing circulation to that of 2011, with a strong SEC during the early part of the year that transported heat into the central Indian, and a weakened Leeuwin. Wind anomalies during 2009 were relatively weak, and the NNI was close to zero indicating neutral conditions. Although the Argo dataset is too short to have recorded another strong Ningaloo Niño event, we use the GODAS reanalysis to examine the SEC and LC velocities and regional MSLP, as well as NCEP/NCAR reanalysis for wind speed, from another smaller Ningaloo Niño event during 2000 (Figures 3.14 through 3.17). Although the anomalies are smaller, they are similar to those of 2011, with a reversal of flow within the SEC region, an increase in LC transport, and a small low pressure anomaly off the northwestern coast of Australia driving a cyclonic circulation. Our results show the importance of the characteristic Ningaloo Niño atmospheric low and anomalous cyclonic circulation (Kataoka et al., 2013) to the upper ocean export pathways of the ITF.

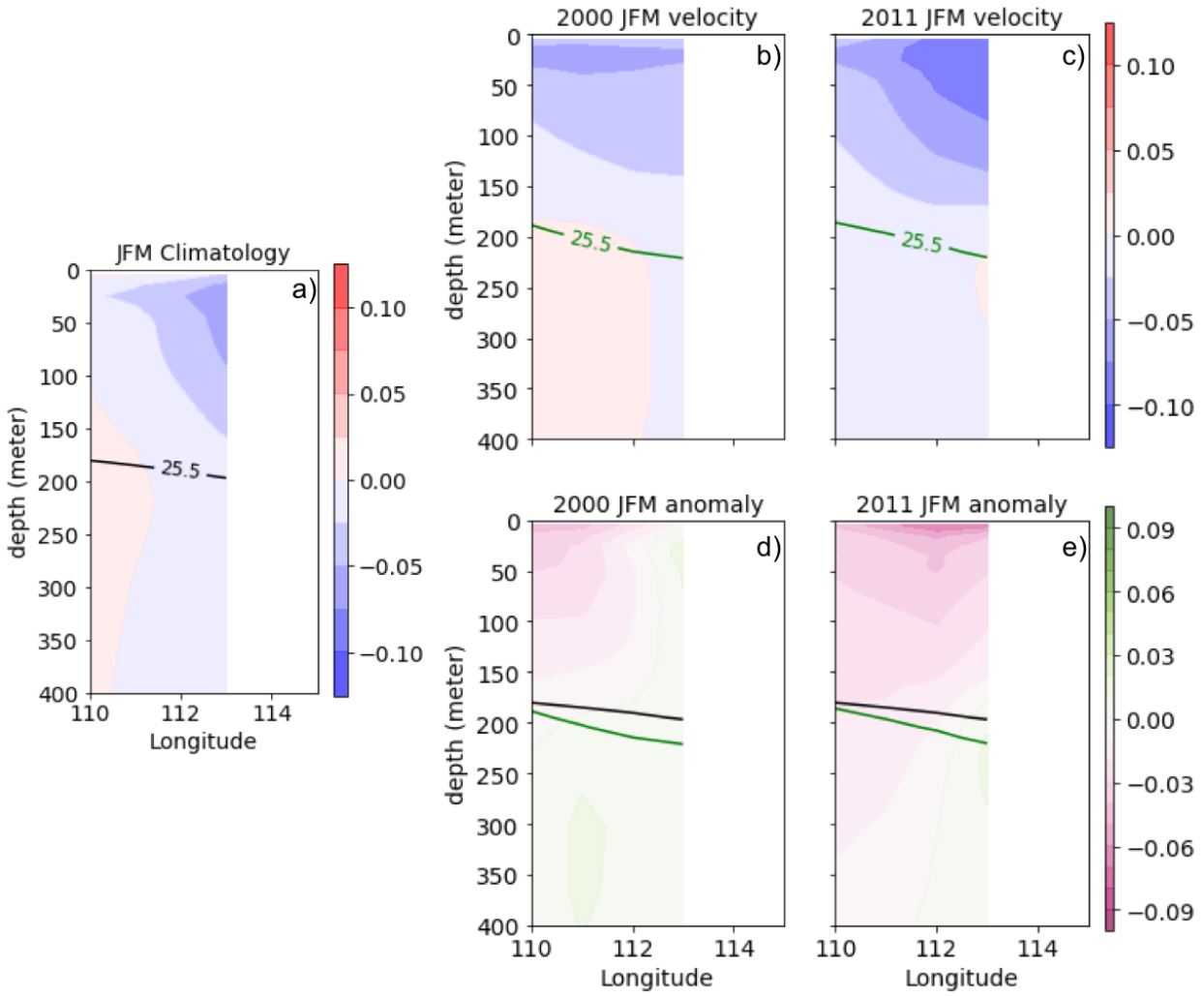


**Figure 3.14** Meridional velocity across 21.5ºS, the top of the LC box. a) shows the JFM climatology with blues indicating southward velocity and red northward. The 25.5**σ** isopycnal is shown by the black line. b) and c) show JFM meridional velocity during 2000 and 2011 respectively with colors as in a). The 25.5**σ** isopycnal is shown by the green line. d) and e) show the 2000 and 2011 anomaly from the climatology with purples as negative anomalies (stronger southward flow) and greens as positive anomalies (stronger northward /weaker southward flow). The climatological and 2000/2011 25.5**σ** isopycnals are shown by the black and green lines respectively. Both 2000 and 2011 see an increase in southward Leeuwin Current velocities during JFM.

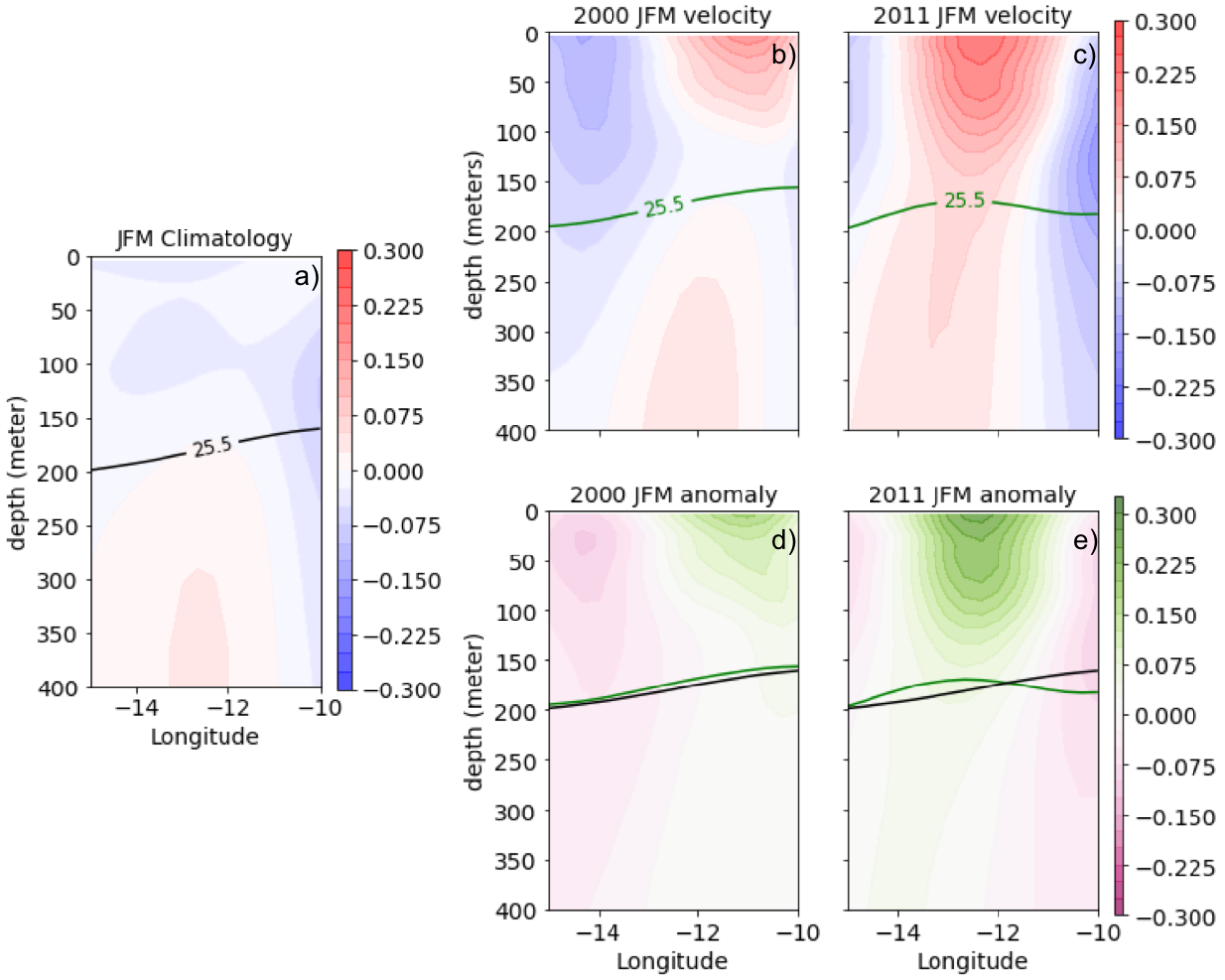


**Figure 3.15** Zonal velocity across 105ºE, the easternmost boundary of the SEC box. a) shows the JFM climatology with blues indicating westward velocity and red eastward. The 25.5**σ** isopycnal is shown by the black line. b) and c) show JFM zonal velocity during 2000 and 2011 respectively with colors as in a). The 25.5**σ** isopycnal is shown by the green line. d) and e) show the 2000 and 2011 anomaly from the climatology with purples as negative anomalies (stronger westward/weaker eastward flow) and greens as positive anomalies (stronger eastward /weaker westward flow). The climatological and 2000/2011 25.5**σ** isopycnals are shown by the black and green lines respectively. An increase of westward flow is present during JFM of both 2000 and 2011, although the increase was stronger in 2011.

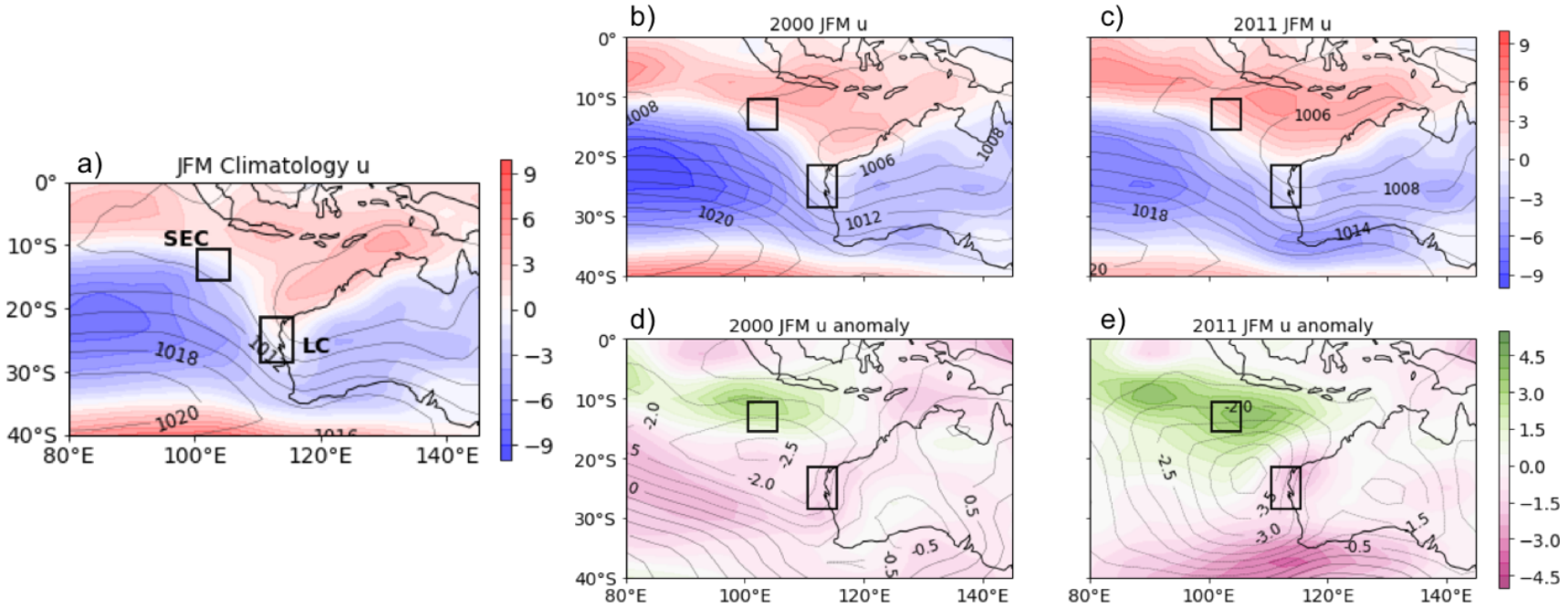
a)
JFM Climatology u
SEC
LC
1018
1020
0°
10°S
20°S
30°S
40°S
80°E
100°E
120°E
140°E
9
6
3
0
−3
−6
−9
b)
2000 JFM u
1008
1006
1012
1020
c)
2011 JFM u
1006
1008
1018
1014
d)
2000 JFM u anomaly
-2.0
-2.5
0.5
-0.5
e)
2011 JFM u anomaly
-2.5
-3.0
-0.5
1.5
4.5
3.0
1.5
0.0
−1.5
−3.0
−4.5

**Figure 3.16** Zonal wind speed at 1000HPa is shown by colored shading and MSLP as black contour lines. a) Climatological average of JFM with reds indicating westerly winds and blues easterly winds. b) and c) show zonal winds and MSLP during JFM of 2000 and 2011 respectively with colored shading as in a). d) and e) show JFM zonal wind anomaly from the climatology in colored shading with greens as positive anomalies (stronger eastward/weaker westward) and purples as negative anomalies (stronger westward/weaker eastward). MSLP anomalies are shown as black contours. A negative MSLP anomaly is present off the western coast of Australia during JFM of both 2000 and 2011. Positive zonal wind anomalies along 10ºS are also present, although weaker in 2000 than in 2011.

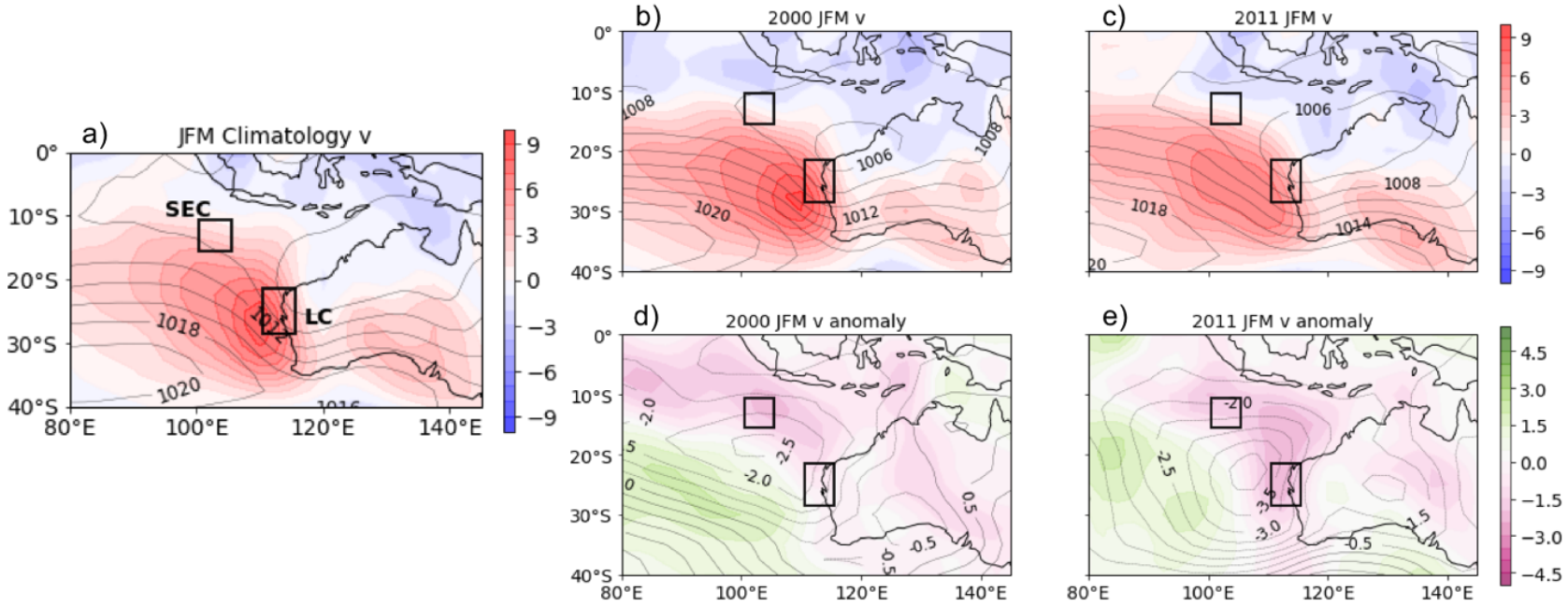
a)
JFM Climatology v
SEC
LC
1018
1020
0°
10°S
20°S
30°S
40°S
80°E
100°E
120°E
140°E
9
6
3
0
−3
−6
−9
b)
2000 JFM v
1008
1006
1020
1012
c)
2011 JFM v
1006
1008
1018
1014
d)
2000 JFM v anomaly
-2.0
-2.5
0.5
-0.5
e)
2011 JFM v anomaly
-2.5
-3.0
-0.5
4.5
3.0
1.5
0.0
−1.5
−3.0
−4.5

**Figure 3.17** Meridional wind speed at 1000HPa is shown by colored shading and MSLP as black contour lines. a) Climatological average of JFM with reds indicating southerly winds and blues northerly winds. b) and c) show meridional winds and MSLP during JFM of 2000 and 2011 respectively with colored shading as in a). d) and e) show JFM meridional wind anomaly from the climatology in colored shading with greens as positive anomalies (stronger northward/weaker southward) and purples as negative anomalies (stronger southward/weaker northward). MSLP anomalies are shown as black contours. The low pressure center off the west Australian coast during 2000 and 2011 is associated with anomalous cyclonic atmospheric circulation and a weakening of southerly winds in the Leeuwin Current region. This negative meridional wind anomaly is stronger in 2011 than in 2000.

The strong correlation between ENSO and LC transport is consistent with other studies (e.g. Feng et al. 2003). Meyers (1996) examine XBT line IX1 that connects western Australia with the western tip of Java and found that an ENSO signal was easily apparent in SST, dynamic height, and thermocline depth in the Leeuwin Current region, but that this signal was not as pronounced in the northern portion of the section (SEC region). This is also consistent with our finding that SEC outflow is not as well correlated with NINO3.4. It should be noted that Ningaloo Niño events discussed above are often associated with La Niña conditions in the Pacific, although this is not always the case as they may develop independently due to local air-sea feedbacks (e.g. Tozuka et al., 2014; Kataoka et al, 2018). The results of the correlation with DMI are less straightforward. The long lag time (>1.5 years for both time series) is difficult to explain, especially with regard to the SEC section, which is partially in the eastern box used to calculate the index. The correlations between the DMI and these transport time series likely do

not indicate a direct cause and effect relationship between changing DMI and transport. It is more likely that these correlations simply reflect the interconnected nature of the DMI and other regional climate forcing such as ENSO.

The correlation between the SEC and LC transport monthly mean time series reflects an alignment of seasonal cycles, as the SEC displays a minimum transport during April/May and a maximum outflow during September/October whereas the LC shows a minimum transport September/October and a maximum transport in April/May. There is a slight offset with the LC showing a maximum on average during April and the SEC showing a minimum on average during May, so the seasonal cycles are not identically opposite. The high negative correlations of the three clusters of 12-month running mean LC and SEC indicates that when one pathway's export is reduced, there is some compensation by the other. This is not a perfect balance though as the LC transport is much smaller than the SEC. The clustering present in Figure 3.11 reflects a weakening in the SEC over time as well as a trend toward a smaller amplitude seasonal cycle in both the LC and the SEC, especially in group C where the slope of the best fit line becomes less steep. As mentioned above, the LC is well correlated with ENSO and this trend toward a weaker seasonal cycle could be due to the presence of La Niña events (2008, 2011) at the beginning of the time series which would tend to increase LC flow during austral fall. This was followed by a relatively neutral period and then the large 2015 El Niño, which would decrease the strength of the LC. The progression from La Niña to neutral to El Niño states could present as a trend toward smaller amplitude seasonal cycles in the LC. Although the SEC is not as well correlated with ENSO as is the LC, the same trend from La Niña to El Niño could play a role. Further analysis of the weakening trend in the SEC is out of the scope of this paper, but is an avenue for future work.

## 3.5 Summary

The ITF waters exiting the Indo-Australian basin enter the western pathway of the South Equatorial Current, and the southern pathway of the Leeuwin Current. However, the ratio of the ITF outflow injected into either of these two pathways is not constant, but varies in response to larger scale regional wind forcing. Ningaloo Niño events in particular set up changes in atmospheric circulation that influence the SEC and LC. An anomalous low pressure center off the north west Australian Coast and resulting cyclonic circulation are characteristic of these events. During the 2011 and the somewhat weaker 2000 events, oceanic circulation shifted from the SEC as the primary conduit, to a reversal of flow in the SEC region and an anomalous strengthening of the Leeuwin Current. Throughout the Argo observational period 2005-2018, the SEC and LC act in tandem, with one pathway's export decreasing and the other increasing. In the context of heat transport the shift between these two pathways is especially important for local marine ecosystems, especially those off the coast of Australia which experienced changes in habitat and biodiversity during warming events (Wernberg et al. 2012). Climate change will likely alter the ITF, with a potential for a decreased ITF and associated decrease in Pacific to Indian heat transport (0.20 PW less, Ma et al., 2020) in the coming decades. Our study informs this climate change modelling work, showing that an understanding of changes in Indian Ocean heat content will require knowing the state of the ratio between the SEC and LC pathways. Further analysis of ITF propagation within the SEC is presented in Chapter 4.

# Chapter 4: ITF waters in the South Equatorial Current, and their relation to Indian Ocean thermocline variability

**Abstract**

The relatively low salinity waters of the ITF spread westward within the Indian Ocean by the South Equatorial Current from the Indo-Australian basin to the African Coast. Using gridded Argo float profiles, we find that the ITF plume (defined by the 34.6, 34.8 and 35.0 isohalines) varies in both westward propagation and in the latitude of the lowest salinity axis, at seasonal and interannual time scales. Within the eastern part of the basin, between 95°E and 110°E, the low salinity plume defined by the 34.6 isohaline propagates furthest west during October and November. Conversely, in the western part the basin, between 55°E and 75°E, the plume defined by the 35.0 isohaline is seen furthest west during June and July in response to seasonal development of the Seychelles Chagos Thermocline Ridge (SCTR). The salinity within the SEC region between 10°S-15°S shows a positive correlation with the depth of the 20°C isotherm (d20) within the SCTR region, indicating that there tends to be greater ITF propagation (lower salinity) associated with the shallower thermocline of a more pronounced SCTR. Two periods of reduced westward ITF plume propagation occur: in 2010/11 and 2016/17. These years were associated with anomalously strong, and unusually eastward, upwelling centers of the SCTR. This was a consequence of regional winds favorable to Ekman upwelling as well as an inhibition of the development of the annual westward propagating downwelling Rossby waves. The cyclonic circulation around these upwelling regions disrupted the zonal flow of the SEC reducing the westward transport of low salinity ITF waters.

## 4.1 Introduction

The relatively low salinity waters of the Indonesian throughflow (ITF) spread across the Indian Ocean within the South Equatorial Current (SEC) centered at 11°S. The SEC pathway along with a secondary pathway within the Leeuwin Current (Chapter 3) affect the heat inventory of the Indian Ocean (Lee et al., 2002; Hirst and Godfrey, 1993; Schneider, 1998). The SEC flowing from the Indo-Australian basin to Madagascar and the east African coast (Wyrtki, 1961; Schott et al., 2009), carries ITF waters primarily within the thermocline feeding into the Agulhas and Somali Currents (Gordon et al., 1997; Song et al., 2003; Qu et al. 2005). Below this thermocline flow, deeper ITF waters from the Banda Sea are also found within the South Equatorial Current (Talley and Sprintall, 2005). Although there is significant mixing along the way, Gordon et al. (1997) identifies waters of up to 60% ITF in the western portion of the Indian basin, and Durgadoo et al. (2017) suggests 45% of the Agulhas Leakage is of ITF origin. Although many studies have shown that the ITF does traverse the Indian Ocean within the SEC, the variability of the ITF within this pathway is poorly understood. This study seeks to understand the variability of the ITF within the SEC, and to investigate what influences the changes in its propagation.

An important feature of Indian Ocean thermocline in the SEC region is the Seychelles Dome. This upwelling region was recognized in models (Woodbury et al., 1989) and observations (Xie et al., 2002) as a unique trait of the southwest tropical Indian Ocean. Hermes and Reason (2008) describe this as the Seychelles Dome upwelling center located at around 8°S and 60°E and note a secondary upwelling center at 11°S and 90°E (Chagos Dome; CD). They describe these two domes sometimes linking to form a ridge, the Seychelles Chagos Thermocline Ridge (SCTR; Figure 4.1), noting that the features are more defined in austral fall to winter,

periods marked by negative wind stress curl that is conducive to Ekman upwelling. A cyclonic circulation is set up by this upwelling, and the southern branch coincides with the SEC in the western half of the Indian basin.

This observational study uses gridded Argo datasets to examine the ITF within the SEC, and identify its pathways on seasonal and interannual timescales. Anomalous ITF propagation events are identified and their links to Indian Ocean thermocline variability and regional winds are investigated.

## 4.2 Methods

To investigate the propagation of the ITF within the SEC we use salinity within the upper thermocline as a proxy for the ITF. We focus on observations using gridded Argo data distributed by the Asia Pacific Data Research Center (retrieved from http://apdrc.soest.hawaii.edu/projects/argo/ ) which is at 1° by 1° spatial resolution and monthly temporal resolution from January 2005 to December 2018. We examine salinity on a density surface within the SEC thermocline, choosing to use the 24$\sigma$ surface to be consistent with Gordon et al. (1997). The three isohalines investigated are 34.6, 34.8 and 35.0. In the immediate ITF outflow region in the eastern tropical Indian Ocean the salinity of ITF waters is around 34.6 for most of the upper water column (see Figure 1.2 in Chapter 1). As these waters propagate westward within the SEC, there is mixing with surrounding waters and the salinity increases. Therefore, as we follow the ITF across the basin isohalines of successively higher salinity must be used. As the Argo data is reported at standard depths, we use a spline interpolation at each grid point and each time step to interpolate salinity to 24$\sigma$. We examine the changes in the thermocline using the depth of the 20°C isotherm (d20) as a proxy as is done in other studies examining the Seychelles Dome (e.g. Hermes and Reason, 2008; Tozuka et al., 2010). The

SCTR is investigated by averaging d20 within a box bounded by 4.5°S-12.5°S and 50.5°E-90.5°E, as well as by examining the minimum depth of the 20°C isotherm at each time step within the study domain of 0.5°N-21.5°S and 40.5°E-120.5°E (d20min). The centroid of the lowest (shallowest) d20 contour is determined using Green's Theorem in the method of Bingham et al. (2019). The centroid is the approximate location in latitude-longitude space of the center of the upwelling region, which we use to examine spatial patterns of the upwelling over time. Niño 3.4, defined as the sea surface temperature anomaly over 90°–150°W, 5°S–5°N, data is retrieved from https://www.cpc.ncep.noaa.gov/data/indices/. All correlations reported are significant to the 95% confidence interval.

Changes in thermocline currents are examined with GODAS reanalysis (Behringer & Xue, 2004; https://psl.noaa.gov/data/gridded/data.godas.html) which provides monthly u and v at 0.333° latitude by 1° longitude spatial resolution from January 1980 until July 2020. To be consistent with Argo data we create a climatology of subsurface velocity by averaging only over the overlapping time period (2005-2018).

As both local winds and remote forcing are known to influence thermocline features in this region of the Indian Ocean, we investigate both wind driven Ekman upwelling and Rossby wave propagation. To examine Ekman upwelling in the region we follow previous SCTR work and use the upwelling equation from Takaaki et al. (2008) to calculated the vertical velocity (w ) as follows:

$$W = \frac{\partial h}{\partial t} - c\frac{\partial h}{\partial x} = \nabla \times \left(\frac{\tau}{\rho_o f}\right) = \frac{1}{\rho_o f}\nabla \times \tau + \frac{\beta \tau^x}{\rho_o f^2}$$

Here we focus on the two terms on the right side of the equation which will be referred to as, from left to right, the curl term and the β-term. The β-term is influenced by the seasonally reversing winds of the Indian Ocean Monsoon whereas the curl term is influenced both by the

Monsoon, as well as the persistent southeasterly winds in the southern portion of the basin. Within the equation c is the Rossby wave phase speed, $\tau$ is the wind stress, $\rho_o$ is the reference density assumed here to be 1025 $kgm^{-3}$, f is the Coriolis parameter, and $\beta$ is df/dy. Winds within the region are from NCEP/NCAR Reanalysis 1 (Kalnay et al., 1996; https://psl.noaa.gov/data/gridded/data.ncep.reanalysis.pressure.html) and are at 2.5° by 2.5° spatial resolution and monthly temporal resolution from 1948 until 2019, although we only consider values over the Argo time period (2005-2018). Windstress $\tau$ is estimated using the following equation:

$$\tau = \rho_{air} C_d |U| U$$

where $\rho_{air}$ is the density of air estimated as 1.22 $kgm^{-3}$, $C_d$ is the drag coefficient estimated as 0.0013 and U is the windspeed in $ms^{-1}$.

Lastly, we examine Rossby wave propagation within the region by examining sea surface height (SSH) at 10°S to be consistent with previous studies (e.g. Hermes and Reason, 2009). The sea surface height data is from the Global Ocean Multimission altimeter gridded dataset which combines data from all satellite altimeter measurements (https://resources.marine.copernicus.eu/?option=com_csw&view=details&product_id=SEALEVEL_GLO_PHY_L4_REP_OBSERVATIONS_008_047). This monthly mean dataset is at quarter degree resolution.

### 4.3 Results

The low salinity ITF plume within the SEC thermocline varies on seasonal time scales, although the timing of maxima and minima of westward propagation of low salinity water vary with longitude in the basin (Figures 4.1 and 4.2).

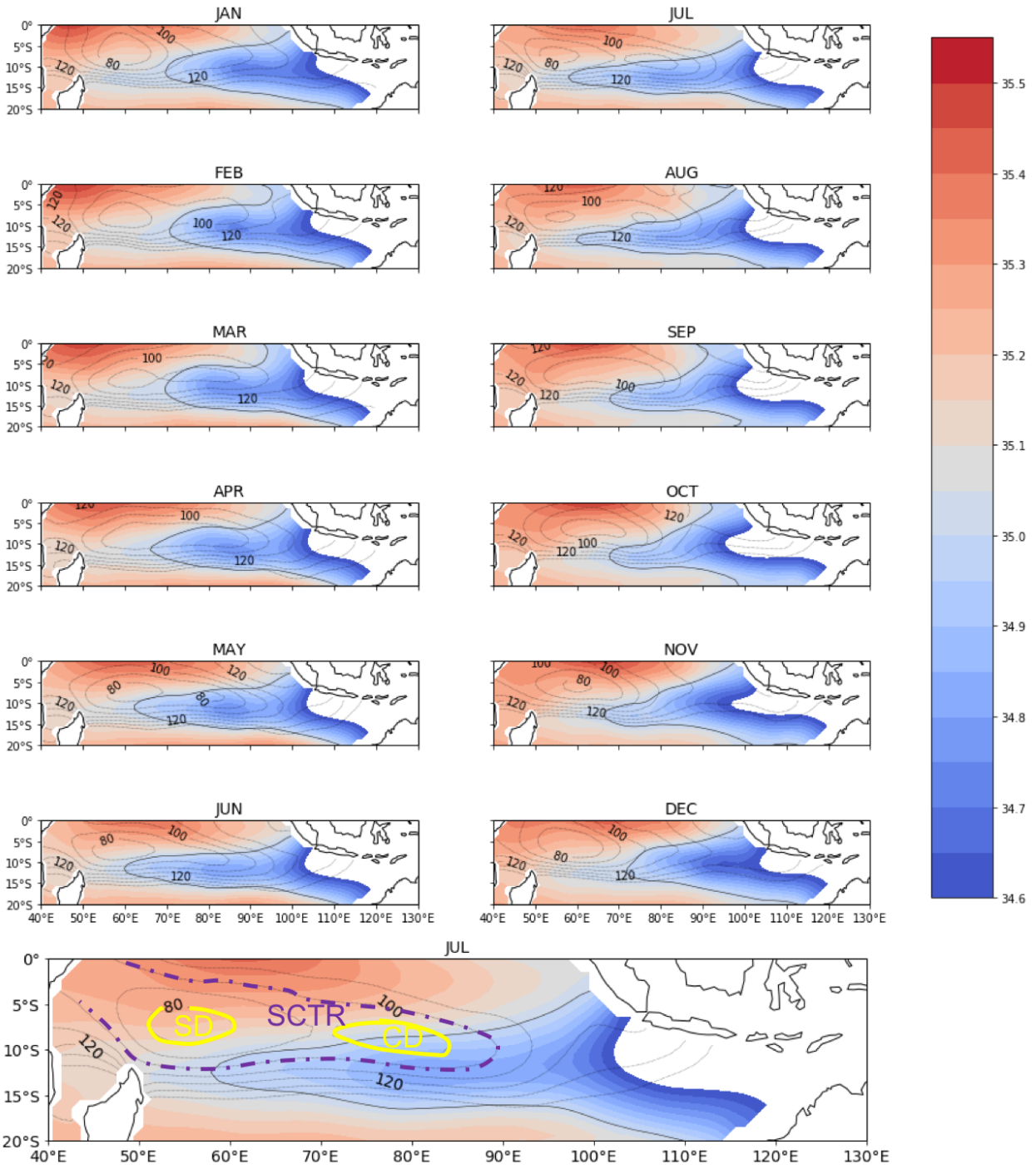


**Figure 4.1** Seasonal cycle of salinity along 24σ and depth of the 20°C isotherm (d20) in the ITF plume region from Argo gridded data. The 35.0 isohaline is outlined in solid black. The depth of the 20°C isotherm is shown in dotted lines at 10 m intervals. During the austral winter, as the Seychelles Chagos Thermocline Ridge strengthens (shallower d20 in the western portion of the

basin), the 35.0 salinity contour follows the steep slope along the southern boundary of the ridge, reaching its furthest extent. The SCTR (purple), SD and CD (yellow) are highlighted in the bottom enlarged plot of July.

In the far eastern portion of the basin we examine the 34.6 salinity contour (Figure 4.2). The furthest westward propagation of this contour appears in October and November whereas propagation is most attenuated during January and February. The 34.8 contour, representing the ITF plume in the center of the Indian basin, propagates farthest during March, and least during June and July. Portions of low salinity waters continue propagating westward, cut off from the main plume, in the intervening months of April and May. The 35.0 isohaline propagates farthest during June, July, and August and is more attenuated in December and January.

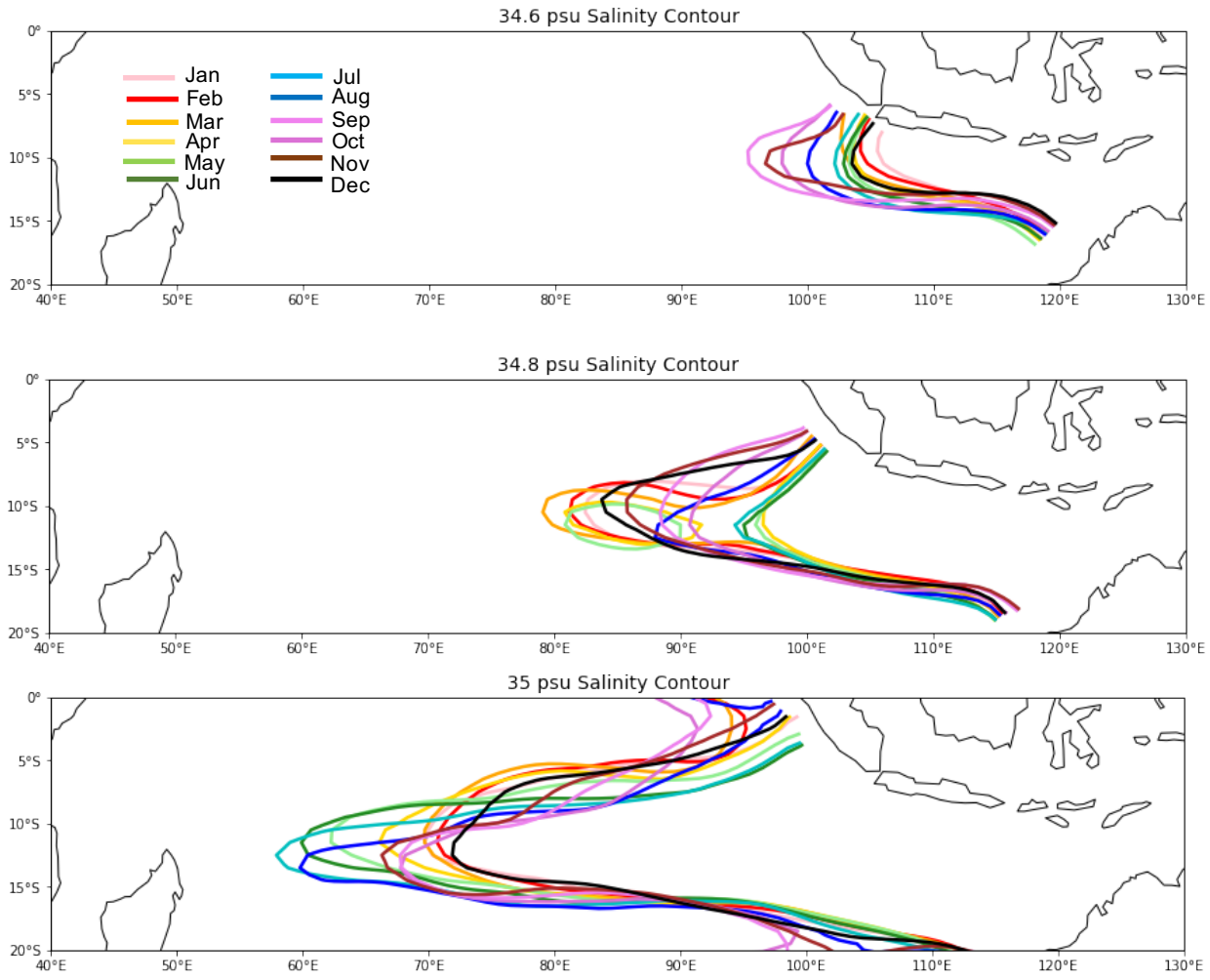


**Figure 4.2** Monthly mean climatology of salinity contours, averaged 2005-2018, along 24σ. ***Upper panel:*** Monthly mean 34.6 salinity contours. Westward propagation is attenuated during January-February and progresses further westward throughout the year to a maximum in October-November. ***Middle panel***: Monthly positions of the 34.8 contour. Contour is furthest west during March. ***Lower panel:*** Monthly positions of the 35.0 salinity contour. The plume is latitudinally wider and furthest to the east during December, and furthest to the west during July.

Figure 4.3 shows the seasonal cycle in terms of the mean salinity at each degree of longitude averaged within a 9.5°S to 15.5°S band, and the latitude of the minimum salinity at

each degree of longitude within the domain of 5.5°S to 15.5°S, 50.5°E to 120.5°E. We see that low salinity ITF water spreads from the Indo-Australian basin into the westward flowing SEC during austral spring to summer, and continues to move westward, mixing with surrounding Indian Central Water into the fall and winter. The plume axis tends to be located further to the north in the eastern part of the basin. Between 100°E and 110°E the minimum salinity tends to be located at around 9.5°S to 10.5°S. This northward positioning is present to the west of 100°E, out to around 80°E, during the austral summer. To the west the plume shifts further to the south with minimum values as far south as 15.5°S during austral winter. A southward shift begins during austral fall when minimum values are present at 12.5°S at 90°E and the austral winter when a minimum at 15.5°S can be seen as far east as 70°E. In the western part of the basin the seasonality of thermocline depth is related to the intensity of the Seychelles Dome. During the austral winter the SCTR strengthens, causing an upwelling of the thermocline roughly between 5°S-10°S and 50°E to 80°E. This creates a meridional steepening of the d20 contours, and causes a sloping of isopycnals to the south. This density gradient strengthens the westward geostrophic current, enhancing the SEC and drawing the ITF further across the Indian Ocean.

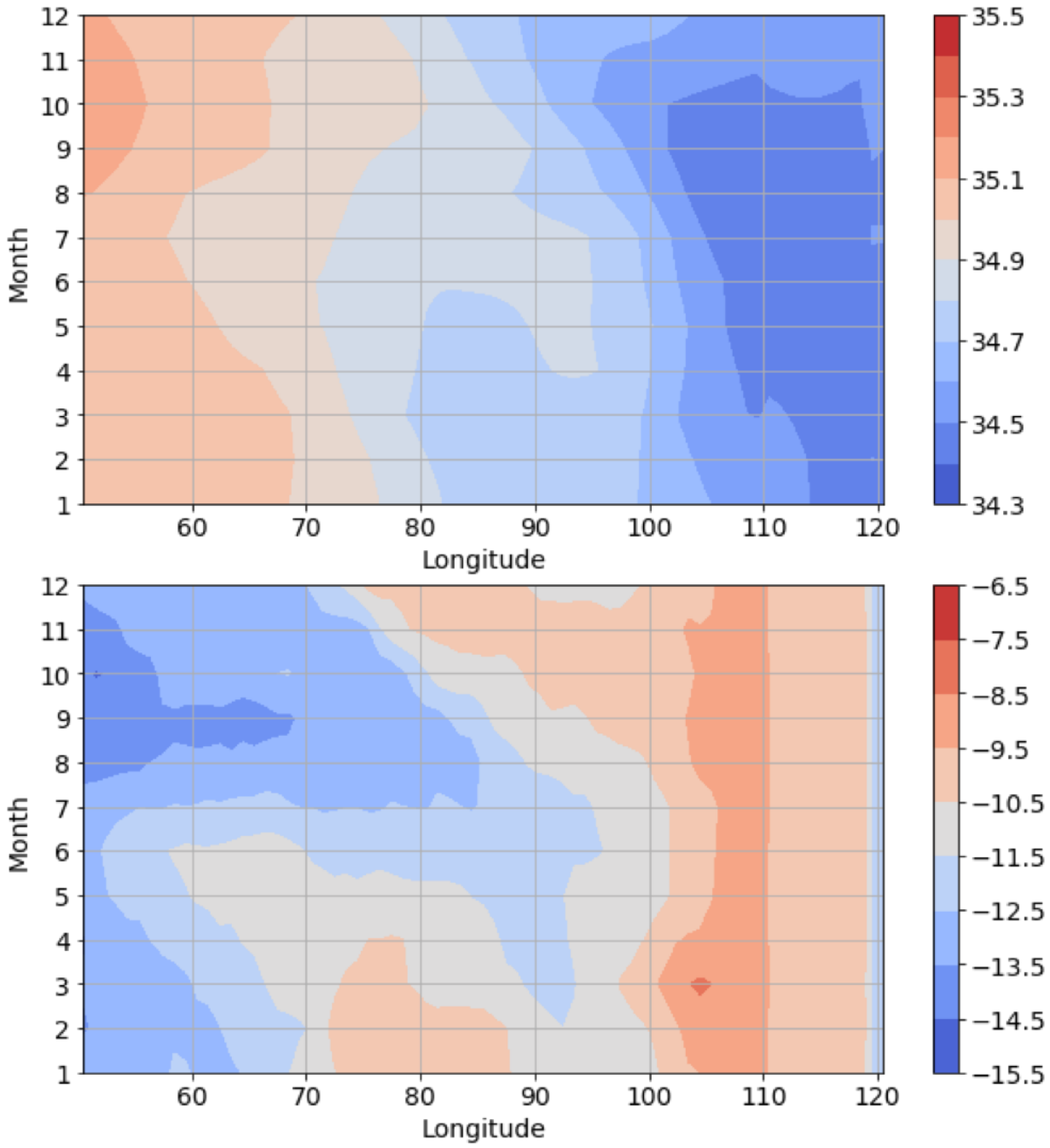


**Figure 4.3** ***Top*** Seasonal cycle of ITF propagation as shown by salinity along 24σ averaged between 9.5°S and 15.5°S. ***Bottom*** Latitude of the lowest salinity at each degree of longitude within the 5.5°S to 15.5°S domain. Consistent colored shading to the east of 110°E is due to

topography preventing meridional movement of the plume. Months are numbered 1-12 starting with January ending with December.

In addition to the seasonal cycle in the ITF plume there is also interannual variability. In Figure 4.4 *left* the salinity along 24σ is averaged between 9.5°S and 15.5°S. The seasonal cycle can be seen as well as periods where the low salinity waters appear to reach father across the basin and times when they recede. Figure 4.4 *right* shows this variability more clearly, as the salinity anomaly from the climatological mean is plotted with a 12-month running mean. There are periods of anomalously high salinity, such as 2010/11 (B) and 2016/17 (A), which indicate less ITF water made its way across the basin, and conversely periods of decreased salinity, such as 2009/10 (C), suggesting a further westward propagation of the ITF.

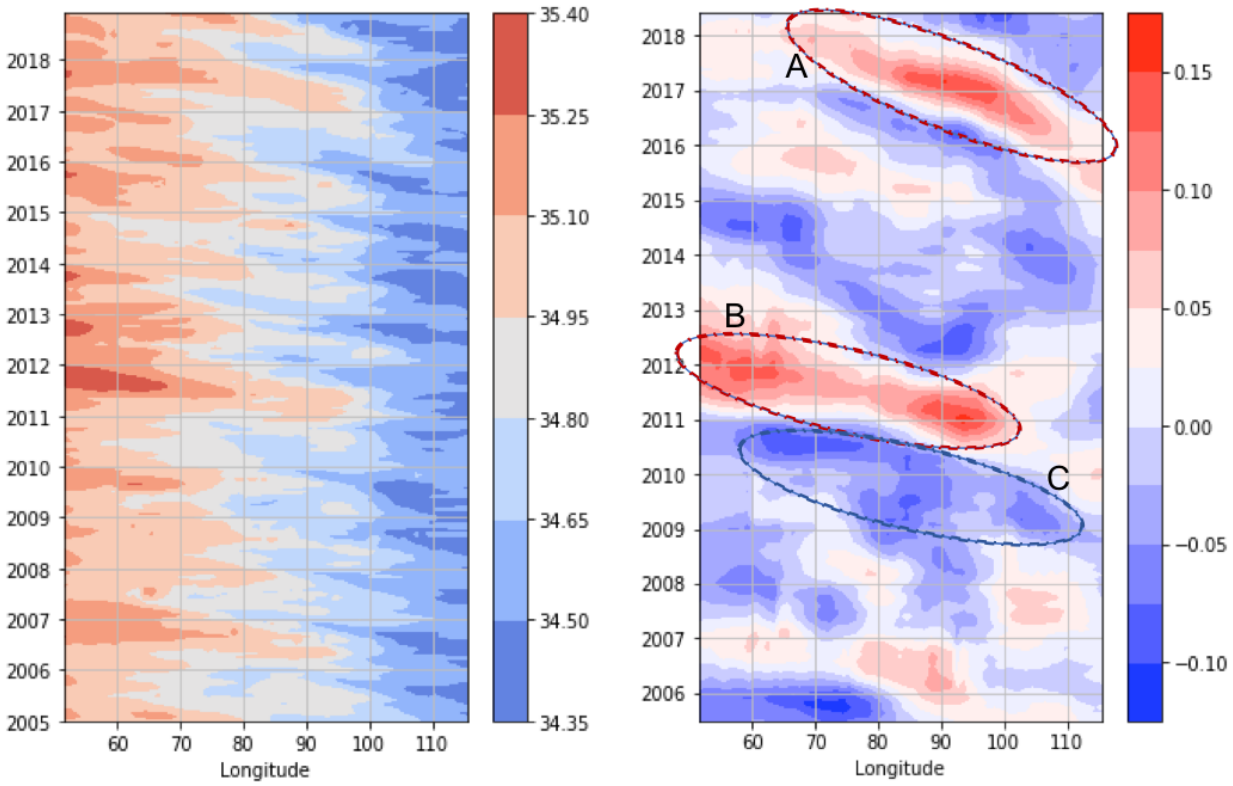


**Figure 4.4** ***Left*** Salinity along the 24σ surface averaged between 9.5°S and 15.5°S. Low salinity values are present in the eastern part of the basin at close to the outflow region of the ITF with higher salinity values to the west. The seasonal cycle in salinity can also be seen. ***Right*** 12-month running mean of salinity anomaly from climatological mean along the 24σ surface averaged between 9.5°S and 15.5°S. Positive anomalies are suggestive of decreases in ITF propagation; negative anomalies mark ITF increases. A and B show the decreases in ITF during 2016/17 and 2010/11 respectively. C shows an ITF increase during 2009/10.

In addition to this variability in the longitudinal propagation of the ITF plume, there is also a latitudinal shift. Figure 4.5 *left* shows the latitude of the lowest salinity at each degree of longitude within the ITF plume domain (5.5°S to 15.5°S), and Figure 4.5 *right* shows the anomaly from the climatological mean with a 12-month running mean. During 2010/11 (B) and

2016/17 (A) the low salinity signal is up to 3 degrees further south when compared with climatology, with the anomaly centered between 80°E and 100°E. Conversely, during 2007 (C) this low salinity signal is up to 3 degrees further north.

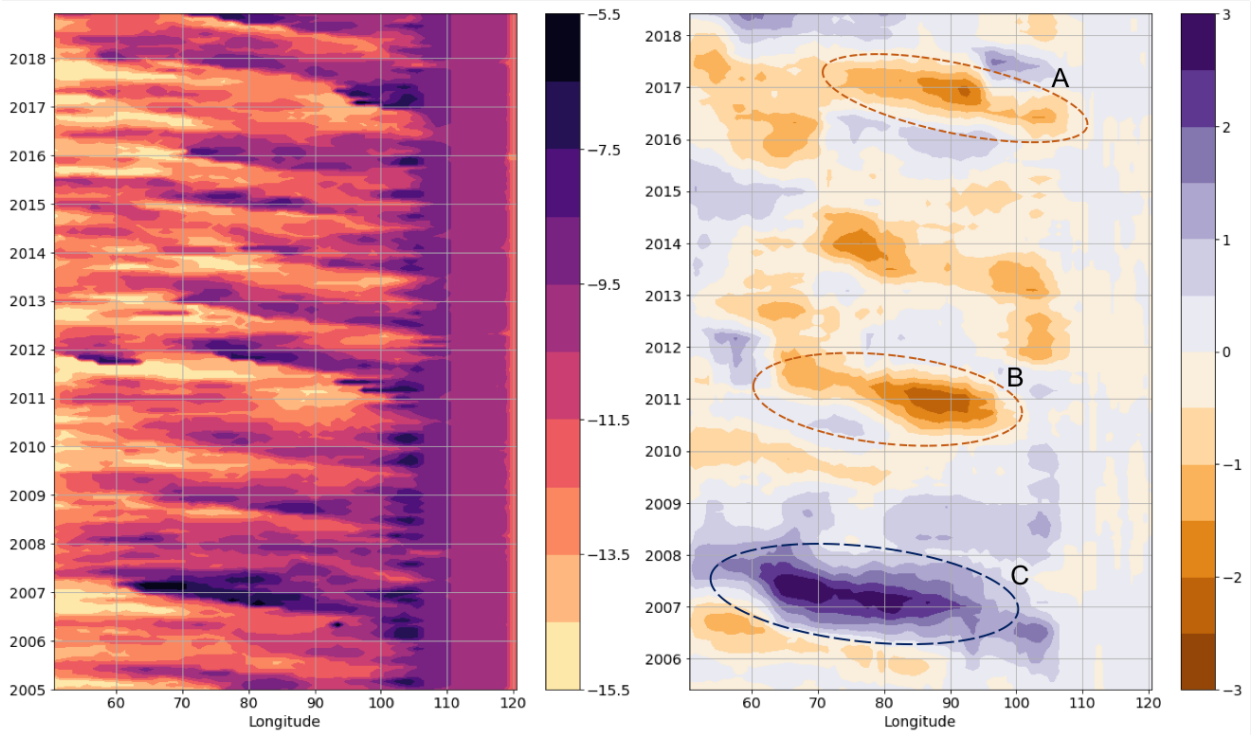


**Figure 4.5** ***Left*** Hovmöller diagram showing the latitude of lowest salinity along the 24σ surface within the ITF plume region (5.5°S to 15.5°S) within the Indian Ocean. Purples indicate further northward and oranges further southward. ***Right*** 12 month running mean of latitude anomaly (from right). Purples indicate an anomalous northward shift and oranges an anomalous southward shift. A and B highlight shifts to the south during 2010/11 and 2016/17. C shows a shift to the north during 2007.

Above analysis of the seasonal cycle suggests that the SCTR may play a role in ITF propagation as its development can alter the local geostrophic circulation by increasing meridional density gradients. The lower panel of Figure 4.6 shows the correlation of d20

averaged over the SCTR region (Figure 4.6 *top panel*) with the salinity along 24σ at each grid point within the study domain. There is a zonal region of positive correlation, with a maximum r of 0.5, from 90°E to the western edge of the domain primarily between 10°S and 15°S. The positive nature of the correlation indicates that when the d20 in the yellow SCTR box becomes smaller (shallowing of the thermocline) salinity in this region becomes lower (increasing ITF input present).

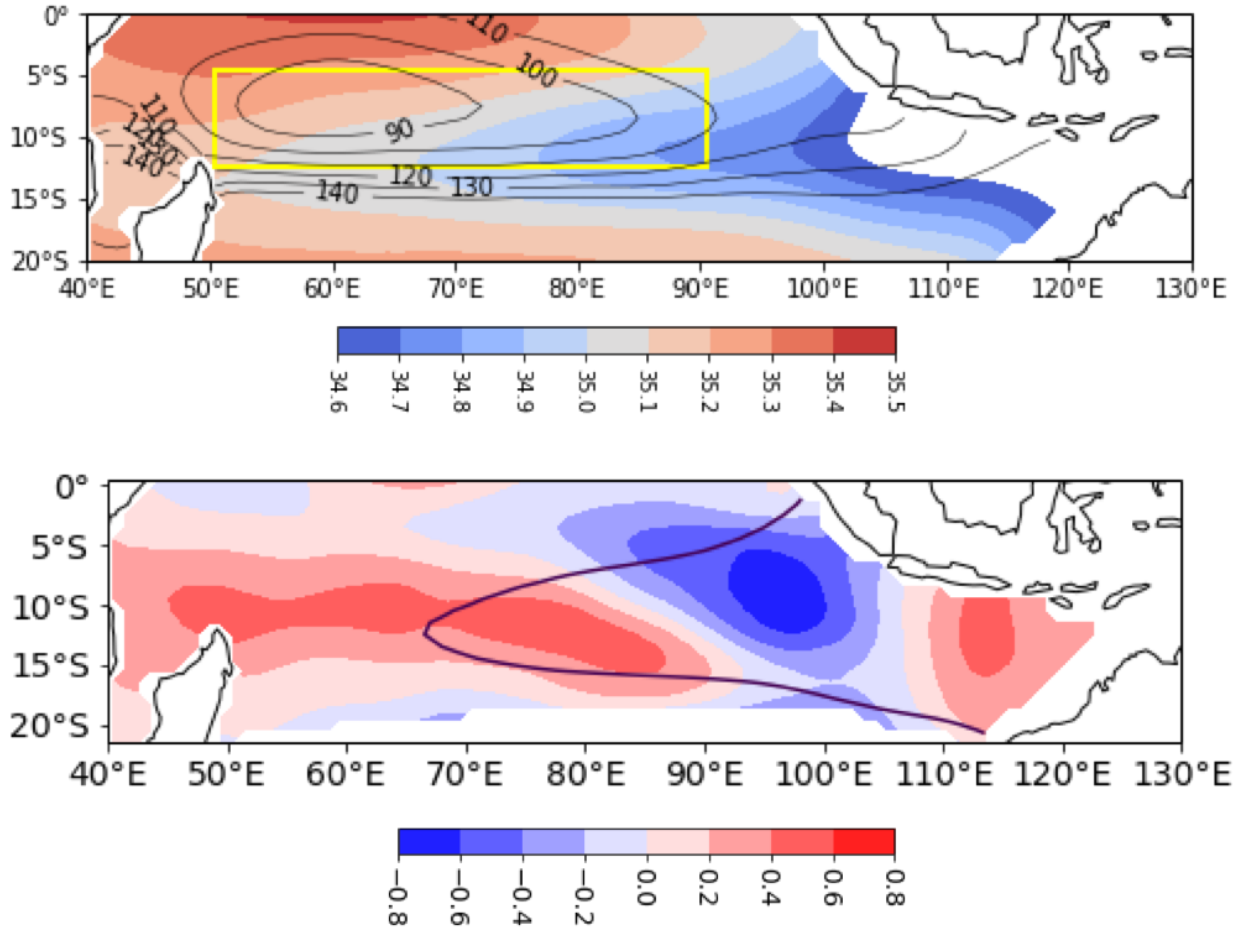


**Figure 4.6** ***Top*** Climatological salinity along the 24σ surface. The ITF is seen as a plume of low salinity water spreading westward. The contours show the depth of the 20°C isotherm. A region of shoaling of the d20 is observed within the yellow box. ***Bottom*** Monthly mean salinity

at each gridpoint was correlated with the d20 averaged within the yellow box. Positive correlation indicates lower salinity when the averaged d20 is shallower, and negative correlation lower salinity with a deeper d20. The climatological position of the 35.0 isohaline is shown in a solid line to demonstrate the path of the ITF. The region along this path within the SEC westward of 90°E shows a positive correlation, indicating that there is reduced salinity (more ITF input) in this region when the d20 within the yellow box is shallow.

To see if the location of this upwelling feature was related to its strength, we examined the centroid of the shallowest d20 contour. The Seychelles Dome is usually located in the western part of the basin and elongates to join the more eastward Chagos Dome as the year progresses. Figure 4.7 plots the latitude of the centroid against the longitude and colors the markers by the minimum d20 at the same time step. A cluster of points is present in the lower left quadrant, indicating that most of the time the centroid of the shallowest contour is in the characteristic Seychelles Dome region. As this is where the upwelling feature persists throughout the year this is not a surprising result. Additionally, most of the shallower data were within this cluster of points. When the centroid of the minimum contour was outside of this lower left quadrant, for example as far east as 90°E, the minimum d20 tended to be comparatively deep. Examining just the latitude and longitude of the centroid, it is apparent that they are not well correlated with each other.

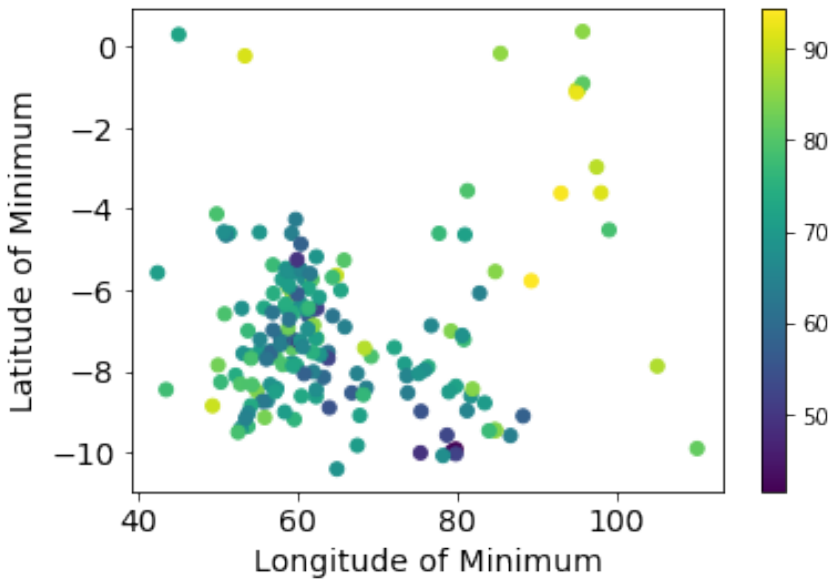


**Figure 4.7** The longitude of the minimum d20 is plotted against the latitude of the minimum d20 and colored by the depth at that point. In agreement with past studies, the minimum d20, often marking the location of the SCTR, is most often located between 6°S and 10°S in the western part of the basin between 50°E and 70°E.

To more closely examine the positive salinity anomalies during 2010/11 and 2016/17 from the hovmöller diagram in Figure 4.3 we plot the salinity along the 24σ and contours of the d20 in map view in Figures 4.8 and 4.9. During 2010/11 there is an anomalous upwelling feature centered at around 80°E and 10°S starting in September of 2010 and lasting through August of 2011. This upwelling raises the thermocline by more than 50 m when compared with climatological values (Figure 4.10). The propagation of the low salinity signal is also unusual during 2010/11, with the 34.8 salinity contour only reaching 100°E during austral summer and fall (averaged December, January, February: DJF and March, April, May: MAM) of 2011 compared with around 80°E for the climatology (Figure 4.12).

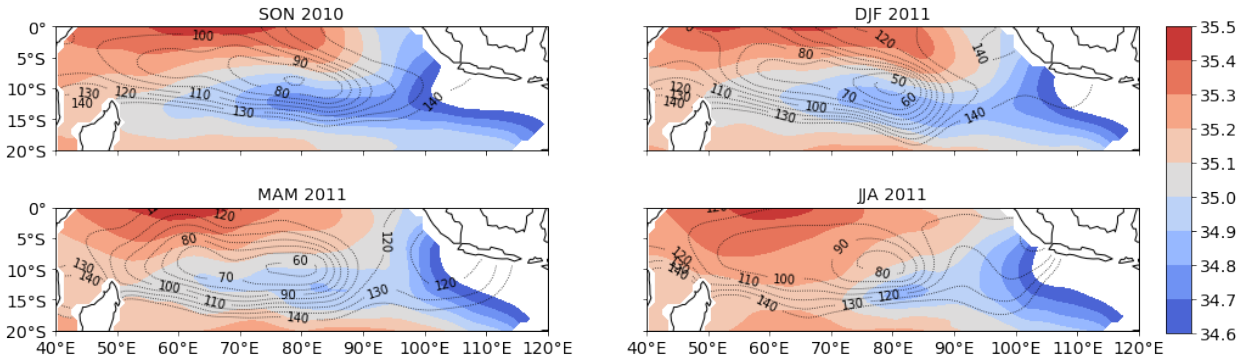


**Figure 4.8** Salinity along the 24σ surface during late 2010 into 2011 where SON is averaged September, October, November; DJF averaged December, January, February; MAM averaged March, April, May; JJA averaged June, July, August. Dotted lines show the depth of the 20°C isotherm (d20). Strong upwelling is present centered at 80°E, 10°S starting during September 2010 and continuing into 2011.

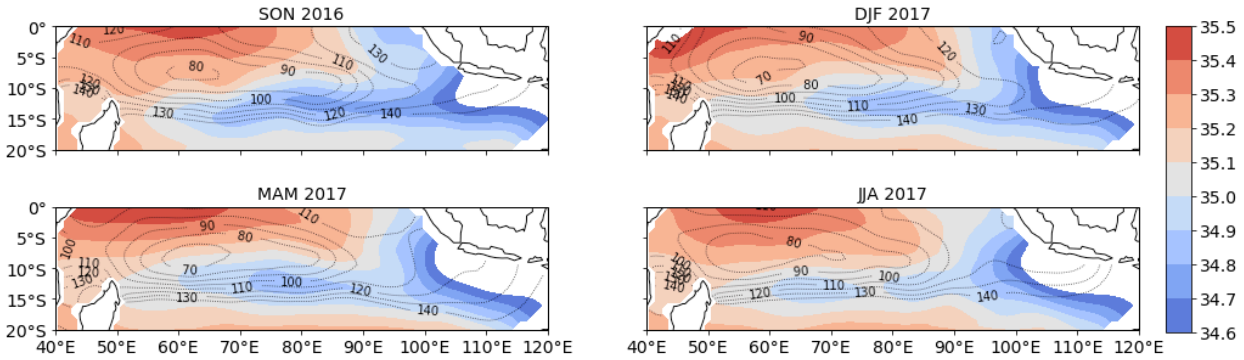


**Figure 4.9** Salinity along the 24σ surface as in Figure 4.8 but for late 2016 into 2017. A ridge of upwelling is present from 60°E to 90°E at around 8°S starting in September of 2016 and continuing into 2017.

Salinity and thermocline depth during 2016/17 show similar anomalies. During 2016/17 there is an anomalous upwelling across much of the domain from 50°E to 90°E with the strongest shoaling of the thermocline of about 30 m shallower than climatology centered

between 80°E and 90°E during austral spring (averaged September, October, November: SON) of 2016 (Figure 4.11). This feature weakens and shifts westward through austral winter (averaged June, July, August: JJA) of 2017. As in 2011, the 34.8 salinity contour is about 20 degrees of longitude further eastward during DJF and MAM of 2017 when compared with climatology (Figure 4.12).

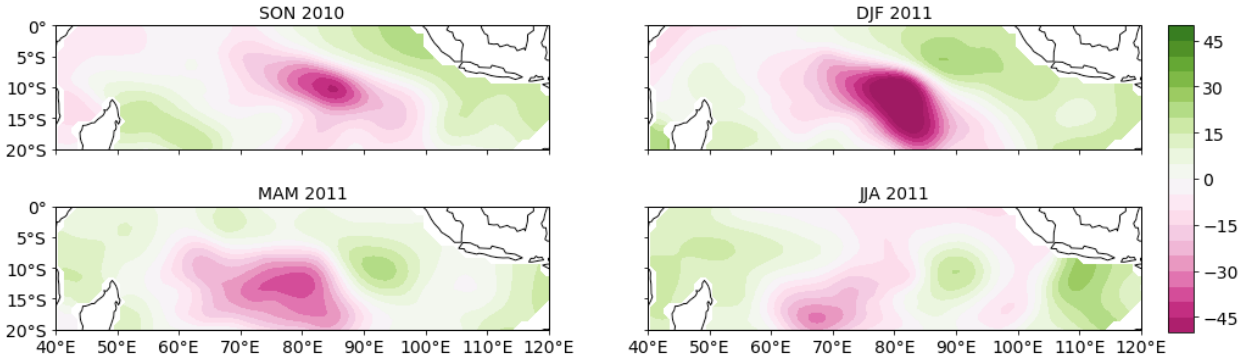


**Figure 4.10** Depth of the 20°C isotherm anomaly from the seasonal cycle is plotted for late 2010 into 2011 with months averaged as in Figure 4.8. Green colors indicate a deeper thermocline (downwelling) than climatology and pink colors a shallower thermocline (upwelling). A strong shallow anomaly is present between 70°E and 90°E beginning in September of 2010 and continuing into May of 2011.

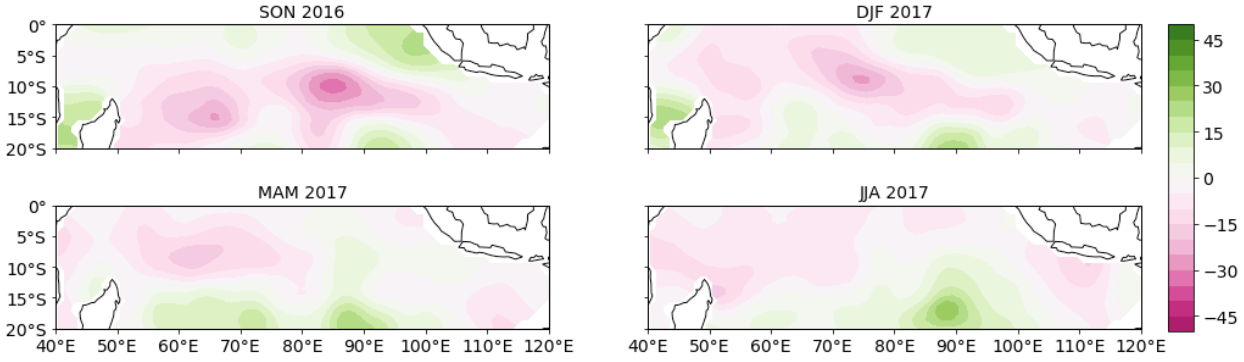


**Figure 4.11** D20 anomaly is plotted as in Figure 4.10 but for 2016 into 2017. A shallow anomaly is present between 50°E and 100°E with the strongest shallowing between 80°E and

90°E during SON of 2016. The upwelling anomaly is present starting in September 2016 through February 2017 and is weakened but still present through August 2017.

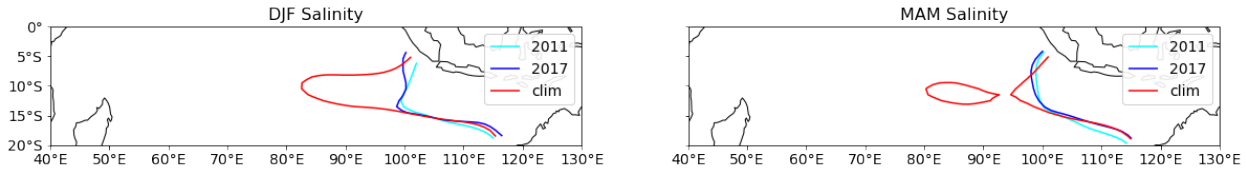


**Figure 4.12** 34.8 salinity contour along the 24σ surface during DJF (left) and MAM (right). 2011 is shown as the light blue contour, 2017 as the dark blue contour, and the climatology as the red contour. During 2011 and 2017 the 34.8 contour is about 20° of longitude further east than the climatology, indicating decreased westward ITF propagation during those years.

Figure 4.13 shows subsurface currents at 105 m depth from GODAS reanalysis as well as d20 and the 34.8 isohalines from Figure 4.12. During 2010/11 and 2016/17 a cyclonic circulation develops around the upwelling center beginning in SON and persisting into the following year. This cyclonic circulation is present in MAM of the climatology when the SCTR is generally strongest and most zonally elongated. In both 2010/11 and 2016/17 the zonal SEC is disrupted as the westward flow on the southern flank of the upwelling is further south than usual, and eastward and southward flows (on the northern and eastern sides of the upwelling) are present in the path of the SEC.

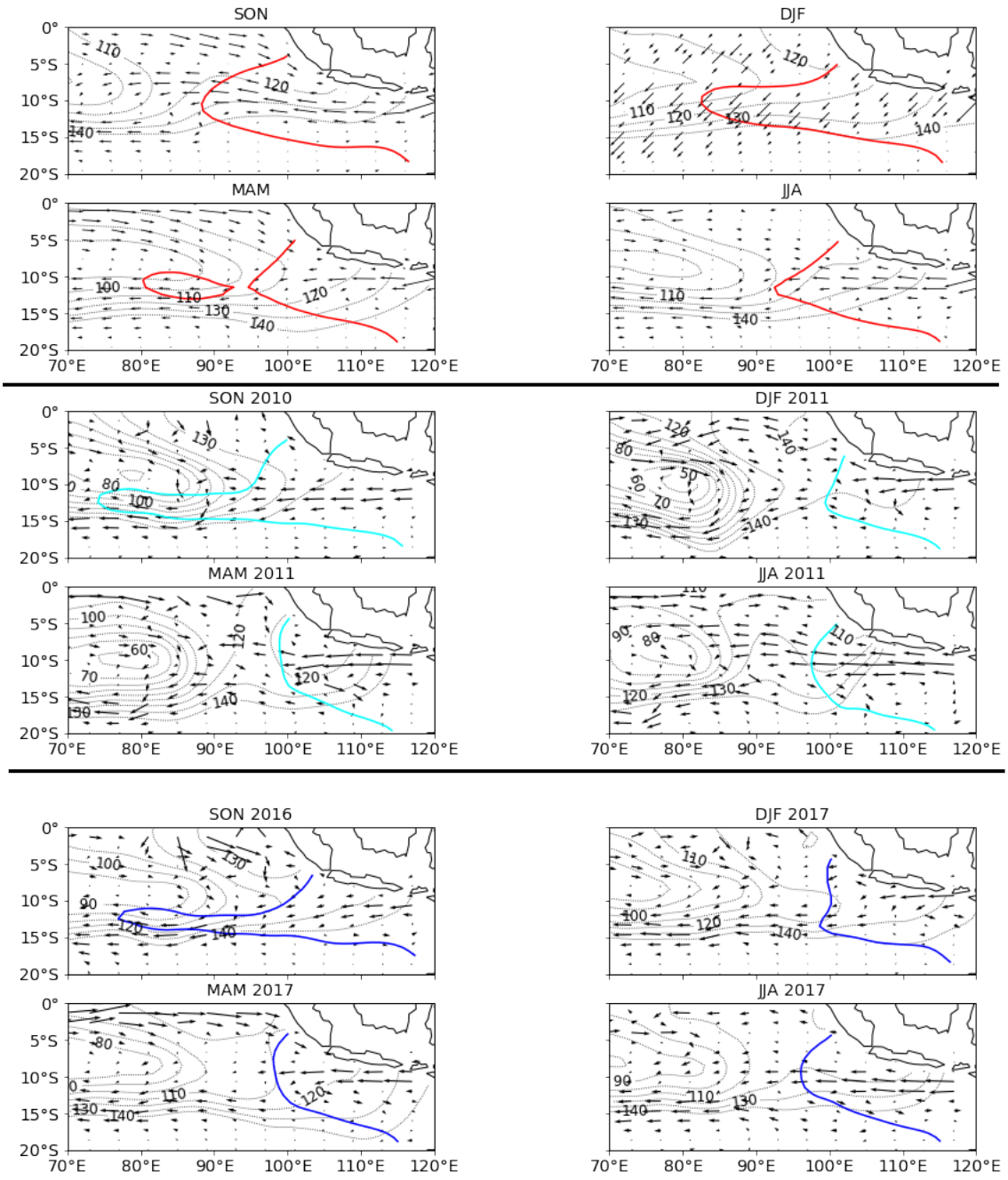


**Figure 4.13** ***Top*** Climatology of GODAS currents at 105 m averaged during September, October, November (SON); December, January, February (DJF); March, April, May (MAM); and June, July, August (JJA). ***Middle*** GODAS currents at 105 m during 2010/11. ***Bottom***

GODAS currents at 105 m during 2016/17. Grey contour lines show d20 and colored contour lines depict the 34.8 isohaline as in figure 4.12.

To understand what is influencing this thermocline shoaling we investigate the vertical velocity associated with Ekman upwelling over the anomalous d20 region (76.25°E to 88.75°E and 6.25°S to 16.25°S) which is plotted in Figure 4.14. During 2010/11 and 2016/17 upwelling velocity of about 0.6 x $10^{-5}$ $ms^{-1}$ is present.

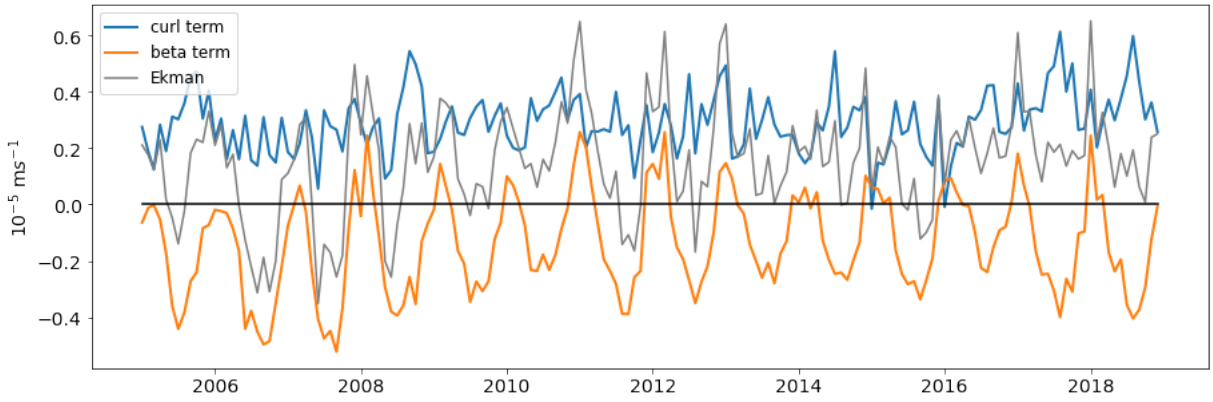


**Figure 4.14** Mean vertical velocity over the anomalous upwelling region (76.25°E to 88.75°E and 6.25°S to 16.25°S) calculated from NCEP/NCAR reanalysis winds. The total Ekman pumping velocity is plotted in the grey line, the portion due to the wind stress curl term in the blue line and the portion due to the β-term in the orange line. Positive values indicate upwelling.

As it is known that changes in d20 within this region are not solely forced by Ekman pumping (Matsumoto and Meyers, 1996), we also examine remote forcing in the form of the annual downwelling westward propagating Rossby waves. We find that during late 2010 and late 2016 there is no downwelling Rossby wave (Figure 4.15) that we see in the other years.

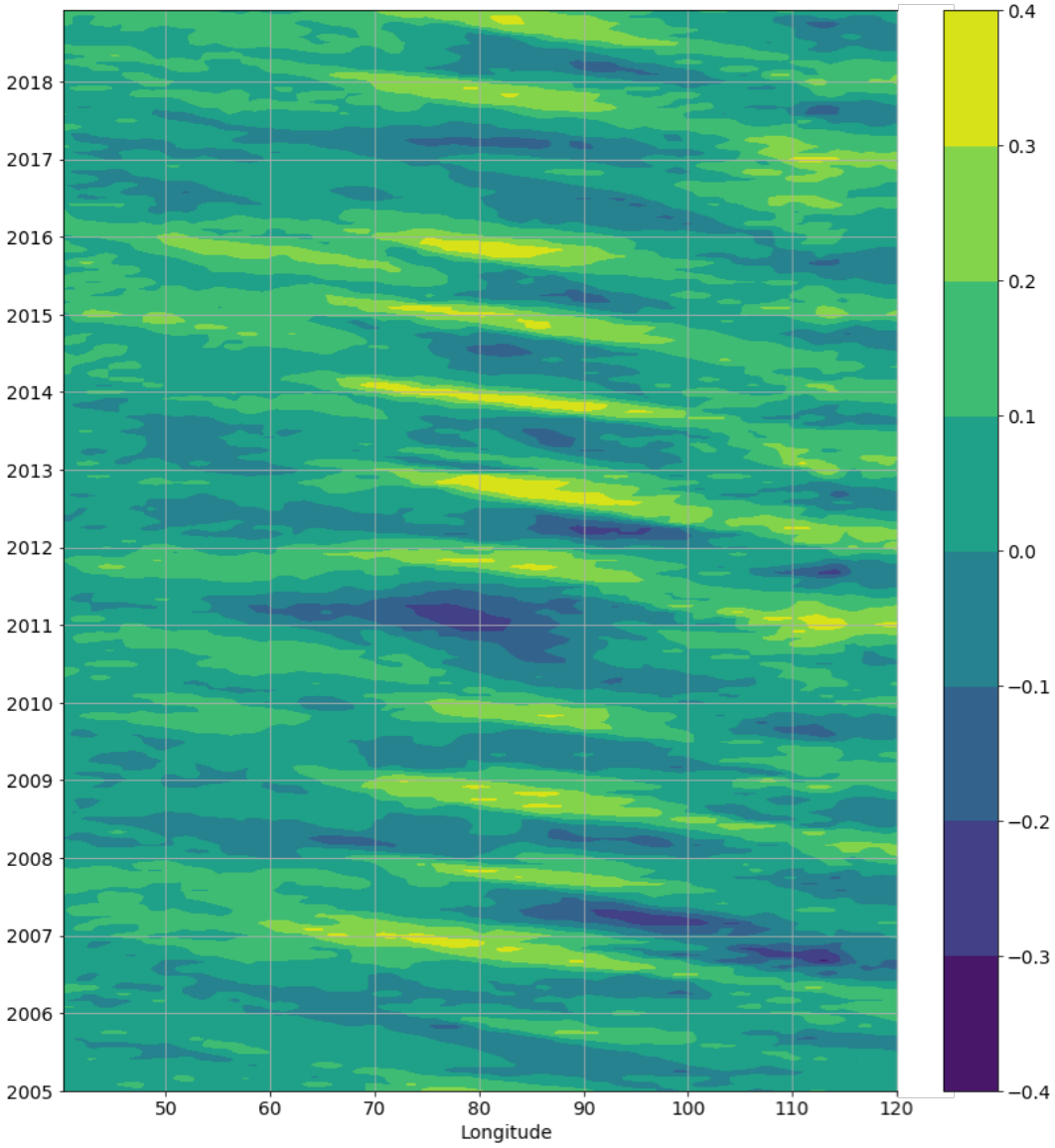


**Figure 4.15** Hovmöller diagram of sea level anomaly along 10.125°S. Sea level data is from the Global Ocean Multimission Altimeter dataset distributed by Copernicus. Yellow colors indicate higher sea level and blue colors lower sea level in units of meters. Westward propagating downwelling Rossby waves are seen annually in the second half of the year except during 2010 and 2016.

## 4.4 Discussion

Our results indicate that at both seasonal and interannual time scales the ITF propagation in the Indian Ocean basin is affected by the strength of the SCTR. In Figure 4.3 the latitude of minimum salinity, indicative of the ITF plume, is further to the south in the western part of the basin. This southward shift is present as from 50°E to 90°E during austral winter, following the development of the SCTR in April-July. As the SCTR strengthens, the meridional density gradients increase, and a cyclonic circulation develops around this upwelling center with increased geostrophic transport westward along its southern flank. The SEC, carrying ITF water, follows along the lower branch of this circulation, shifting slightly to the south from its initial trajectory in the eastern part of the basin.

The upwelling in the central Indian basin during 2010/11 and 2016/17 was unusual in that it was strong and eastward during the season when it is usually weak and contained to the western part of the basin. This region of shoaled thermocline was surrounded in both years by a cyclonic circulation (Figure 4.13) from SON through to JJA of the following year, whereas the climatological mean only shows this cyclonic circulation during MAM into JJA when the SCTR is seasonally strongest. This out of season cyclonic circulation disrupted the relatively zonal pathway of the SEC during SON and DJF, forcing the low salinity signal further to the south (Figure 4.5), and preventing low salinity waters from propagating westward in the first half of 2011 and 2017. In Figure 4.12 it is clear that these two years were characterized by a restriction in ITF propagation amounting to 20 degrees of longitude when compared with climatology. Although both 2010/11 and 2016/17 show anomalous upwelling in the central part of the basin between 70°E and 90°E, the location of the shallowest d20 is different for both years. During 2010/11 the shallowest d20 is located in the Chagos Dome region, while during 2016/17 it is

further westward in the Seychelles Dome region. In this study we focus on the unusual out of season upwelling in the central part of the basin generally, but future work should further address the relationship between the two domes and the westward ITF propagation more explicitly.

The cause of these unseasonably strong upwelling centers is likely due to the presence of favorable wind conditions for Ekman upwelling as well as an absence of westward propagating downwelling Rossby waves during the later halves of 2010 and 2016. During late 2010 to early 2011 and late 2016 to early 2017 the anomalous upwelling regions showed Ekman vertical velocities of $0.6 \times 10^{-5}$ $ms^{-1}$ (Figure 4.14). In both years the curl term contributed about $0.4 \times 10^{-5}$ $ms^{-1}$ of this velocity and the β-term about $0.2 \times 10^{-5}$ $ms^{-1}$. This magnitude of vertical velocity is not restricted to 2010/11 and 2016/17 but also occurs in 2012, 2013, and 2018, but these years do not have the same d20 and salinity anomalies. This indicates that remote forcing must also play a role during 2010/11 and 2016/17.

Annual westward propagating downwelling Rossby waves in the later half of the year are a prominent feature of the southern tropical Indian Ocean (Matsumoto and Meyers, 1998) and can be clearly seen in the SSH along 10°S in Figure 4.15. During late 2010 and 2016 the SSH remained low and this wave was not present. Downwelling Rossby waves act to deepen the thermocline in the Indian Ocean and therefore can affect the SCTR. During late 2006 into 2007 persistent easterly wind anomalies in the eastern Indian Ocean forced a westward propagating downwelling Rossby wave which deepened the thermocline in the SCTR (Hermes and Reason, 2009). Hermes and Reason (2009) describe how this wave increased SST and ocean heat content, contributing to an increase in tropical cyclone activity. We propose that, as the presence of these Rossby waves would deepen the thermocline, it follows that the absence of them, or the presence of upwelling waves, would allow the thermocline to remain shallow as we see in

2010/11 and 2016/17. This is supported by the modeling work of Tozuka et al. (2010) which showed that a strong Seychelles Dome was the result of both local Ekman upwelling and arriving upwelling Rossby waves. The 2006/7 event happened during the simultaneous occurrence of an El Niño and a positive IOD event causing easterly zonal wind anomalies over the tropical Indian, which are conducive to downwelling Rossby wave formation (Jury and Huang, 2004; Hermes and Reason, 2009). The 2010/11 and 2016/17 were times of coincident La Niña and negative IOD events (although the 2016/17 La Niña was weaker than that of 2010/11). Figure 4.16 shows the resulting positive zonal wind anomalies which are not conducive to downwelling Rossby wave formation. A schematic is presented in Figure 4.17. Figure 4.17a shows the climatological case where easterly winds are present and a westward propagating downwelling Rossby wave forms, which deepens the thermocline in the central portion of the basin and allows for the ITF to travel westward within the thermocline. Figure 4.17b shows the 2010/2011 and 2016/17 case where westerly wind anomalies are present and the annual downwelling Rossby wave does not form. Local winds force Ekman upwelling which creates an anomalous cyclonic circulation which lessens westward ITF propagation within the SEC.

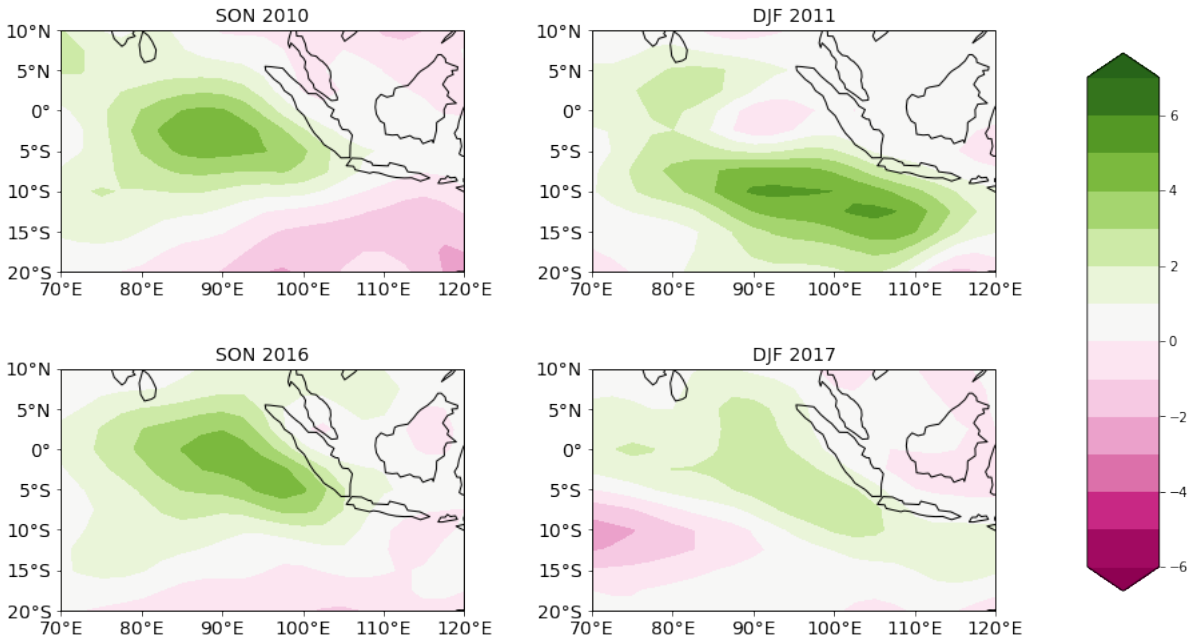


**Figure 4.16** Zonal wind anomalies during ***top*** September/October/November (SON) and December/January/February (DJF) of 2010/11, and ***bottom*** SON and DJF of 2016/17. Positive (westerly) zonal wind anomalies are present in the eastern tropical Indian Ocean for both years.

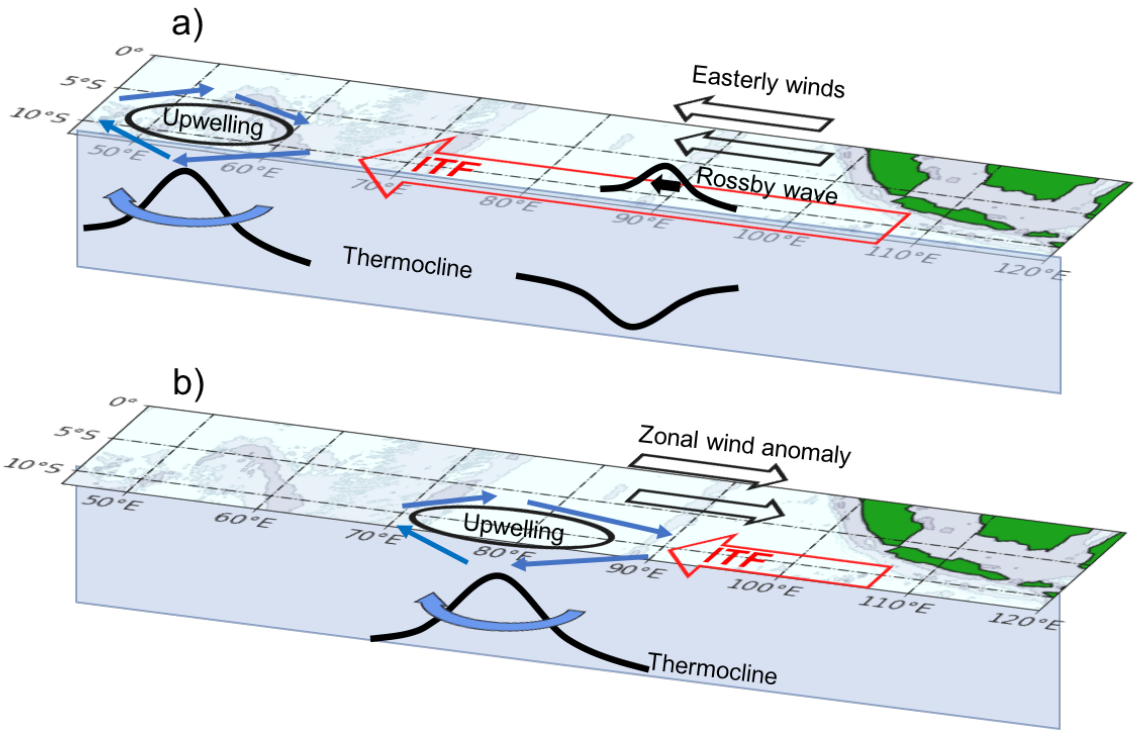


**Figure 4.17** Schematic showing climatological case in a) and 2010/11, 2016/17 case in b). In a) westward propagating downwelling Rossby waves traveling along 10°S which act to deepen the thermocline in the central Indian Ocean. The Seychelles Dome upwelling center is present at the western edge of the basin. The ITF travels far westward within the SEC. In b) westerly zonal wind anomalies are present and the annual downwelling Rossby wave does not form. Favorable local winds force Ekman upwelling in the central Indian Ocean and a cyclonic circulation develops disrupting the westward ITF transport within the SEC.

## 4.5 Summary

In this study we have used a combination of observations and reanalysis products to examine the variability of the ITF plume within the thermocline of the Indian Ocean South Equatorial Current on seasonal and interannual timescales. On seasonal time scales the low salinity plume reaches maximum westward propagation at different times of the year in the

eastern and western parts of the basin. Additionally, some years show further westward ITF propagation, whereas others, such as 2010/11 and 2016/17 show attenuated flow, with the plume remaining 20 degrees of longitude further east than climatology as seen in the 34.8 salinity contour. Thermocline characteristics, most importantly the strength, location, and timing of the SCTR, play an important role in ITF plume propagation. An anomalous strong and eastward SCTR out of season during 2010/11 and 2016/17 was driven by regional winds creating conditions favorable to both Ekman upwelling and the absence of the annual downwelling Rossby wave. The subsurface cyclonic circulation created by these upwelling centers disrupted the zonal flow within the SEC leading to reduced propagation of the ITF into the central Indian Ocean.

These results present a new addition to our understanding of Pacific/Indian inter-basin exchange. The ITF itself is affected by ENSO with increasing transport during La Niña and decreasing transport during El Niño (e.g. Meyers, 1996; England and Huang, 2005; Gordon et al., 2019). Once those waters reach the Indian and begin to travel westward, they are also affected by ENSO events, which, when in phase with the IOD, affects Rossby wave creation and the formation of the SCTR. This is especially important as we consider how future climate change may affect ENSO. Although it is still unclear, some studies such as Collins et al. (2005) suggest a slight probability of an increase in El Niño events in the coming decades.

This study only examined the ITF plume propagation and relationship to Indian Ocean thermocline variability during the Argo observational time period of 2005-2018. Longer time series such as reanalysis and model output could help to better define this relationship. As the ITF is an important source for the Agulhas Leakage, and interbasin exchange (le Bars et al.,

2013; Durgadoo et al., 2017) a better understanding of the conditions that control the ability of these waters to reach the western Indian is essential.

# Chapter 5: Conclusions and Future Work

This dissertation examines the Indonesian Throughflow on the western side of the Maritime Continent. Using observational and reanalysis data we draw connections between the small straits and the wider Indian Ocean and relate changes in the ITF pathways, out of the Indo-Australian basin and within the South Equatorial Current, to regional forcing.

In Chapter 2 Makassar Strait heat flux anomaly was calculated using a moored velocity profile and an ENSO varying temperature profile created by compiling in situ observations from CTDs, MBTs, XBTs, profiling floats and a moored temperature time series 2004-2006, within the Strait. These temperature observations confirmed that the thermocline tends to shoal (deepen) during El Niño (La Niña). The Makassar southward heat flux is strongly seasonal with an average difference between boreal winter (seasonal minimum) and summer (seasonal maximum) of 0.65PW. Makassar heat flux is closely related to total volume transport with the volume transport explaining 57% of the variance in heat flux. Changes in the velocity profile are more important than changes in the temperature profile to heat flux, with the velocity profile variability explaining 72% of the total variance in heat flux and the temperature profile 28%. Additionally, the upper layer (0-300 m) of volume transport, where the transport is greatest and also most variable, is more important to heat flux than the lower layer (320-740 m). Upper layer volume transport is very well correlated with heat flux anomaly with $r = 0.94$. Changes in Makassar heat flux are important for upper ocean heat content within the eastern tropical Indian Ocean. Gridded Argo data was used to determine heat content in the 0-300 m layer within the ITF outflow area. This heat content anomaly during the Argo era, when lagged 30 months, is well correlated ($r=0.83$) with Makassar heat flux anomaly. This is 2.5 year lag is indicative of an advective signal between the Makassar Strait and the southeast tropical Indian Ocean, and

indicates the importance of the Makassar Strait in determining upper ocean characteristics in the ITF outflow region.

One remaining challenge brought up by this chapter is the difficulty posed by a lack of continuous temperature measurements within the Indonesian Seas. Although the relationship between ENSO and the thermocline depth is well established and informed our methods, recent studies have shown that the effect on Makassar heat flux may be seasonally dependent with ENSO influence seen predominantly during July/August/September when southward flow is greatest (Gordon et al., 2019). Without continuous temperature measurements it is difficult to tease out these effects.

Chapter 3 examined the split between the South Equatorial Current and Leeuwin Current pathways for the ITF leaving the Indo-Australian basin. ITF waters enter both the SEC and LC but the ratio between these two pathways is not constant and is affected by regional atmospheric circulation. Gridded Argo data is used to calculate upper ocean heat content anomaly per $m^2$ in the immediate ITF outflow area, the northern Leeuwin Current and the eastern South Equatorial Current. We show that HCa in the upper ocean in the ITF outflow area is well correlated with HCa in the SEC source region ($r=0.8$, with 5 month lag), confirming that the SEC is the major pathways for ITF flow out of the Indo-Australian basin. During 2011, an anomalous increase in HCa leaving the Indonesian Seas does not propagate to the eastern SEC and is instead found within the LC. This southward shift of heat during 2011 was not simply due to the presence of a La Nina. It is noted that the La Nina of 2008/9 is associated with a westward propagation of positive heat content anomalies whereas the La Nina of 2011, a Ningaloo Niño year, saw a southward shift of these anomalies. NCEP/NCAR reanalysis wind data show that during Ningaloo Niño years of 2000 and 2011 a low pressure system developed off the northwest coast

of Australia, inducing anomalous cyclonic circulation. This reduced southerly winds off the west Australian coast allowing for an increase in LC transport, and induced northwesterly wind anomalies in the eastern tropical Indian Ocean decreasing the SEC. Over the Argo observational period (2005-2018) the SEC and LC vary in opposition to each other at interannual time scales, although this relationship can sometimes be obscured by longer term trends in SEC transport.

Although the LC is an important pathway for the ITF, Chapter 3 confirmed that the SEC remains the primary route into the Indian Ocean. In Chapter 4 this pathway was examined by using gridded Argo data to track the low salinity ITF signal within the South Equatorial Current thermocline, and identify thermocline variability that could affect this westward propagation. The ITF plume within the thermocline of the SEC varies at seasonal and interannual time scales, with the seasonal timing of the maximum of westward propagation varying with longitude across the basin. The maximum westward spreading in the western half of the basin during austral winter implicates the Seychelles Chagos Thermocline Ridge. The SCTR is well developed during this season and induces a westward geostrophic current on its southern flank that draws the ITF across the Indian basin. The SEC thermocline during late 2010 into 2011 and late 2016 into 2017 was marked by anomalously salty waters, indicating a reduction of westward ITF transport. Anomalous upwelling regions appeared centered at around 80°E and 10°S during September October November of 2010 (about 50 m shallower than climatology) and 2016 (about 30 m shallower than climatology) and continued into the following year. Although upwelling in this region associated with the SCTR is normal, such a strong upwelling in the central Indian basin during SON/DJF is unusual for that season. GODAS velocity at 105 m revealed a cyclonic circulation that developed around these upwelling regions, which disrupted the normal zonal flow of the SEC. This caused the westward ITF propagation to be constrained to an area about

20 degrees of longitude further to the east during both 2011 and 2017 when compared with climatology as seen in the 34.8 salinity contour. The unusual upwelling was caused by wind stress favorable to local Ekman upwelling as well as positive zonal wind anomalies in the south east tropical Indian Ocean which did not force the annual westward propagating downwelling Rossby wave during late 2010 and 2016.

This research has left us with many more questions for the future including: What happens within the SEC in the western part of the basin, especially regarding the split between the East African Coastal Current and the Mozambique Current? Does the ITF affect upper ocean heat content and SST in the center of the SCTR upwelling region, or is it primarily deflected to the south? Are ITF waters in the Leeuwin current primarily mixed into the south Indian Ocean or do they return to the Pacific? How do eddies shed off the Leeuwin Current play a role compared with the South Australian Current? Additionally, the research presented here is limited by the short time period of observational data. Continued analysis over many more ENSO, IOD, and Ningaloo Niño events is necessary to provide more confidence in, and context about, the results presented here.

In order to answer these questions, it is essential that observations are continued and expanded. In addition to our use of Argo data, we also relied on GODAS reanalysis, which assimilates observational data. Argo data was key to the work presented here, and is especially important in the historically undersampled Indian Ocean. Future work concerning the propagation of any ITF signal from the Leeuwin into the southern Indian Ocean as well as the ITF in the western portion of the SEC will certainly take advantage of these profiling floats as well as other observations such as the tropical RAMA moorings.

As mentioned above, longer time series of data would be useful to better understand interannual variability and decadal trends. As the only way to achieve longer time series is to continue observational campaigns and wait, an analysis of contemporary observations combined with regional models may be the best approach as the infrastructure for future observations is developed and maintained. My own ongoing work involves a project combining the Makassar observations presented here with coral $\delta^{18}O$ records from Murty et al. (2017), a proxy for sea surface salinity, within the Indonesian Seas and regional high resolution ocean models. The goal of this work is to draw connections between the overlapping time series of coral and Makassar data and use this to extend the Makassar time series 150 years into the past. Results so far are promising, with Makassar transport covarying nicely with coral $\delta^{18}O$ in the southern Lombok Strait. Next steps include using 1/20° ocean model hindcasts to provide some regional context for these changes and help identify the drivers of past ITF variability.

# References


Aagaard, K., and E.C. Carmack. 1989. The role of sea ice and other fresh water in the Arctic circulation. *Journal of Geophysical Research: Oceans* 94:14485-14498. https://doi-org.ezproxy.cul.columbia.edu/10.1029/JC094iC10p14485.

Asia Pacific Data Research Center. 2017. http://apdrc.soest.hawaii.edu/projects/argo/.

Andersson, H.C., and A. Stigebrandt. 2005. Regulation of the Indonesian throughflow by baroclinic draining of the North Australian Basin. *Deep-Sea Research Part I* 52:2214-2233. https://doi.org/10.1016/j.dsr.2005.06.014.

Banzon, V., T. M. Smith, T.M. Chin, C. Liu, and W. Hankins. 2016. A long-term record of blended satellite and in situ sea-surface temperature for climate monitoring, modeling and environmental studies. *Earth System Science Data* 8:165–176. doi:10.5194/essd-8-165-2016.

Behringer, D.W., and Y. Xue. 2004. Evaluation of the global ocean data assimilation system at NCEP: The Pacific Ocean. Eighth Symposium on Integrated Observing and Assimilation Systems for Atmosphere, Oceans, and Land Surface, AMS 84th Annual Meeting, Washington State Convention and Trade Center, Seattle, Washington, 11-15.

Benthuysen, J., M. Feng, L. Zhong. 2014. Spatial patterns of warming off Western Australia during the 2011 Ningaloo Niño: Quantifying impacts of remote and local forcing. *Continental Shelf Research* 91:232-246. https://doi.org/10.1016/j.csr.2014.09.014.

Boyer, T.P., J. I. Antonov, O. K. Baranova, C. Coleman, H. E. Garcia, A. Grodsky, D. R. Johnson, R. A. Locarnini, A. V. Mishonov, T.D. O'Brien, C.R. Paver, J.R. Reagan, D. Seidov, I. V. Smolyar, and M. M. Zweng. 2013. World Ocean Database 2013, NOAA Atlas NESDIS 72, S. Levitus, Ed., A. Mishonov, Technical Ed.; Silver Spring, MD, 209, http://doi.org/10.7289/V5NZ85MT.

Collins, M. 2005. El Niño- or La Niña-like climate change? *Climate Dynamics* 24:89-104.

DeVries, T. 2014. The oceanic anthropogenic $CO_2$ sink: Storage, air-sea fluxes, and transports over the industrial era. *Global Biogeochemical Cycles* 28:631-647. https://doi-org.ezproxy.cul.columbia.edu/10.1002/2013GB004739.

de Ruijter, W.P.M., A. Biastoch, S.S. Drijfhout, J.R.E. Lutjeharms, R.P. Matano, R. Pichevin, P.J. van Leeuwen, and W. Weijer. 1999. Indian-Atlantic interocean exchange: dynamics, estimation and impact. *Journal of Geophysical Research: Oceans* 104:20885-20910. https://doi.org/10.1029/1998JC900099.

Durgadoo, J.V., S. Rühs, A. Biastoch, and C.W.B. Böning. 2017. Indian Ocean sources of Agulhas leakage. *Journal of Geophysical Research Oceans* 122:3481-3499. doi:10.1002/2016JC012676.

England, M., and F. Huang. 2005. On the interannual variability of the Indonesian Throughflow and its linkage with ENSO. *Journal of Climate* 18:1435-1444. https://doi-org.ezproxy.cul.columbia.edu/10.1175/JCLI3322.1.

England, M. H., S. McGregor, P. Spence, G. A. Meehl, A. Timmermann, W. Cai, A. Sen Gupta, M. J. McPhaden, A. Purich, and A. Santoso. 2014. Recent intensification of wind-driven circulation in the Pacific and the ongoing warming hiatus. *Nature Climate Change* 4:222–227. doi:10.1038/NCLIMATE2106.

Fang, G., Y. Wang, Z. Wei, Y. Fang, F. Qiao, and X. Hu. 2009. Interocean circulation and heat and freshwater budgets of the South China Sea based on a numerical model. *Dynamics of Atmospheres and Oceans* 47:55-72.

Feng, M., G. Meyers, A. Pearce, S. Wijiffels. 2003. Annual and Interannual Variations of the Leeuwin Current at 32°S. *Journal of Geophysical Research Oceans* 108:C11. https://doi.org/10.1029/2002JC001763.

Feng, M., M.J. McPhaden, S. Xie, and J. Hafner. 2013. La Niña forces unprecedented Leeuwin Current warming in 2011. *Scientific Reports* 3.

Feng, M., J. Benthuysen, N. Zhang, and D. Slawinski. 2015. Freshening anomalies in the Indonesian throughflow and impacts on the Leeuwin Current during 2010-2011. *Geophysical Research Letters* 42:8555-8562.

Ffield A., and A.L. Gordon. 1992. Vertical Mixing in the Indonesian Thermocline. *Journal of Physical Oceanography* 22:184-195.

Ffield, A., K. Vranes, A.L. Gordon, R.D. Susanto, and S.L. Garzoli. 2000. Temperature Variability within the Makassar Strait. *Geophysical Research Letters* 27:237-240.

Ganachaud, A., and C. Wunsch. 2000. Improved Estimates of global ocean circulation, heat transport and mixing from hydrographic data. *Nature* 408(6811):453-457. doi:10.1038/35044048.

Ganachaud, A., and C. Wunsch. 2003. Large-Scale Ocean Heat and Freshwater Transports during the World Ocean Circulation Experiment. Journal of *Climate* 16:696–705. https://doi.org/10.1175/1520-0442(2003)016<0696:LSOHAF>2.0.CO;2.

Godfrey, J.S., and Ridgway K.R. 1985. The Large-Scale Environment of the Poleward Flowing Leeuwin Current, Western Australia: Longshore Steric Height Gradients, Wind Stresses and Geostrophic Flow. *Journal of Physical Oceanography* 15(5):481–495.

Godfrey, J. S. and T. J. Golding. 1981. The Sverdrup relation in the Indian Ocean, and the effect of Pacific–Indian Ocean Throughflow on the Indian Ocean circulation and on the East Australian Current. *Journal of Physical Oceanography* 11:771–779.

Gordon, A.L. 1985. Indian-Atlantic transfer of thermocline water at the Agulhas Retroflection. *Science* 227: 1030-1033.

Gordon, A.L. 1986. Inter-Ocean Exchange of Thermocline Water. *Journal of Geophysical Research* 91(C4): 5037-5046.

Gordon, A.L., R.F. Weiss, W.M. Smethie Jr., and M.J. Warner. 1992. Thermocline and intermediate water communication between the south Atlantic and Indian oceans. *Journal of Geophysical Research: Oceans* 97:7223-7240 https://doi.org/10.1029/92JC00485.

Gordon, A.L., S. Ma, D.B. Olson, P. Hacker, A. Ffield, L.D.Talley, D. Wilson, and M. Baringer. 1997. Advection and diffusion of Indonesian throughflow water within the Indian Ocean South Equatorial Current. *Geophysical Research Letters* 24:2573-2576.

Gordon, A.L., R.D. Susanto, and K. Vranes. 2003. Cool Indonesian throughflow as a consequence of restricted surface layer flow. *Nature* 425:824-828. https://doi-org.ezproxy.cul.columbia.edu/10.1038/nature02038.

Gordon, A.L., R.D. Susanto, A. Ffield, B.A. Huber, W. Pranowo, and S. Wirasantosa. 2008. Makassar Strait throughflow, 2004 to 2006. *Geophysical Research Letters* 35: L24605.

Gordon, A.L., J. Sprintall, H.M. Van Aken, D. Susanto, S. Wijffels, R. Molcard, A. Ffield, W. Pranowo, and A. Wirasantosa. 2010. The Indonesian throughflow during 2004-2006 as observed by the INSTANT program. *Dynamics of Atmospheres and Oceans* 50:115-128.

Gordon, A.L, B.A. Huber, J. Metzger, R.D. Susanto, H.E. Hulbert and T.R. Adi. 2012. South China Sea throughflow impact on the Indonesian throughflow. *Geophysical Research Letters* 39:LI 1602.

Gordon, A. L., P. Flament, C. Villanoy, and L. Centurioni. 2014. The nascent Kuroshio of Lamon Bay. *Journal of Geophysical Research Oceans* 119. doi:10.1002/ 2014JC009882.

Gordon, A.L., A. Napitu, B.A. Huber, L.K. Gruenburg, K. Pujiana, T. Agustiadi, A. Kuswardani, N. Mbay, and A. Setiawan. 2019. Makassar Strait Throughflow Seasonal and Interannual Variability: An Overview. *Journal of Geophysical Research Oceans* 124. https://doi.org/10.1029/2018JC014502.

Gruenburg, L.K., and A.L. Gordon. 2018. Variability in Makassar Strait heat flux and its effect on the eastern tropical Indian Ocean. *Oceanography* 31:2, 80-87.

He, Z., M. Feng, D. Wang, and D. Slawinski. 2015. Contribution of the Karimata Strait transport to the Indonesian throughflow as seen from a data assimilation model. *Continental Shelf Research* 92:16-22. https://doi.org/10.1016/j.csr.2014.10.007.

Hermes, J.C., and C.J.C. Reason. 2008. Annual cycle of the south Indian Ocean (Seychelles-Chagos) thermocline ridge in a regional model. *Journal of Geophysical research: Oceans* 113. https://doi.org/10.1029/2007JC004363.

Hermes, J.C., and C.J.C. Reason. 2009. The sensitivity of the Seychelles-Chagos thermocline ridge to large-scale wind anomalies. *Journal of Marine Science* 66:1455-1466.

Hirst, A., and J.S. Godfrey. 1993. The Role of Indonesian Throughflow in a Global Ocean GCM. *Journal of Physical Oceanography* 23:1057-1086.

Hu, S., and J. Sprintall. 2016. Interannual variability of the Indonesian Throughflow: The salinity effect. *Journal of Geophysical Research Oceans* 121:2596–2615, doi: 10.1002/2015JC011495.

Hu, S., and J. Sprintall. 2017. Observed strengthening of interbasin exchange via the Indonesian seas due to rainfall intensification. *Geophysical Research Letters* 44:1448-1456, doi: 10.1002/2016GL072494.

Ilahude, A.G., and A.L. Gordon. 1996. Thermocline stratification within the Indonesian Seas. *Journal of Geophysical Research* 101:12401-12409.vd.

Jury, M.R., and B. Huang. 2004. The Rossby wave as a key mechanism of Indian Ocean climate variability. *Deep-Sea Research Part I* 51:2123-2136.

Kalnay et al. 1996. The NCEP/NCAR 40-year reanalysis project. *Bulletin of the American Meteorological Society* 77: 437-470.

Kataoka, T., T. Tozuka, S. Behera, and T. Yamagata. 2014. On the Ningaloo Niño/Niña. *Climate Dynamics*, 43:1463–1482.

Kataoka, T., S. Masson, T. Izumo, T. Tozuka, and T. Yamagata. 2018. Can Ninfaloo Niño/Niña develop without El Niño-Southern Oscillation? *Geophysical Research Letters* 45(14):7040-7048 https://doi.org/10.1029/2018GL078188.

Kosaka, Y., and S.P. Xie. 2013. Recent global-warming hiatus tied to equatorial Pacific surface cooling. *Nature* 501:403–407. doi:10.1038/nature12534.

Le Bars, D., H.A. Dijkstra, and W.P.M. De Ruijter. 2013. Impact of the Indonesian Throughflow on Agulhas Leakage. *Ocean Science* 9:773–785. doi:10.5194/os-9-773-2013.

Lee, T., I. Fukumori, D. Menemenlis, Z. Xing, and L-L. Fu. 2002. Effects of the Indonesian Throughflow on the Pacific and Indian Oceans. *Journal of Physical Oceanography* 32:1404-1429.

Lee, S., W. Park, M.O. Baringer, A.L. Gordon, B. Huber, and Y. Liu. 2015. Pacific origin of the abrupt increase in Indian Ocean heat content during the warming hiatus. *Nature*

*Geoscience* 8:445-449. doi:10.1038/ngeo2438.

Levitus, S., J.I. Antonov, T.P. Boyer, O.K. Baranova, H.E. Garcia, R.A. Locarnini, A.V. Mishonov, J.R. Reagan, D. Seidov, E.S. Yarosh, and M.M. Zweng. 2012. World ocean heat content and thermosteric sea level change (0–2000 m), 1955–2010. *Geophysical Research Letters* 39:L10603. doi:10.1029/2012GL05110.

Li, M., A.L. Gordon, J. Wei, L.K. Gruenburg, and G. Jiang. 2018. Multi-decadal timeseries of the Indonesian Throughflow. *Dynamics of Atmospheres and Oceans* 81:84-95. https://doi.org/10.1016/j.dynatmoce.2018.02.001.

Liu, Q., M. Feng, D. Wang, and S. Wijffels. 2015. Interannual Variability in the Indonesian Throughflow transport: a revisit based on 30 year expendable bathythermograph data. *Journal of Geophysical Research Oceans*. doi: 10.1002/2015JC011351.

Ma, J., M. Feng, J. Lan, and D. Hu. 2020. Projected future changes in the meridional heat transport and heat balance in the Indian Ocean. *Geophysical Research Letters* 47. https://doi.org/10.1029/2019GL086803.

Marshall, A.G., H.H. Hendon, M. Feng, and A. Schiller. Initiation and amplitude of the Ningaloo Niño. *Climate Dynamics* 45:2367-2385.

Martinson, D.G. 2018. *Quantitative Methods of Data Analysis for the physical sciences and engineering*. Cambridge University Press, Cambridge, 598 pp.

Matsumoto, Y., and G. Meyers. 1998. Forced Rossby waves in the southern Tropical Indian Ocean. *Journal of Geophysical Research* 103(C12):27,589-27,602.

Meyers, G. 1996. Variation of Indonesian throughflow and the El Niño-Southern Oscillation. *Journal of Geophysical Research: Oceans* 12255-12263. https://doi-org.ezproxy.cul.columbia.edu/10.1029/95JC03729

Murty, S.A., N.F. Goodkin, H. Halide, D. Natawidjaja, B. Suwargadi, I. Suprihasnto, D. Prayudi, A.D. Switzer, and A.L. Gordon. 2017. Climatic Influences on Southern Makassar Strait Salinity over the past century. *Geophysical Research Letters* 44:119967-11975. https://doi-org.ezproxy.cul.columbia.edu/10.1002/2017GL075504.

National Oceanic and Atmospheric Administration. 2017. http://www.cpc.ncep.noaa.gov/data/indices/ersst4.nino.mth.81-10.ascii.

Nieves, V., J.K. Willis, and W.C. Patzert. 2015. Recent hiatus caused by decadal shift in Indo-Pacific heating. *Science* 349:532-535. DOI: 10.1126/science.aaa4521.

Pujiana, K., M.J. McPhaden, A.L. Gordon, and A.M. Napitu. 2019. Unprecedented response of Indonesian Throughflow to anomalous Indo-Pacific climatic forcing in 20167. *Journal of*

*Geophysical Research: Oceans* 124:3737-3754. https://doi-org.ezproxy.cul.columbia.edu/10.1029/2018JC014574.

Qiu, B., and S. Chen. 2010. Interannual-to-Decadal Variability in the Bifurcation of the North Equatorial Current off the Philippines. *Journal of Physical Oceanography* 40: 2525-2538.

Schneider, N., and T.P. Barnett. 1997. Indonesian throughflow in a coupled general circulation model. *Journal of Geophysical Research Oceans* 102:12341-2358.

Schneider, N. 1998. The Indonesian Throughflow and the Global Climate System. *Journal of Climate* 11:676-689.

Schott, A. F., and J. McCreary, 2001: The monsoon circulation of the Indian Ocean. *Progress in Oceanography* 51:1–123.

Schott FA, Xie SP & McCreary Jr JP. (2009). Indian Ocean circulation and climate variability. *Rev Geophys* 47:RG1002. doi:10.1029/2007RG000245.

Sen Gupta, A., S. McGregory, E. van Sebille, A. Ganachaud, J.N. Brown, and A. Santoso. 2016. Future changes to the Indonesian throughflow and Pacific circulation: the differing role of wind and deep circulation changes. *Geophysical Research Letters* 43:1669–1678. doi:10.1002/ 2016GL067757.

Smith, R.L, A. Huyer, J.S. Godfrey & J. Church. 1991. The Leeuwin Current off Western Australia, 1986–1987. *Journal Physical Oceanography* 21:323–345.

Smith, W.H., and D.T. Sandwell. 1997. Global sea floor topography from satellite altimetry and ship depth soundings. *Science* 277:1956-1962.

Song, Q., and A.L. Gordon. 2004. Significance of the Vertical Profile of Indonesian Throughflow Transport on the Indian Ocean. *Geophysical Research Letters* 31:L16307 doi:10.1029/2004GL020360.

Song, Q., A.L. Gordon, and M. Visbeck. 2004. Spreading of the Indonesian Throughflow in the Indian Ocean. *Journal of Physical Oceanography* 34:772-792.

Stammer, D., C. Wunsch, R. Giering, C. Eckert, P. Heimbach, j. Marotzke, A. Adcroft, C.N. Hill, and J. Marshall. 2003. Volume, heat, and freshwater transports of the global ocean circulation 1993–2000, estimated from a general circulation model constrained by World Ocean Circulation Experiment (WOCE) data. *Journal of Geophysical Research* 108:C1 3007. doi:10.1029/2001JC001115.

Sprintall, J., S.E. Wijffels, R. Molcard, and I. Jaya. 2009. Direct Estimates of the Indonesian Throughflow entering the Indian Ocean: 2004-2006. *Journal of Geophysical Research Oceans* 114, doi: 10.1029/2008JC005257.

Sprintall, J., A.L. Gordon, A. Koch-Larrouy, T. Lee, J.T. Potemra, K. Pujiana, and S.J. Wijffels. 2014. The Indonesian seas and their role in the coupled ocean-climate system. *Nature Geoscience*. doi: 10.1038/NGEO2188.

Susanto, R.D., A. Ffield, A.L. Gordon, and T.A. Adi. 2012. Variability of the Indonesian throughflow within Makassar Strait 2004-2009. *Journal of Geophysical Research* 117:C09013.

Takaaki, Y., T. Tozuka, and T. Yamagata. 2008. Seasonal Variation of the Seychelles Dome. *Journal of Climate* 21:3740-3754. https://doi.org/10.1175/2008JCLI1957.1.

Talley, L., and J. Sprintall. 2005. Deep expression of the Indonesian Throughflow: Indonesian Intermediate Water in the South Equatorial Current. *Journal of Geophysical Research* 110:C1009. doi:10.1029/2004JC002826.

Talley, L.D., G.L. Pickard, W.J. Emery, and J.H. Swift. 2011. Descriptive physical oceanography an introduction (6th Edition). *Elsevier* Figure 14.11(b).

Thompson, R.O.R.Y. 1984. Observations of the Leeuwin Current off Western Australia. *Journal of Physical Oceanography*. doi: https://doi-org.ezproxy.cul.columbia.edu/10.1175/15200485(1984)014<0623:OOTLCO>2.0.CO;2.

Tozuka, T., T. Yokoi, and T. Yamagata. 2010. A modeling study of interannual variations of the Seychelles Dome. *Journal of Geophysical Research Oceans* 115. https://doi.org/10.1029/2009JC005547.

Tozuka, T., T. Kataoka, and T. Yamagata. 2014. Locally and remotely forced atmospheric anomalies of Ningaloo Niño/Niña. *Climate Dynamics* 43:2197-2205.

van Aken, H.M., I.S. Brodjonegoro, and I. Jaya. 2009. The deep-water motion through the Lifamatola Passage and its contribution to the Indonesian throughflow. *Deep Sea Research Part I* 56:1203-1216. https://doi.org/10.1016/j.dsr.2009.02.001.

van Sebille, E., J. Sprintall, F.U. Schwarzkopf, A.S. Guota, A. Santoso, M.H. England, A. Biastoch, and C.W. Boning. 2014. Pacific-to-Indian Ocean Connectivity: Tasman leakage, Indonesian Throughflow, and the role of ENSO. *Journal of Geophysical Research Oceans* 119:1365-1382. doi:10.1002/2013JC009525.

Vidya, P. J., M. Ravichandran, M.P. Subeesh, S. Chatterjee, and N.M. 2020. Global warming hiatus contributed weakening of the Mascarene High in the Southern Indian Ocean. *Scientific Reports* 10:3255. https://doi.org/10.1038/s41598-020-59964-7.

von Känel L., T. L. Frölicher, and N. Gruber. 2017. Hiatus-like decades in the absence of equatorial Pacific cooling and accelerated global ocean heat uptake. *Geophysical Research Letters* 44. doi:10.1002/2017GL073578.

Vranes, K., A.L. Gordon, and A. Ffield. 2002. The heat transport of the Indonesian Throughflow and implications for the Indian Ocean heat budget. *Deep-Sea Research Part I* 49:1391-1410.

Wernberg, T., D.A. Smale, F. Tuya, M.S. Thomsen, T.J. Langlois, T. de Bettignies, S. Bennett, & C.S. Rousseaux. 2012. An extreme climatic event alters marine ecosystem structure in a global biodiversity hotspot. *Nature Climate Change* 3:28-82.

Woodbury, K.E., M.E. Luther, and J.J. O'Brien. 1989. The wind driven seasonal circulation in the southern tropical Indian Ocean. *Journal of Geophysical Research: Oceans* 94:17985-18002. https://doi.org/10.1029/JC094iC12p17985.

Wyrtki, K. 1961. Physical oceanography of Southeast Asian waters. NAGA Rep. 2, Scripps Institution of Oceanography, University of California, San Diego, 195 pp.

Wyrtki, K. 1987. Indonesian through flow and the associated pressure gradient. *Journal of Geophysical Research* 92:12941-12946.

Xie, S-P., H. Annamalai, F.A. Schott, and J.P. McCreary Jr. 2002. Structure and Mechanisms of South Indian Ocean Climate Variability. *Journal of Climate* 15:864–878. https://doi.org/10.1175/1520-0442(2002)015<0864:SAMOSI>2.0.CO;2.

Yuan, D., J. Wang, T. Xu, P. Xu, Z. Hui, X. Zhao, Y. Luan, W. Zheng, and Y. Yu. 2011. Forcing of the Indian Ocean dipole on the interannual variations of the tropical Pacific Ocean: roles of the Indonesian throughflow. *Journal of Climate* 24:3593-3608.

Zhang, Y., M. Feng, Y. Du, H.E. Phillips, N.L. Bindoff, M.J. McPhaden. 2018. Strengthened Indonesian Throughflow drives decadal warming in the Southern Indian Ocean. *Geophysical Research Letters* 45:6167-6175. https://doi.org/10.1029/2018GL078265.